Title
Self-Assembly of Semiconducting Polymers and Fullerenes for Photovoltaic Applications

Author
Huber, Rachel Colleen

Publication Date
2014

UNIVERSITY OF CALIFORNIA

Los Angeles

Self-Assembly of Semiconducting Polymers and Fullerenes for Photovoltaic Applications

A dissertation submitted in partial satisfaction of the requirements
for the degree Doctor of Philosophy in Chemistry

by

Rachel Colleen Huber

2014

ABSTRACT OF THE DISSERTATION

Self-Assembly of Semiconducting Polymers and Fullerenes For Photovoltaic Applications

by

Rachel Colleen Huber
Doctor of Philosophy in Chemistry
University of California, Los Angeles
Professor Sarah H. Tolbert, Chair

In this thesis we present methodologies for control and characterization of nanoscale film morphology and self-assembly in systems containing semiconducting polymers and fullerenes for use in photovoltaic devices. These materials are of interest to the photovoltaic community due to their facile processing and relative low cost. Organic photovoltaics consist of a photo-absorbing electron-donating polymer and an electron-accepting fullerene, upon exposure to light an electron-hole pair (excition) is formed. This exciton can travel 10-20 nm before if finds a polymer-fullerene interface or it will recombine. Due to this small exciton diffusion length, the study of the nanoscale morphology is pivotal in understanding and improving device properties.

Here we first explore how the crystallinity of different molecular components of a blended film affects device performance. Using grazing incidence wide-angle X-ray scattering

(GIWAXS), we find that different device fabrication techniques are optimized by polymers with different crystallinities. Additionally we studied all-polymer solar films through GIWAXS, which shows that these blends are approximately an addition of the two polymers; however, shifts of the polymer peaks elucidated how the polymers are mixing. To further these X-ray studies we used time-resolved microwave conductivity to study the local mobilities of fullerenes.

In the second half of this thesis, we examine a hydrogel network formed from a charged amphiphilic polymer, poly(fluorene-alt-thiophene) (PFT). This polymer self-assembles into rod-like structures in water and also shows improved conductivity in dried films due to its assembled structure. Here we use small angle X-ray scattering (SAXS) and TEM to confirm the nanoscale rod-like assembly, and employ rheology to study how the three dimensional network is held together. Finally, we examine photophysical changes upon the addition of a water-soluble fullerene, C_{60}-N,N-dimethylpyrrolidinium iodide, to PFT, as a step towards water-processable organic solar cells. Photoexcitation of aqueous assemblies of cationic polymers and fullerenes result in the formation of free charge carriers (polarons). These separated charge carriers are stable for days to weeks, which is unprecedented in polymer/fullerene assemblies. We have shown that through these fundamental studies of device architectures and intelligent molecular design, self-assembly has the power to provide a pathway towards improved photovoltaic device properties.

This dissertation of Rachel Colleen Huber is approved.

Pei Qibing

Yves Rubin

Sarah H. Tolbert, Committee Chair

University of California, Los Angeles

2014

To Those Who Always Believed in Me

TABLE OF CONTENTS

CHAPTER 3. Polymer/Polymer Blend Solar Cells Using Tetraazabenzodifluoranthene Diimide Conjugated Polymers as Electron Acceptors………………………………..37

LIST OF FIGURES

CHAPTER 2. Crystallinity Effects in Sequentially-processed and Blend-cast Bulk-heterojunction Polymer/Fullerene Photovoltaics

Chapter 3. Polymer/Polymer Blend Solar Cells Using Tetraazabenzodifluoranthene Diimide Conjugated Polymers as Electron Acceptors

Chapter 4. **Understanding Local and Macroscopic Electron Mobilities in the Fullerene Network of Conjugated Polymer-based Solar Cells: Time-Resolved Microwave Conductivity and Theory**

Chapter 5. **On the Structure and Conductivity of Semiconducting Polymer Hydrogels**

Chapter 6. Long-Lived Photoinduced Polaron Formation in Conjugated Polyelectrolyte/Fullerene Assemblies

LIST OF TABLES

CHAPTER 2. Crystallinity Effects in Sequentially-processed and Blend-cast Bulk-heterojunction Polymer/Fullerene Photovoltaics

Chapter 3. Polymer/Polymer Blend Solar Cells Using Tetraazabenzodifluoranthene Diimide Conjugated Polymers as Electron Acceptors

Chapter 4. Understanding Local and Macroscopic Electron Mobilities in the Fullerene Network of Conjugated Polymer-based Solar Cells: Time-Resolved Microwave Conductivity and Theory

LIST OF CHARTS

Chapter 3. **Polymer/Polymer Blend Solar Cells Using Tetraazabenzodifluoranthene Diimide Conjugated Polymers as Electron Acceptors**

ACKNOWLEDGEMENTS

I would like to thank my family and friends for sticking by me through this entire process. It was not often an easy path to follow but at the moments where I could not fathom continuing they were always there with a sympathetic ear and words of encouragement. I'd specifically like to thank my mom, Vicki Huber, because she is the only person I actually don't mind talking to on the phone and she put up with my science talk even though she often didn't know what I was talking about. Yet my mother and brother, Travis Huber, celebrated in my triumphs and commiserated in my failures. I now challenge my brother to get a PhD because at this point I am beating you, two masters does not equal a PhD. My father was there with the latest sports update when I would miss a particularly important football or baseball game. And although both my Grandfathers did not make it to see this day, I know they would be proud because they always believed in me. My Grandmother is still hoping that I make it back to Oregon but knows how much I love her. Last but not least I'd like to thank my dog Remy, who I adopted during my fourth year of graduate school and without his craziness I may not have stayed sane enough to finish this adventure.

I'd like to thank Professor Sarah Tolbert for putting up with me during graduate school. Without her I would not be the person I am today, she pushed me to become a scientist that I didn't even know I could be. She instilled in me that to be a good scientist you need to be able to share science with everyone, not just other scientists. This meant that I had to understand subjects deeply to be able to describe them to people with little to no scientific background. Sarah also taught me to approach scientific problems from different angles, to efficiently work towards a solution. I will carry the lessons that she taught me for the rest of my life and I thank her for that.

I'd like to thank the past and current members of the Tolbert group. Without the support of those who came before and those who will remain after I leave, graduate school would not be possible. And because I worked in the solar collaboration I would also like to thank the Schwartz, Rubin and Neuhauser groups for their scientific discussion, help and friendships.

I do, however, need to name names for a few people who were incredibly supportive. First I'd like to thank Christopher Tassone, who I shared a two-person office with for a couple of years during graduate school. He is now a beamline scientist at SSRL and even though he is exceptionally busy, he still manages to find time to talk whenever I need him. Next, I'd like to thank Laura Schelhas. Even though we never worked on the same projects, it was always beneficial to bounce ideas off each other. Let alone we also spent plenty of time walking around the geology building venting about one thing or another. Amy Ferreira was also part of that tradition, as she also worked on all of these science projects with me. Patrick Yee who was my undergraduate research assistant apparently liked me enough to stay on to become my replacement on the solar project. I hope that I've aptly prepared him for what he has gotten himself into.

I also need to thank my non-science friends because they were incredibly supportive both by asking about my projects but also allowing me to not talk about my projects. Benjamin Edwards has always been so proud of me and is an amazing Sunday morning brunch date. Crys Hernandez also always gave me a place to go when I just needed a change of scenery or a home-cooked dinner. Every time I made it back to Portland, April Fleming made me explain my projects to her, which was always good for determining if I really knew what I was talking about.

I would also like to thank Professor Johnny Pang for allowing me to TA for him whenever I was required to teach. He always made the process enjoyable along with entrusting me with the night classes. Also teaching for someone who cares so much about his students was truly inspiring.

In general I've been lucky to surround myself with good people who have made this process bearable and without their love and support I would not be a PhD graduate.

I wish to thank my committee memebers, Professor Yves Rubin and Professor Qibing Pei for their help and support in writing this thesis. Additionally, I'd like to thank Professor Xiangfeng Duan for serving on my oral committee. And finally I would like to thank Professor Benjamin Schwartz, Professor Yves Rubin, Dr. Nikos Kopidakis and Professor Johnny Pang for letters of recommendation.

Chapter 2 is a version of: Rachel C. Huber, Guangye Zhang, Amy S. Ferreira, Shane D. Boyd, Christine K. Luscombe, Sarah H. Tolbert, and Benjamin J. Schwartz, "Crystallinity Effect in Sequentially-Processed and Blend-Cast Bulk Heterojunction P3HT/PCBM Photovoltaics." *J. Phys. Chem. C,* 2014, 118 (32), 18424-18435. Guangye fabricated the devices and films. Amy and I measured the films at SSRL and performed analysis. Shane synthesized the polymer. Guangye wrote the initial manuscript; Amy and I helped edit the paper. Professor Luscombe, Professor Tolbert and Professor Schwartz helped edit the manuscript.

Chapter 3 is a version of Haiyan Li, Ye-Jin Hwang, Taeshik Earmme, Rachel C. Huber, Conor O'Brien, Sarah H. Tolbert and Samson A. Jenekhe, "Polymer/Polymer Blend Solar Cells Using Tetraazabenzodifluoranthene Diimide Conjugated Polymers as Electron Acceptors." Haiyan Li, Ye-Jin Hwang, and Taeshik Earmme synthesized, characterized and made devices of these polymers. I performed the grazing incidence wide-angle X-ray scattering and subsequent analysis. Haiyan Li wrote the paper and all collaborators helped to edit. Professor Tolbert and Professor Jenekhe helped edit the manuscript.

Chapter 4 is a version of Jordan C. Aguirre, Christopher Arntsen, Samuel Hernandez, Rachel Huber, Alexandre M. Nardes, Merissa Halim, Daniel Kilbride, Yves Rubin, Sarah H. Tolbert, Nikos Kopidakis, Benjamin J. Schwartz, and Daniel Neuhauser, "Understanding Local and Macroscopic Electron Mobilities in the Fullerene Network of Conjugated Polymer-based Solar Cells: Time-Resolved Microwave Conductivity and Theory" *Advanced Functional Materials*, 2013, 24, 784-792. Chris and Sam performed theory calculations, Jordan and Alexandre performed the TRMC, Daniel Kilbride and Merissa Halim synthesized the fullerenes and I fabricated SCLC devices. Jordan wrote the manuscript and all collaborators helps edit. Dr. Kopidakis, Professor Schwartz, Professor Rubin, Professor Tolbert, and Professor Neuhauser helped to edit the manuscript.

Chapter 5 is a version of: Rachel C. Huber, Amy S. Ferreira, Jordan C. Aguirre, Daniel Kilbride, Daniel Toso, Kenny Mayoral, Thomas G. Mason, Z. Hong Zhou, Nikos Kopidakis, Yves Rubin, Benjamin J. Schwartz and Sarah H. Tolbert, "Structure of Poly(fluorene-alt-thiophene) Hydrogel." Daniel Kilbride synthesized the polymer. I performed the rheology work, under the supervision of Kenny Mayoral. Amy and I collect small angle X-ray scattering data (SAXS), I analyzed this data by Primus and IRENA. Amy analyzed the SAXS data by Dammin Bead models. Jordan performed time-resolved microwave conductivity at NREL with Nikos Kopidakis. Daniel Toso performed CryoEM. I wrote the manuscript and all the graduate student collaborators helped with the edits. Professor Mason, Professor Zhou, Dr. Nikos Kopidakis, Professor Rubin, Professor Schwartz and Professor Tolbert helped edit the manuscript.

Chapter 6 is a version of: Rachel C. Huber, Amy S. Ferreira, Daniel Kilbride, Robert Thompson, Nicholas S. Knutson, Lekshmi Sudha Devi, Daniel B. Toso, Z. Hong Zhou, Yves Rubin, Benjamin J. Schwartz and Sarah H. Tolbert, "Long-Lived Photoinduced Polaron Formation in Conjugated Polyelectrolyte/Fullerene Assemblies." Daniel Kilbride synthesized the polyelectrolyte. Robert and Nicholas synthesized the water-soluble fullerene. Daniel Toso performed cryoEM. Amy and I collect SAXS data, I analyzed this data by Primus and IRENA. Amy and I collected photoluminescence data, UVvis and EPR data. Lekshmi performed pump-probe experiments. I wrote the manuscript and all the contributing graduate and post doctoral collaborators helped with the edits. Professor Zhou, Professor Rubin, Professor Schwartz and Professor Tolbert helped edit the manuscript.

Professor Sarah Tolbert directed the research present in this manuscript. Funding of this research was provided by the ONR, NSF and DOE EFRC MEEM. Portions of this research were performed at the Stanford Synchrotron Radiation Lightsource, a national user facility operated by Stanford University on behalf of the U.S. Department of Energy, Office of Basic Energy Sciences.

VITA

2008	B.S. in Advanced Chemistry, Oregon State University
2008-2014	Teaching Assistant, Department of Chemistry and Biochemistry, UCLA
2011	EQ-SANS Workshop, Oak Ridge National Laboratory, Oak Ridge, Tennessee
2012	Departmental Travel Grant for ACS Meeting, March 2012, Department of Chemistry and Biochemistry, UCLA
2012	American Chemical Society Travel Award, ACS Meeting March 2012
2013	Fifteenth Neutron and X-ray Scattering School, Argonne National Laboratory, Argonne, Illinois and Oak Ridge National Laboratory, Oak Ridge, Tennessee

PUBLICATIONS AND SELECTED PRESENTATIONS

Huber, R.C., Zhang, G., Ferreira, A., Boyd, S. D., Luscombe, C. K., Tolbert, S. H., and Schwartz, B. J. "Crystallinity Effect in Sequentially-Processed and Blend-Cast Bulk Heterojunction P3HT/PCBM Photovoltaics" *J. Phys. Chem. C,* 2014, 118 (32), 18424-18435.

Aguirre, J.C., Arntsen, C., Hernandez, S., **Huber, R.C.**, Nardes, A. M., Halim, M., Kilbride, D., Rubin, Y., Tolbert, S.H., Kopidakis, N., Schwartz, B.J. and Neuhauser, D.N. "Understanding Local and Macroscopic Electron Mobilities in the Fullerene Network of Conjugated Polymer-Based Solar Cells: Time-Resolved Microwave Conductivity and Theory". *Adv. Funct. Mater.* 2014, *24*, 784–792.

Hawks, S.A., Aguirre, J.C., Schelhas, L.T., Thompson, R., **Huber, R.C.**, Ferriera, A., Zhang, G., Street, R.A., Herzing, A.A., Tolbert, S.H. and Schwartz, B.J. "Comparing Matched Polymer:Fullerene Solar Cells Made by Solution-Sequential Processing and Traditional Blend Casting: Nanoscale Structure and Device Performance" *J. Phys. Chem. C,* 2014, 118 (31), 17413-17425.

Huber, R.C., Aguirre, J.C., Kopidakis, N., Schwartz, B.J. and Tolbert, S.H. EFRC PI Meeting, Washington D.C., July 2013. Poster Presentation: Self-Assembling Polymer/Fullerene Systems for Organic Photovoltaics.

Huber, R.C., Ferreira, A., Kilbride, D., Aguirre, J., Toso, D., Zhou, H., Rubin, Y., Kopidakis, N., Schwartz, B.J., and Tolbert, S. H. American Chemical Society National Meeting, San Diego, CA, March 2012. Oral Presentation: Optimizing Nanoscale Architecture in Semiconducting Polymers.

Huber, R.C., Ferreira, A., Kilbride, D., Thompson, R., Rubin, Y., Schwartz, B.J., and Tolbert, S. H. American Chemical Society National Meeting, Anaheim, CA, March 2011. Oral Presentation: Optimizing Nanoscale Architecture in Semiconducting Polymers.

Huber, R.C., Ferreira, A., Kilbride, D., Thompson, R., Rubin, Y., Schwartz, B.J., and Tolbert, S. H. Nanotechnology Student Summer School, The 6th NIMS/MANA (Japan), Nanoscience Centre, University of Cambridge (UK), UCLA/CNSI (USA), Los Angeles, CA July 37-31, 2009. Oral Presentation: Study of Amphiphilic Polymers for Solar Cell Applications.

CHAPTER 1

INTRODUCTION

Organic photovoltaics (OPVs) are of increased interested due to their ease of processing, ease of installation and low cost. Traditional solar devices are fabricated from mono- or polycrystalline silicon, which is costly to install but has the benefit of higher efficiencies than OPVs. An apt method of comparison between OPV and silicon (Si) devices is the energy payback time (EPBT), this is a calculation of how much time is required to gain back the energy that was used to fabricate these devices.[1] The EPBT time is comparable for Si and OPV device, where Si is 1.65-4.14 years and OPV is 0.2-4 years. It is worth mentioning that this is a comparison between efficiencies of 25% for Si devices and only 2% for OPVs. So even at this juncture with OPV efficiencies significantly lower then their competitor, OPVs are still a viable option. If the quoted efficiencies of 10% can be reached on large area roll-to-roll processing, then OPVs could become a main source of renewable energy.[2]

OPVs consist of a photo-absorbing electron-donating polymer and an electron-accepting fullerene. The workhorse polymer and fullerene in literature is poly(3-hexylthiophene-2,5-diyl) (P3HT) and [6,6]-phenyl-C_{61}-butyric acid methyl ester (PCBM); however, the higher efficiency OPVs employ redder absorbing donor-acceptor polymers.[3] Upon excitation of the polymer, an electron-hole pair (exciton) is formed. This exciton has a diffusion length of 10-20 nm, where it can either find a polymer:fullerene interface and undergo charge transfer or it recombines.[4] Recombination of the electron and hole means that the photons absorbed by the device are not contributing to the photocurrent; therefore, an OPV device requires an intermixed morphology to efficiently split the exciton into free carriers. Our aim is to use careful design of the nanoscale morphology through self-assembly of the active layer materials is a pathway towards increased efficiencies of polymer:fullerene devices.

My thesis is divided into five chapters: Polymer properties required for different methods of device fabrication (Chapter 2), structural characterization of all-polymer solar devices (Chapter 3), comparing local and macroscopic mobilities of fullerene derivatives (Chapter 4), structural characterization of an amphiphilic polymer (Chapter 5), and analysis of long-lived charge carriers produced by the assembly of an amphiphilic polymer and water-soluble fullerene (Chapter 6).

The second chapter is a study of controlling active layer morphology by varying polymer regioregularity (RR) and polydispersity index (PDI) between two different fabrication techniques, blend-casting (BC) and sequential processing (SqP). BC is the traditional technique employed for solar device fabrication, where the polymer and fullerene are dissolved and deposited out of the same solvent. The other technique, SqP, deposits the polymer layer first and then the fullerene is deposited on top of the polymer out of an orthogonal solvent. The use of the orthogonal solvent is to insure that the underlying polymer layer is not dissolved. Each of these fabrication techniques results in an intimately mixed system that is referred to as a bulk heterojunction (BHJ). The SqP device morphology relies on intercalation of the fullerene into the underlying polymer layer; whereas, BC relies on phase separation of the polymer and fullerene driven by thermal annealing. Because of this difference, SqP leads to more reproducible and scalable devices.

To further study these fabrication techniques we used two different polymers, one was the commercially available Rieke polymer that has low regioregularity (LR P3HT) and two high regioregularity P3HTs with molecular weights (MW) of 16 kDa and 37 kDa (16K HR P3HT and 37K HR P3HT, respectively) synthesized by Christine Luscombe's group from the University of Washington. It has been shown that as RR increases so does the crystallinity; therefore the 16K HR P3HT and 37K HR P3HT are more crystalline than the LR P3HT. When these polymers are integrated into a solar cell device we found that SqP performs better with the LR P3HT and BC performs better with HR P3HT. BC requires phase separation of the polymer and fullerene, which will be kinetically driven by a higher crystalline polymer. Whereas, SqP relies on intercalation of the PCBM into the P3HT layer, this process is facilitated by the presence of amorphous P3HT for the PCBM to intercalate into. This study showed that BC and SqP require different polymer characteristics to achieve the highest device efficiency.

In the third chapter of this thesis, we study the use of a n-type polymer as an electron acceptor as a replacement for the traditional fullerene derivative. Since fullerenes do not typically absorb visible light, the introduction of another polymer into an organic photovoltaic allows for more excitation events in the active layer of the film. Even with this extra advantage, the n-type polymer does not perform as well as devices fabricated with PCBM as the electron acceptor. Two similar n-type polymers (PBFI-T and PBFI-S) are synthesized with the main difference being the linking group in the co-polymer, either thiophene (T) or selenophene (S). A majority of the characterization techniques show similar physical properties; however, by grazing incidence wide-angle X-ray scattering (GIWAXS) we are able to observe more mixing of the PBFI-S with the p-type polymer (PSEHTT) then with the PBFI-T copolymer. This difference in miscibility of the polymers results in different device performance.

In the fourth chapter, we study the local and macroscopic mobilities of two fullerene derivatives. These fullerene derivatives are pentaaryl-substituted (shuttlecocks (SCs)), one with tert-butyl groups (4-tBu) and the other with methyl groups (4-Me). The assembly of these fullerenes affects the electron mobilities, which can be studied through time-resolved microwave conductivity (TRMC). TRMC is a unique tool that allows for measurement of local mobilities in solid-state films. In TRMC photoinduced carriers are created by an incident laser pulse on the sample. The carriers are then induced to move by the electric field from microwave radiation, and the change in microwave power is measured as these photoinduced carriers absorb microwaves. The change in microwave power after passing through the sample is proportional to the local nm-scale photoconductivity of the sample, which is the carrier yield times the sum of the mobilities of all carriers, which in our case is both electron and hole mobilities. We are able to compare these local mobilities to macroscopic mobilities by fabricating space-charge limited current (SCLC) devices. Through this study, we determined that the local mobilites of 4-tBu and 4-Me were similar to PCBM; however, the bulk mobilities of the SCs was significantly lower.

In the fifth chapter, we deduce the structure of poly(fluorene-alt-thiophene) (PFT) hydrogel. PFT is an amphiphilic polymer that forms rod-like micelles in water. At a 2% w/v of PFT it forms a gel and through various rheology experiments we were able to determine that the gel is held together by “sticky-ends”. These “sticky-ends” are created because not all of the polymer chains in the micelle align upon creation of the hydrogel. These misaligned ends, or “sticky-ends”, of the polymer chains can then bridge other polymer micelles thus forming an interconnected network. PFT is a semiconducting polymer with a conducting backbone that runs the length of the polymer micelle and such an interconnected network would be highly beneficial for moving charges through a solar cell device. Our group has previously shown that the self-assembled network mobility is four times higher than the uncharged version of the PFT polymer.[5] The use of PFT in a water-processable solar cell device would also be a pathway towards a "green" environmentally friendly method to fabricate OPVs.

The fourth chapter combines PFT with a water-soluble fullerene, C60-N,N-dimethylpyrolldinium iodide ($C_{60}(N^+)_n$), to create long-lived charge carriers in solution. These long-lived charge carriers are polarons, a stable radical ion with a resulting lattice distortion. The polaron formed on PFT is observable in the visible region at ~700 nm, which means we can track the polaron formation by UV-vis. However, $C_{60}(N^+)_n$ is composed of various isomers (n=2-5) and the polaron formation is only observed with the bis (n=2) fullerene adducts. The bis adducts are composed of six different isomers, and to further study the self-assembly of PFT and 'mixed-bis' adducts we were able to separate these isomers into two fractions that were composed of mostly *trans*-2 and *trans*-3 isomers. Overall, the bis adducts are not water-soluble so assembly with PFT is required to dissolve the fullerene. The charged side groups on the *trans*-3 isomer are on the same side of the fullerene ball, allowing *trans*-3 to assemble within the PFT micelle. The *trans*-2 adducts are arranged on opposite sides of the fullerene ball making *trans*-2 more isotropically charged then *trans*-3. Thus *trans*-3 assembles between the polymer chains in the PFT micelle and *trans*-2 assembles outside of the micelle near the charged side chains of PFT; allowing both fullerene bis adducts to be thermodynamically stable in their respective environments. The compilation of these results tells us that the long-lived polaron formation is facilitated by the fast charge transfer to the *trans*-3 isomer present in the polymer micelle, after this the electron is shuttled out to the *trans*-2 isomer where is it stabilized by the dielectric of the water. This process is reminiscent of photosynthesis, where the electrons created are shuttled out of the recombination range to be used in later processes. The polarons formed from the assembly of PFT and C_{60}-$(N^+)_2$ are stable for months without recombining, which is unprecedented in the literature.

Chapter 6 will summarize this work and suggest future directions to continue this research.

Overall the purpose of this work is to study the self-assembly and structure of semiconducting polymers and fullerenes, to determine how to improve the active layer morphology of an OPV. We analyzed the structure of polymer:fullerene and polymer:polymer films to determine how structure affects device performance. Along with studying the local and macroscopic mobilities of fullerene derivatives, we strive to determine what makes PCBM the best electron acceptor for organic solar devices. Next, we studied an amphiphilic polymer in hopes to use self-assembly of PFT to create more efficient pathways for the charges to be removed from a solar device. Lastly, in the process of creating a water-soluble solar cell we discovered long-lived charge carriers in a PFT:fullerene solution system that proves back-electron transfer is blocked, which could be beneficial for an all water-processable solar cell.

CHAPTER 2

Crystallinity Effects in Sequentially-processed and Blend-cast Bulk-heterojunction Polymer/Fullerene Photovoltaics

2.1. Introduction

In recent years, dramatic progress has been made in the field of organic photovoltaics (OPVs),[6,7] resulting in power conversion efficiencies (PCEs) of polymer/fullerene devices surpassing 10%.[8–11] This achievement is based mostly on traditional blend-cast (BC) bulk heterojunctions (BHJs),[12] in which an electron-donating polymer and electron-accepting fullerene are mixed together in a solution that is used to cast the active layer of the organic solar cell. The resulting film is then typically thermally or solvent annealed to promote phase separation of the polymer and fullerene, resulting in a conductive network for both electrons and holes as well as intermixed regions where a majority of charge separation occurs.[13–22] The morphology of BC BHJ films is dictated by multiple factors, including the donor/acceptor miscibility, the propensity of one or both materials to crystallize,[21,23–26] the relative solubilities of the two materials in the casting solution, the drying kinetics of the film, the presence of any solvent additives,[27–31] etc. Because the nm-scale morphology depends on so many of the details of how the film is cast, the device performance of BC BHJ solar cells is hypersensitive to the processing kinetics of the active layer.[12] Thus, for any new set of OPV materials, an Edisonian approach involving the fabrication of hundreds of BC devices is needed to find the processing conditions that lead to the optimal morphology and best device performance.

An alternative approach to preparing polymer/fullerene active layers for photovoltaic applications has been to sequentially process the polymer and fullerene components in separate steps by depositing the materials from orthogonal solvents.[32] This sequential processing (SqP) technique has been studied by several groups in both polymer-fullerene[33–41] and small molecule-fullerene systems.[42] It is well established that even though the fullerene is deposited on top of the polymer layer, the resultant film still has a significant amount of fullerene dispersed through the polymer layer,[43] particularly after thermal annealing.[44–46] Not only are the PCEs of devices fabricated via SqP comparable to or better than the more traditional BC devices,[41,42,47–53] but the SqP method also provides several distinct advantages that could make it the preferred route for large-scale fabrication of polymer-based photovoltaics. First, films produced via SqP have a more reproducible morphology because SqP does not rely on kinetic control of the nm-scale structure, resulting in devices that behave more consistently (*cf.* Figure 2.1, below).[32,54] Second, since the two materials are deposited separately, one can optimize or otherwise deliberately alter the donor material (e.g., by chemical doping) either before[55–57] or after[58] it has been processed, without unwanted chemistry occurring with the electron-accepting material. Third, sequentially-processed films are guaranteed to have a fullerene network that is connected to the top of the film, avoiding issues with undesirable vertical phase separation that necessitate the use of an inverted device geometry. Finally, many solubility issues can be bypassed since one can separately choose optimal solvents for the donor and acceptor materials.[42,59] Thus, the SqP technique potentially opens the photovoltaic field to a variety of donor and acceptor materials that once were not usable due to compatibility issues between solvents and materials.

Although it is clear that the BHJ morphology of films produced via SqP is generally similar to that of BC films in that the fullerene is dispersed throughout the polymer, a variety of experiments have suggested that the details of the nm-scale distribution of the polymer and fullerene differ between the two processing techniques. For example, ultrafast spectroscopic studies have shown that the dynamics of exciton quenching and polaron production are different in optically-matched sequentially-processed and BC films made from the workhorse materials poly(3-hexylthiophene) (P3HT) and [6,6]-phenyl-C_{61}-butyric-acid-methyl-ester (PCBM).[60] Moreover, nominally matched sequentially-procssed and BC photovoltaic devices show different behaviors upon thermal annealing.[42,53,54,61] Thus, one of the most important issues concerning solar cells fabricated via SqP is precisely how the nm-scale morphology is different from that in BC films, and what factors control the extent and distribution of fullerene interpenetration into the polymer underlayer.

In this paper, we work to build an understanding of the fullerene distribution in P3HT/PCBM BHJ solar cells produced via both SqP and blend-casting. Our approach is to take advantage of a series of P3HTs with a narrow molecular weight distribution and precisely controlled regioregularity that allow us to explore how changing specific attributes of the polymer leads to differences in both the BHJ architecture and in the PV performance of sequentially-procssed and BC devices. It is well known that polymer regioregularity and polydispersity index (PDI) can have dramatic effects on the photovoltaic performance of BC BHJs,[62–68] and here we extend these studies to sequentially-processed devices, focusing in particular on how regioregularity affects the morphology and device performance of thermally annealed P3HT/PCBM active layers. In agreement with previous suggestions, we first find that PCBM deposited by sequential processing preferentially penetrates into the amorphous regions of the P3HT underlayer, leaving the crystalline regions of the polymer essentially intact.[45,61] We then show that too much polymer crystallinity is actually unfavorable for SqP photovoltaic devices because too little fullerene can penetrate around the crystallites, leading to over-phase separation of the polymer and fullerene. In contrast, BC devices show the opposite behavior: highly regioregular (and thus more crystalline) P3HT provides better efficiencies than BC devices made from lower regioregularity P3HTs. We thus conclude that sequentially-processed and BC BHJ devices require different materials properties to achieve formation of their ideal active layer morphologies.

2.2. Experimental

The key feature underpinning this work is the successful synthesis of P3HT with well-defined regioregularity and extremely narrow PDI.[69] In what is described below, we compare the behavior of three different batches of P3HT: commercial P3HT purchased from Rieke Metal Inc. (BASF Sepiolid^{TM} P100), which we denote as LR P3HT, and two in-house batches synthesized with 98% regioregularity and average molecular weights of about 16 kDa (PDI = 1.18) and 37 kDa (PDI = 1.19), denoted as HR P3HTs, where LR and HR stand for low regioregularity and high regioregularity, respectively. The full characteristics of the three batches we focus on here are summarized in Table 2.1.

For measurements of the optical properties and for structural characterization of our BHJ films, we prepared a series of sequentially-processed active layers by first spinning a ~110-nm thick layer of P3HT from *o*-dichlorobenzene, and then we subsequently deposited PCBM layers from either 5%, 10% or 15% wt/wt dichloromethane solutions on top by spin-coating, leading to P3HT/PCBM films with a total thickness in the range of 155 to 185 nm. We then prepared BC

	M_n (kDa)	Regioregularity	PDI	Mobility (SCLC) ($cm^2\ V^{-1}\ s^{-1}$)
Low RR (LR) P3HT	~50-60	~94%	~2.20	1.6×10^{-5}
16k High RR (HR) P3HT	15.9	98%	1.18	3.4×10^{-5}
37k High RR (HR) P3HT	36.9	98%	1.19	1.3×10^{-5}

Table 2.1. Characteristics of P3HT used in this work.

active layers (~175 nm thick) by spinning a composite P3HT:PCBM (1:0.9 weight ratio) solution from *o*-dichlorobenzene at 1000 rpm for 60 s. Identical active layers were used to fabricate photovoltaic devices with Ca/Al evaporated on top as the cathode.

We note that no slow drying of solvent or solvent vapor treatments were performed on either the sequentially-processed or BC devices, even though such treatments are necessary to optimize the PCE for the P3HT/PCBM materials combination. Instead, we chose our spin-coating parameters to provide us with completely dry films after spinning. We made this choice to eliminate drying kinetics, which can cause marked variations in the performance of BC devices.[47,70] In this way, we were able to maintain our focus on how polymer properties such as regioregularity and molecular weight control variations in morphology and device performance.

2.3. Results and Discussion

In this section, we begin by discussing the hole mobility of the three polymer batches we investigate in this work (Table 2.1). Although we find that polymer regioregularity and molecular weight do slightly affect hole transport, the differences we observe are subtle, suggesting that BHJ morphology is a much larger factor in determining device performance than the raw hole mobility of the bare polymer. We then use these different polymer batches to fabricate SqP and BC solar cells, and demonstrate that polymer regioregularity has the opposite effect for the two different processing techniques in terms of photovoltaic device efficiency. This result can be understood through a series of morphological studies, including thin film absorption, fluorescence quenching and grazing incidence X-ray scattering measurements, which allow us to directly explore the structural changes that occur upon thermal annealing and to define the optimal conditions needed to create ideal morphologies for BC and SqP solar cells.

2.3.1. The Device Physics of BC and SqP Solar Cells Made From Different P3HTs

2.3.1.1. Hole Mobility of Different P3HTs

Many groups have examined how the mobilities of P3HT films are controlled by different polymer properties, such as the regioregularity and/or molecular weight.[63,64,71–75] The generally accepted trend is that increasing regioregularity and increasing molecular weight lead to higher charge carrier mobilities,[73] although such measurements are made on field-effect transistors (FETs).[76] Since the direction of charge transport for photovoltaic devices is perpendicular to that in FETs, we chose to examine the carrier mobilities in our P3HT batches in sandwich-structure devices so that our measurements would be directly relevant for the performance of these materials in solar cells.

We fabricated diodes from each batch of P3HT using an architecture of ITO/PEDOT:PSS/P3HT/Au to ensure that the majority carriers in the device are holes. We then fit the corresponding dark *J-V* curves using the space-charge limited current (SCLC) model, yielding the mobilities listed in Table 2.1. The 16k HR P3HT shows the highest hole mobility, a bit over twice that of the LR P3HT, which has a molecular weight of roughly 50 kDa. Surprisingly, the 37k HR P3HT shows the lowest mobility, even though it has the same regioregularity as the 16k HR batch but a higher molecular weight. These results indicate that P3HT hole mobility has a complex dependence on both regioregularity and molecular weight. We note, however, that the hole mobilities for all three P3HT batches all fall within a factor of 2.6. This suggests that when these different P3HTs are employed in photovoltaic devices, all else being equal, differences in hole mobility are not likely to explain any significant difference in device performance. This allows us to use these batches to understand how differences in

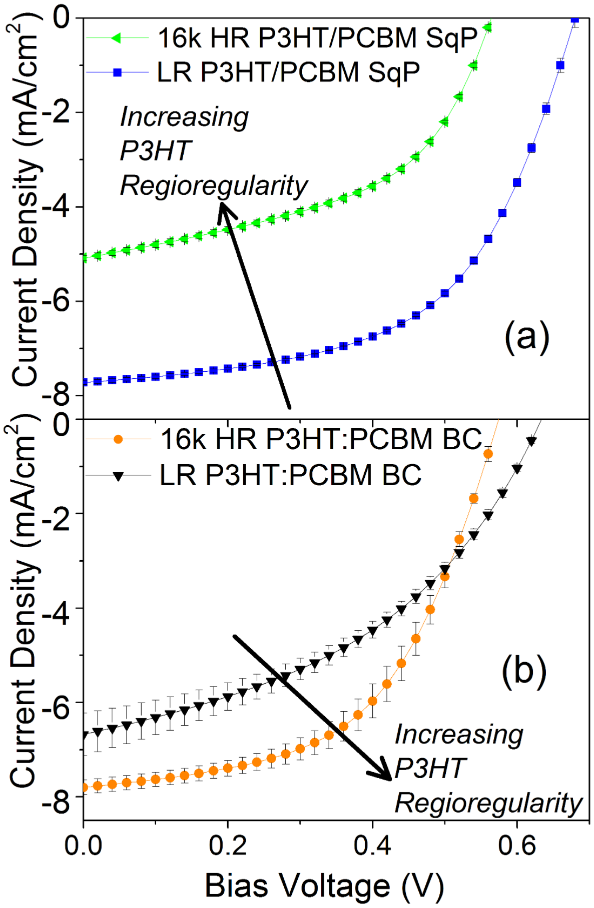

Figure 2.1. Current density versus applied bias for (a) ITO/poly(ethylene-dioxythiophene):poly(styrenesulfonic acid)(PEDOT:PSS)/P3HT/PCBM/Ca/Al sequentially-processed solar cells and (b) ITO/PEDOT:PSS/P3HT:PCBM/Ca/Al BC-BHJ solar cells under AM-1.5 illumination. The SqP active layer was made by spinning 5 mg/mL PCBM solution onto a 110 nm P3HT underlayer (see SI). All of the SqP and BC films were thermally annealed at 150 °C for 20 min prior to deposition of the cathode. The error bars show 1 standard deviation in measurements over at least 12 independent devices. Although error bars can be clearly seen in panel (b), they are comparable to or smaller than the symbols used to plot the data in panel (a), indicating that SqP devices are more reproducible than BC devices.

regioregularity and molecular weight result in morphology differences that affect solar cell performance, and how these differences depend on the processing route chosen to make the BHJ active layer.

2.3.1.2. Comparing the Performance of SqP and BC Devices with Controlled P3HT Regioregularity and Fullerene Composition

To determine the effect of polymer regioregularity/crystallinity on the performance of the solar cells with different active-layer processing methods, we constructed working photovoltaic devices with both SqP and BC active layers from both the 16k HR P3HT and LR P3HT batches. Figure 2.1 demonstrates the *J–V* characteristics of the devices under AM 1.5 solar illumination; the data plotted are the average *J–V* curves from at least twelve separate devices, and the error bars (which in some cases are smaller than the symbols used to plot the data) are ±1 standard deviation. The full *J–V* characteristics for all the devices we studied are detailed in Table 2.2. The data shows clearly that even though SqP devices require one more spin-coating step than BC devices, SqP devices can be fabricated far more reproducibly. This is because SqP avoids the kinetic sensitivity of the BHJ morphology that is inherent with BC processing.[42]

The most interesting result from Figure 2.1 is the fact that the two P3HT batches show opposite performance trends, depending on the processing method used to make the devices. The SqP solar cells made with LR P3HT show *J–V* characteristics similar to those published previously,[32] with average open circuit voltage $V_{oc} = 0.68$ V, short circuit current $J_{sc} = 7.2$ mA cm^{-2}, fill factor $FF = 56\%$ and PCE = 2.9%. The HR P3HT batch, however, makes poorer SqP devices with J_{sc} values of only ~5.1 mA cm^{-2}, and PCE of only ~1.4%. In contrast, the HR P3HT:PCBM BC devices have a significantly higher J_{sc} and ~40% higher PCE compared to the

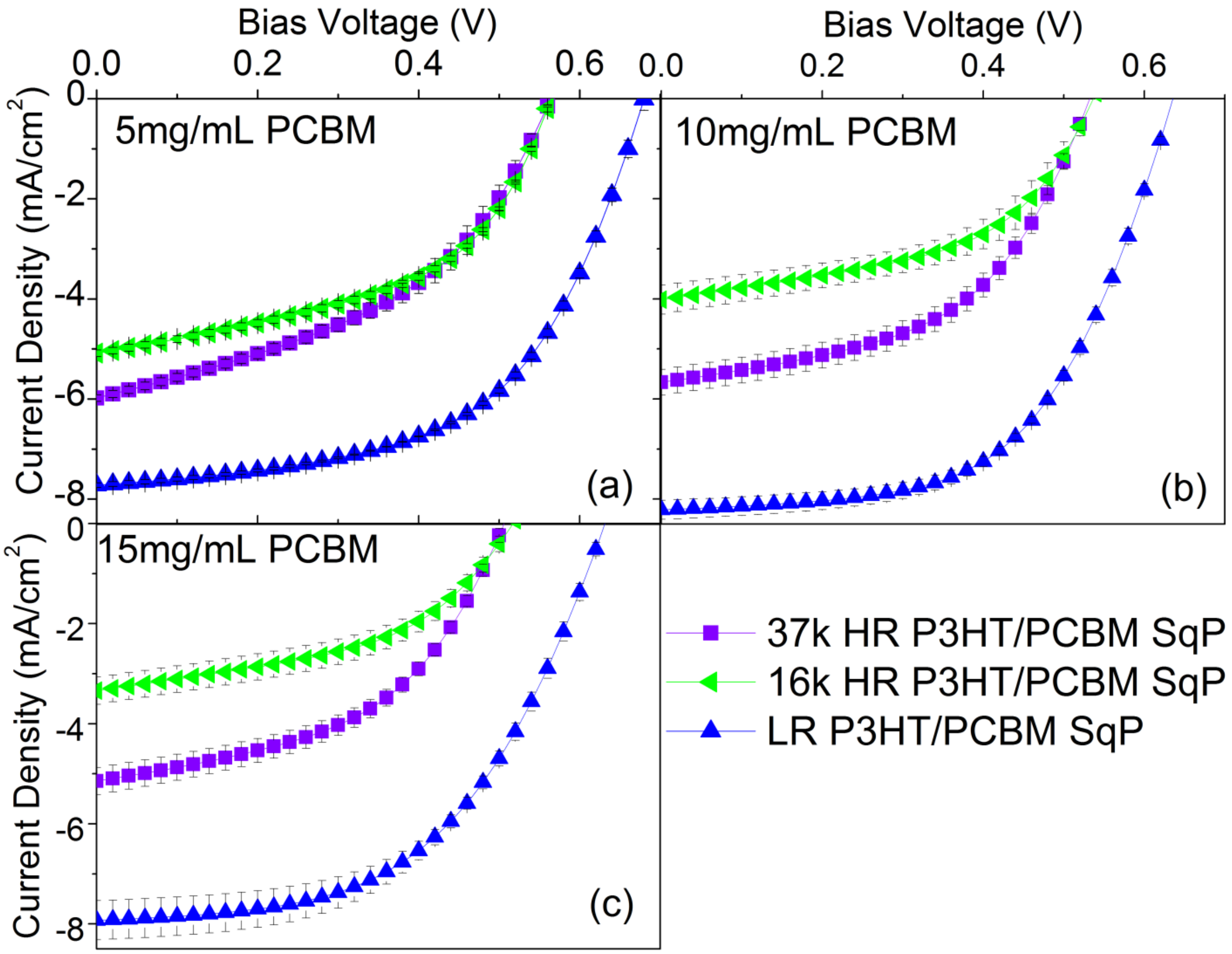

Figure 2.2. Effect of molecular weight, regioregularity and film composition on the *J–V* characteristics of P3HT/PCBM devices made via SqP. LR P3HT (blue up-triangles) and two HR P3HTs with different molecular weights, e.g. 37k Da (violet squares) and 16 kDa (green left triangles) are used as underlayer. All P3HT underlayers were kept at ~110 nm. Three different concentrations of PCBM (5 mg/mL, 10 mg/mL and 15 mg/mL) were spun on top of the P3HT underlayers from DCM and the corresponding *J–V* curves are shown in panels (a), (b) and (c), respectively. The total thicknesses of the active layers are 155 nm, 169 nm and 185 nm with increasing PCBM solution concentratio, respectively. All samples were annealed at 150° C for 20 min before deposition of the Ca/Al cathode. The error bars show 1 standard deviation for measurements over at least 12 independent devices.

BC devices fabricated with LR P3HT. Thus, the way polymer regioregularity/crystallinity affects device performance is not a simple material property, but instead depends on the route via which the active BHJ layer is processed.

To understand why changing the polymer regioregularity leads to opposite changes in performance for SqP and BC devices, we performed a series of control experiments to verify that the performance changes we observed did not result from changes in the polymer molecular weight or the polymer:fullerene composition of the active layer. Figure 2.2 and Table 2.2 summarize the *J–V* characteristics of SqP solar cells made from the 16k HR P3HT (green triangles) and LR P3HT (blue squares), as well as the 37k HR P3HT (violet squares). The in-house synthesized 37k HR P3HT batch has the same high regioregularity and low PDI as the 16k HR P3HT, but a molecular weight closer to that of the commercial LR P3HT. The V_{oc} and *FF* of the 37k HR batch are similar to the 16k HR P3HT, but the overall PCE is higher, mainly due to increased J_{sc}. However, even though increasing the molecular weight improves the device performance, we see that the LR P3HT still shows superior performance for devices fabricated by SqP. Thus, for SqP devices, the overall performance is governed more by the degree of P3HT regioregularity instead of the polymer molecular weight.

In addition to polymer regioregularity, the performance of OPVs also depends sensitively on the overall polymer:fullerene composition,[48,77] a factor that is directly controlled using the ratio of polymer to fullerene in the casting solution in BC processing. In SqP, by contrast, the composition is indirectly controlled by the relative solution concentrations and spin speeds used to deposit each component of the active layer. Figure 2.2 thus illustrates the change in SqP solar cell performance with different polymer:fullerene compositions. In these experiments, we fixed the thickness of the P3HT underlayer and increased the concentration of the PCBM solution spun

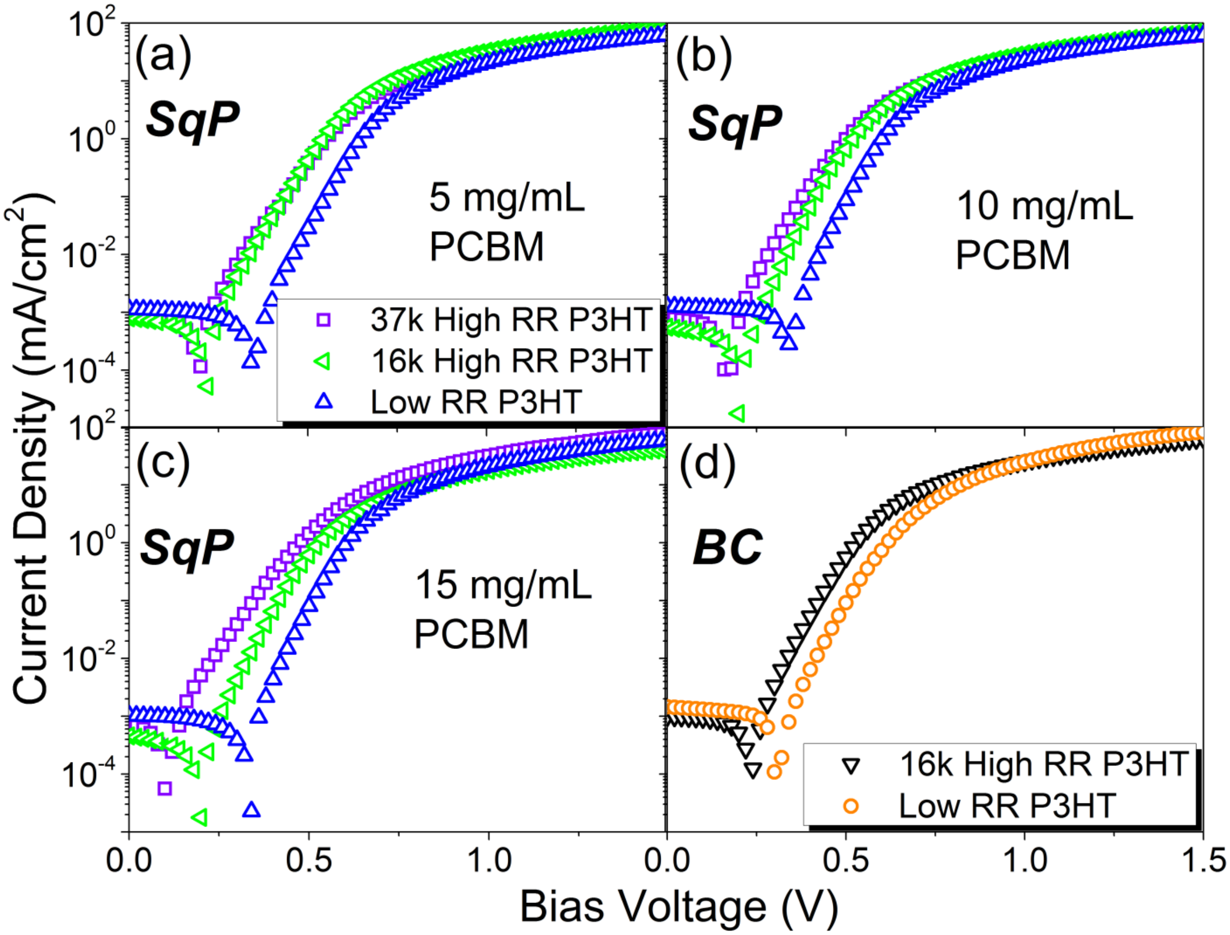

Figure 2.3. Dark *J-V* characteristics of the same SqP devices in Figure 2.2 and the same BC devices in Figure 2.1.

on top. We find that with increasing fullerene loading in SqP active layer, the LR P3HT-based devices show only slight variations in J_{sc}, with an optimal polymer/fullerene composition obtained when the PCBM overlayer is spun from a 10 mg/mL solution.[32] In contrast, the performance of the SqP devices based on HR P3HT continually decreases with increased PCBM loading. Thus, not only does increased P3HT regioregularity lead to poorer SqP device performance, the results also imply that the introduction of extra fullerene cannot be accommodated in pre-formed high-RR P3HT underlayers.

We also have performed identical experiments exploring the changes in device performance for different batches of P3HT with different fullerene compositions for BC devices. We find, in agreement with the literature, that increased P3HT regioregularity is beneficial to BC device performance. Surprisingly, however, we find that for BC devices made from the 16k HR P3HT, the optimal P3HT:PCBM weight ratio is 1:1.3, significantly higher than the 1:0.9 optimal ratio typically seen in the literature (with lower regioregular, commercially-available P3HT). Thus, for the HR-P3HT, the trend in fullerene loading for optimal BC devices also goes in the opposite direction as that for SqP devices.

2.3.1.3. The Effect of Polymer Regioregularity on BC and SqP Device Physics

To begin our exploration of why polymer regioregularity has opposite effects on solar cells fabricated via BC and SqP, we measured the dark *J–V* curves of the SqP and BC solar cells discussed above; the results are summarized in Figure 2.3 and Table 2.2. Perhaps the most interesting parameter to consider for purposes of this study is the dark ideality factor. Typically the dark ideality factor falls into the range between 1 and 2, although numbers outside this range have been reported mainly due to resistivity effects.[78,79] Within the range of 1 and 2, a larger

	V_{oc} (V)	J_{sc} (mA/cm^2)	*FF*	*PCE* (%)	n_{ideal} (Dark *J-V*)	R_{seires} (Ω-cm^2)	R_{shunt} (×10^5 Ω-cm^2)
37k HR P3HT/PCBM(5mg/mL) SqP	0.56 ±0.01	5.98 ±0.06	0.44 ±0.02	1.48 ±0.07	1.62 ±0.03	11.2 ±2.2	13.0 ±0.3
16k HR P3HT/PCBM(5mg/mL) SqP	0.56 ±0.01	5.08 ±0.06	0.50 ±0.01	1.43 ±0.02	1.62 ±0.03	8.8 ±0.7	7.8 ±0.0
LR P3HT/PCBM(5mg/mL) SqP	0.68 ±0.01	7.72 ±0.04	0.56 ±0.01	2.92 ±0.02	1.43 ±0.02	10.6 ±0.3	20.8 ±0.4
37k HR P3HT/PCBM(10mg/mL) SqP	0.53 ±0.01	5.67 ±0.26	0.51 ±0.01	1.52 ±0.09	1.88 ±0.03	12.3 ±2.2	12.6 ±0.0
16k HR P3HT/PCBM(10mg/mL) SqP	0.54 ±0.01	4.02 ±0.29	0.50 ±0.03	1.09 ±0.10	1.64 ±0.04	10.7 ±2.1	8.7 ±0.0
LR P3HT/PCBM(10mg/mL) SqP	0.64 ±0.01	8.21 ±0.19	0.57 ±0.01	2.97 ±0.03	1.40 ±0.04	10.9 ±2.1	14.8 ±0.2
37k HR P3HT/PCBM(15mg/mL) SqP	0.51 ±0.01	5.15 ±0.27	0.48 ±0.02	1.26 ±0.12	2.09 ±0.05	9.1 ±1.9	9.5 ±0.0
16k HR P3HT/PCBM(15mg/mL) SqP	0.515 ±0.01	3.34 ±0.27	0.47 ±0.02	0.82 ±0.08	1.64 ±0.05	18.3 ±1.9	10.0 ±0.0
LR P3HT/PCBM(15mg/mL) SqP	0.636 ±0.01	7.93 ±0.39	0.52 ±0.02	2.63 ±0.06	1.43 ±0.05	10.8 ±2.0	82.2 ±21
16k HR P3HT:PCBM BC	0.58 ±0.01	7.80 ±0.15	0.53 ±0.03	2.39 ±0.14	1.51 ±0.02	11.2 ±1.5	22.6 ±0.0
LR P3HT:PCBM BC	0.64 ±0.01	6.68 ±0.45	0.42 ±0.01	1.79 ±0.07	1.65 ±0.07	6.9 ±1.4	7.4 ±0.1

Table 2.2. Summary of Device Parameters

ideality factor is considered as a strong indication of increased trap-assisted recombination in the device, whereas lower ideality factors are more reflective of bimolecular recombination.[80–82] We derived the ideality factors for our SqP and BC devices in Table 2.2 from the slope of the linear regions in Figure 2.3; we find that the ideality factors mirror the trends in device performance. For SqP devices with a given fullerene concentration, the ideality factors for devices based on LR P3HT are consistently lower than those fabricated with HR P3HTs. For BC devices, the opposite is true: the HR P3HT-based devices exhibit lower ideality factors than the LR P3HT-based devices. This implies that the polymer/fullerene interfacial trap distribution is quite different for the different BHJ morphologies formed through the two different processing techniques.

Based on the data presented above and the structural data presented below, we offer the following picture for the changes in device physics with polymer regioregularity. Low P3HT regioregularity typically leads to more amorphous regions in BHJ films made from the traditional blend-casting method. Since there are fewer crystalline polymer regions and more structural disorder, there is a greater degree of trap-assisted recombination. In contrast, increasing the polymer regioregularity in SqP devices causes the ideality factor to increase no matter what fullerene loading is used. This suggests that pre-existing P3HT underlayers can support only a certain amount of PCBM, an amount presumably limited by the fraction of the polymer that lies within amorphous regions. Thus, increasing the polymer regioregularity decreases the available space for fullerene intercalation, so that increased regioregularity leads to poorer device performance. If one tries to compensate for this by increasing the fullerene concentration in SqP devices, large-scale phase separation of the fullerene from the highly crystalline polymer network occurs, leading to an increase in the fraction of structural traps and thus trap-assisted recombination, as seen with the increased ideality factor.

Finally, we note that the devices made with different batches of P3HT also have slightly different V_{oc}'s. The trend that V_{oc} is lower in both SqP and BC devices with HR P3HT correlates with the concomitant red-shift of the absorption spectrum, described further below. This red-shift results from the fact that the highest occupied molecular orbital (HOMO) increases slightly in energy with increasing regioregularity of P3HT because of enhanced delocalization.[83,84] It is also known that increasing the amount of trap-assisted recombination can result in decreased V_{oc}, particularly for devices with carrier mobilities similar to those used here.[85] Since we indeed find that HR P3HT shows more trap-assisted recombination in the SqP devices but less in BC devices, this can help us explain the fact that the V_{oc} decrease observed in BC devices (0.06 V) is smaller than that seen in SqP devices (>0.1 V): the recombination effect goes in the same direction as the HOMO level effect in determining V_{oc} for the SqP devices while the two effects partially compensate in BC devices.

2.3.2. Understanding How P3HT Crystallinity Affects the BHJ Architecture for SqP and BC OPVs

Now that we have shown that polymer regioregularity causes opposite effects in SqP and BC photovoltaic device performance, we turn in this section to study how regioregularity affects the active layer morphology in both SqP and BC films. To this end, we perform thin-film absorption, fluorescence quenching, and grazing incidence wide-angle X-ray scattering (GIWAXS) to examine differences in the active layer morphologies formed via SqP and BC.

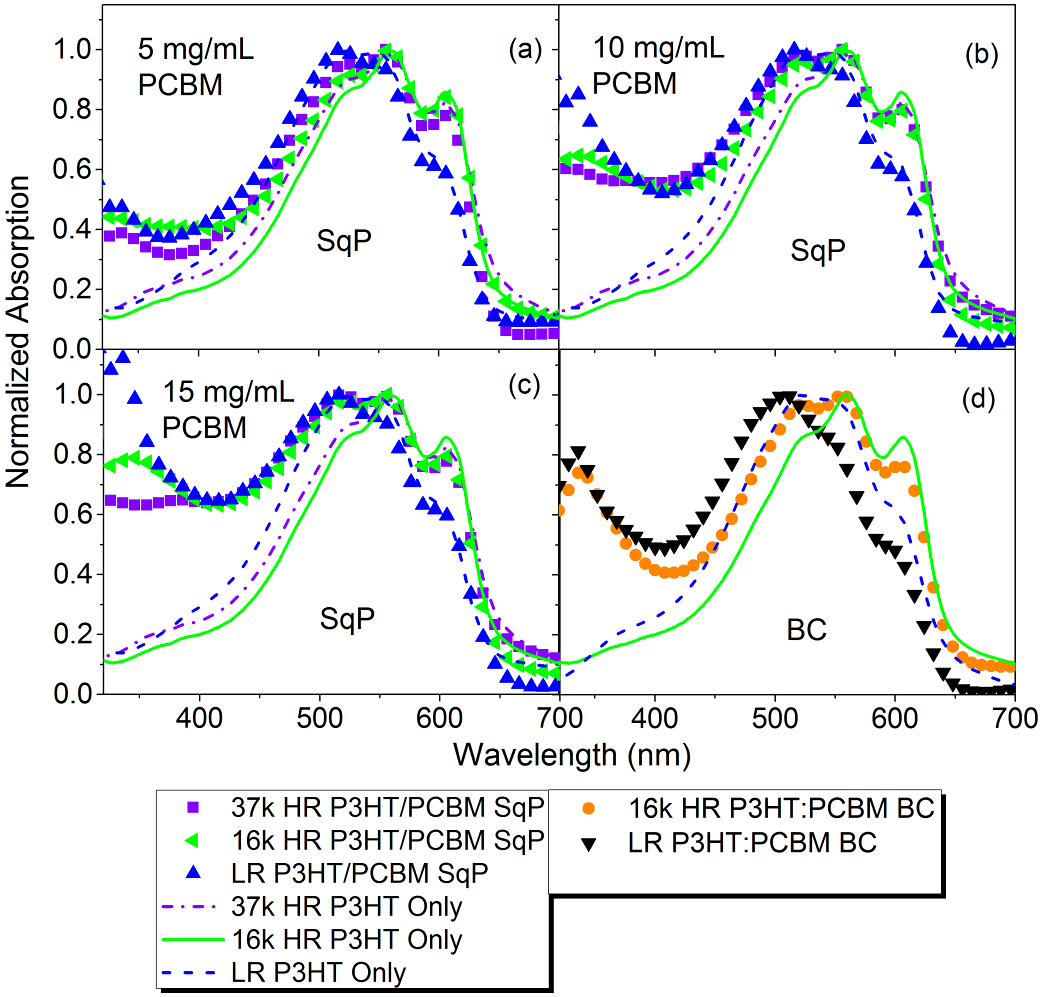

Figure 2.4. UV-visible absorption spectra of thin films made from different batches of pure P3HT (solid dashed and dash-dotted lines) and SqP P3HT/PCBM films (symbols) made from the same P3HTs with **(a)** 5 mg/mL PCBM, **(b)** 10 mg/mL PCBM and **(c)** 15 mg/mL PCBM spun on top; and **(d)** BC P3HT:PCBM films made from the same P3HTs. The pure P3HT films were 110 nm thick in all cases. All films were thermally annealed at 150 °C for 20 minutes and the spectra in both panels are normalized to the highest polymer optical density (i.e. highest OD red of 490 nm) for ease of comparison.

2.3.2.1. UV-Vis and PL of SqP and BC Active Layers with Different P3HT Regioregularities

Figure 2.4 shows the UV-Visible absorption spectra of pure P3HT films from each of the different polymer batches as well as spectra for all of the SqP and BC active layers discussed above. The spectra of the pure LR P3HT (dashed curve) is shifted to the blue by about 13 nm compared to the HR P3HT (solid and dash-dotted curve), and the relative intensity of the vibronic peaks is also different. Both Spano[86,87] and others[88–90] have shown that the ratio of the intensity of the 0-0 peak ($A_{0\text{-}0}$) to the 0-1 peak ($A_{0\text{-}1}$) is directly related to the intermolecular coupling and thus the crystallinity of P3HT. For our polymer batches, we observe higher $A_{0\text{-}0}/A_{0\text{-}1}$ ratios for the 37k and 16k HR P3HT than for the LR P3HT, indicating higher crystallinity in the HR P3HT films. The slight decrease of $A_{0\text{-}0}/A_{0\text{-}1}$ for the 37k HR P3HT sample compared to the 16k sample indicates the crystallinity of the polymers is slightly affected by their molecular weights. Despite this, the data suggest the polymer regioregularity is the most important factor in determining the film crystallinity.

The symbols in Figures 4(a)-(c) show the absorption spectra of the same P3HT films after sequential deposition of a PCBM overlayer and subsequent thermal annealing at 150 °C for 20 minutes. We find that for all three P3HT batches, the SqP film absorption is nearly identical to that of the pure polymer, indicating that the fullerene incorporated into the film through sequential processing induces little disruption to the crystalline polymer domains.

The band seen near 340 nm in the BHJ films in Figure 2.4 arises primarily from the absorption of PCBM, although there is some residual absorption of P3HT at this wavelength. Since the pure P3HT absorption at 340 nm is nearly identical for all three polymer batches, we can use the 340-nm peak intensity to roughly evaluate the PCBM content in each of the SqP films (but see Ref. 42). For SqP films with the PCBM overlayer cast from a 5 mg/mL solution, the fullerene content of the films is quite similar, suggesting that any of the underlayer films can accommodate the relatively modest amount of fullerene provided by the dilute solution. For SqP active layers produced using more concentrated PCBM solutions, however, the HR P3HT samples show much weaker fullerene absorption than LR P3HT sample. This confirms that higher crystallinity polymers are less able to incorporate fullerene during SqP; if there are fewer amorphous regions into which PCBM can penetrate into the bulk of the film, more of the fullerene is likely to simply spin off during deposition of the over-layer. In Figure 2.5, we show optical micrographs of these films whose absorption spectra are shown Figure 2.4; the films made from HR P3HT batches with high PCBM concentrations spun on top show fullerene aggregates/crystals at the μm-length scale, consistent with the idea that sequentially-processed high crystallinity films cannot accommodate significant fullerene loadings.

Unlike the sequentially-processed films, whose absorption spectra do not change upon the addition of fullerene, the vibronic features in the absorption spectra of P3HT:PCBM BC films (Figure 2.4(d)) are strongly altered by the presence of fullerene. For the LR P3HT flim, the vibronic peaks have a dramatcially decreased intensity relative to the pristine P3HT, even after 20 minutes of thermal annealing at 150 °C. This suggests for LR P3HT, the presence of fullerene hinders the crystallization of P3HT during both the spin-coating and thermal annealing processes. In the case of the HR P3HT:PCBM BC films, although the A_{0-1}/A_{0-0} ratio does not remain constant as observed in the seqentially processed films, it does not decrease as strongly as in the LR P3HT:PCBM BC-BHJ films. Thus, this data suggests that even in BC films, the inherent crystallinity of HR P3HT can be better retained than that of LR P3HT.

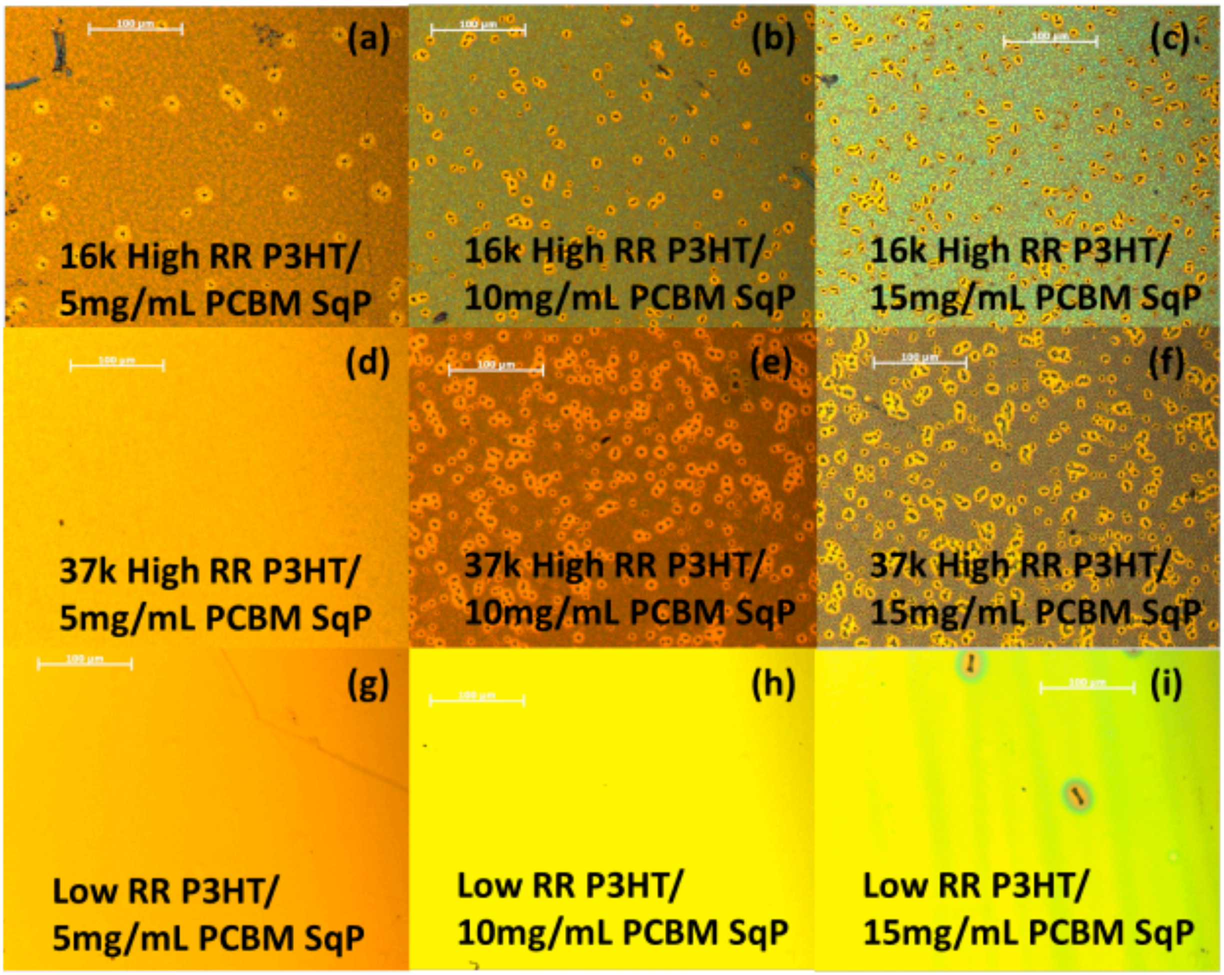

Figure 2.5. Optical microscopy images of thermally annealed films with three batches of P3HTs and three different PCBM concentrations pun on top of each other. The scale bar is 100 µm.

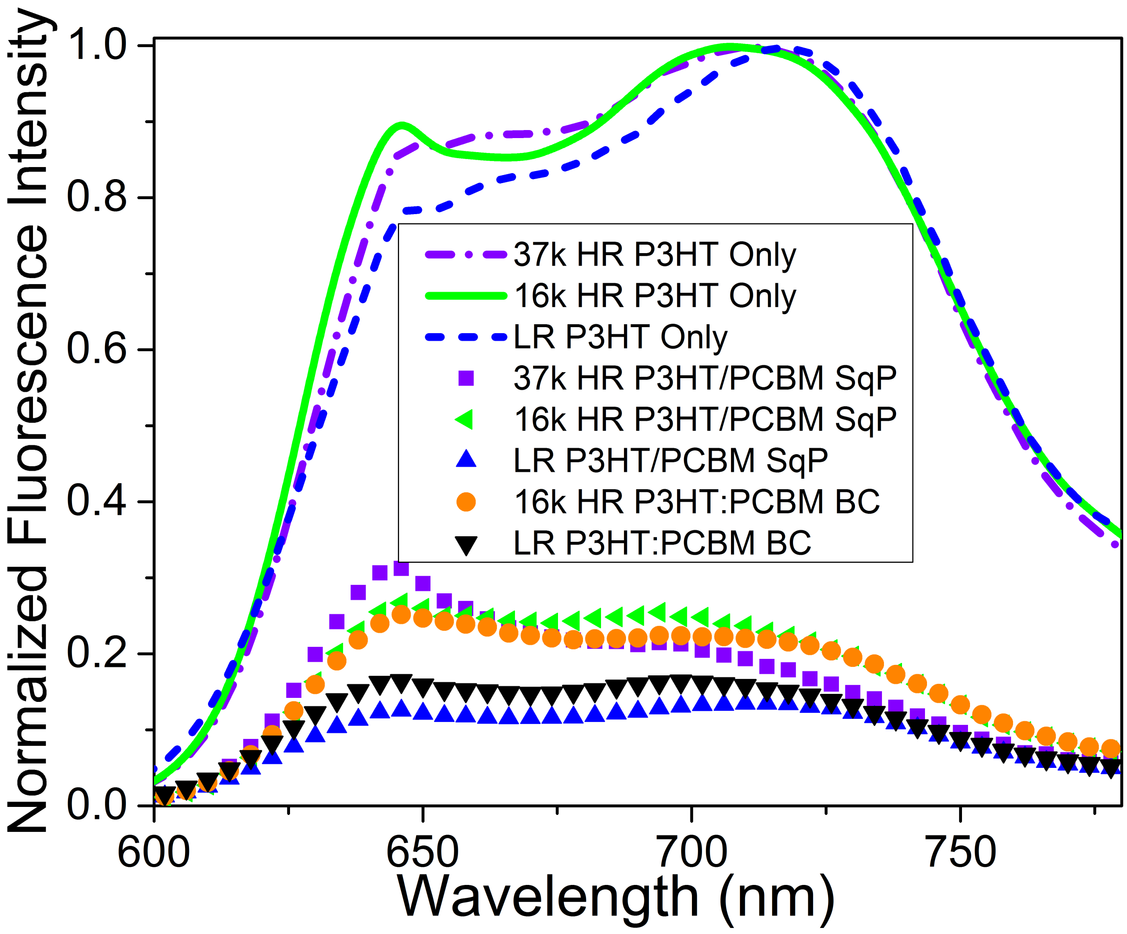

Figure 2.6. Photoluminescence (PL) spectra of thin films made from: pure P3HTs (same as Figure 2.4a), SqP P3HT/PCBM films (same as Figure 2.4a) and P3HT:PCBM BC films (same as Figure 2.4d). The measured PL intensities were divided by each film's optical density at 530 nm, the excitation wavelength used in this experiment. and then normalized to the highest PL value (that of the pure 16k HR P3HT film) to best illustrate the extent of PL quenching in the different samples.

In addition to UV-Visible spectroscopy, we also performed a series of photoluminescence (PL) quenching experiments of SqP and BC P3HT:PCBM films made from the different polymer batches, the results of which are shown in Figure 2.6. The PL spectra of the pure P3HT polymer films are similar, with only slight differences in the relative height of the 0-0 peak near 650 nm that reflect the changes in intermolecular coupling with the degree of polymer crystallinity,[86] in agreement with the UV-Visible data in Figure 2.4. Overall, the trends observed in BC and SqP films are very similar. HR samples show less PL quenching in all cases compared to LR samples, a result that indicates that the equilibrium (i.e. post-annealing) extent of polymer-fullerene mixing at the molecular scales is driven primarily by polymer regioregularity and not by the processing method. This result is particularly interesting in light of the facts that HR material produces the best BC devices while LR material gives SqP devices with the highest efficiency. The results thus emphasize how the same level of atomic-scale mixing must be accompanied by very different nanoscale architecture using the two different processing methods. For a separation-based process like BC, strong separation appears to drive the formation of an optimized nanoscale architecture. By contrast, for a mixing-based process like SqP, a strong driving force for mixing is needed to create that same ideal architecture.

2.3.2.2. The Morphology of SqP and BC Films with Different Batches of P3HT Measured by X-Ray Diffraction

To directly investigate how changes in the P3HT regioregularity affect the polymer and fullerene crystallinity for the different processing routes used to make BHJs, we performed a series of two-dimensional (2-D) grazing incidence wide-angle X-ray scattering (GIWAXS) measurements. For these experiments, we used all the same processing methods described above, but instead spun the active layer materials onto silicon substrates. Our GIWAXS measurements were performed at the Stanford Synchrotron Radiation Light Source on beamline 11-3 using a wavelength of 0.9742 Å. We should note that the absolute diffraction intensities cannot be compared between SqP and BC data sets because of different beam intensities during separate experimental runs; the relative intensities for a single processing method, however, can be meaningfully compared within each set. Below, we show only radially-integrated scattering data. The results from our GIWAXS measurement are summarized in Figure 2.7 and Table 2.3.

2.3.2.2.1. The Polymer Diffraction in SqP Samples

We begin our discussion by examining the P3HT (200) peaks, located between 0.77 – 0.79 $Å^{-1}$, which arise from P3HT lamellar interchain stacking. The (200) peak is mostly distributed in the out-of-plane direction due to the dominant "edge-on" orientation of the P3HT chains relative to the substrate. For the as-cast SqP films (dashed curves), the integrated (200) peak area of the 16k HR P3HT is more than six times higher than that of the LR P3HT. The peak center of the HR P3HT is also positioned at higher Q than that of LR P3HT, which indicates more compact lamellar stacking for the HR P3HT. We note that in polymeric systems, the broadening of x-ray scattering peaks results from disorder in the polymer domains, rather than from the finite size of crystallites as seen in crystalline materials.[21,91,92] Thus, the FWHM or coherence lengths reported here are those derived from the Scherrer equation, even though the size of the crystalline polymer domains are likely smaller. In Table 2.3, the two P3HT batches show similar FWHM for the (200) peaks. From this data, we conclude that a larger fraction of the as-cast HR P3HT-based SqP samples is crystalline, but the crystallites in both films have similar coherence lengths.

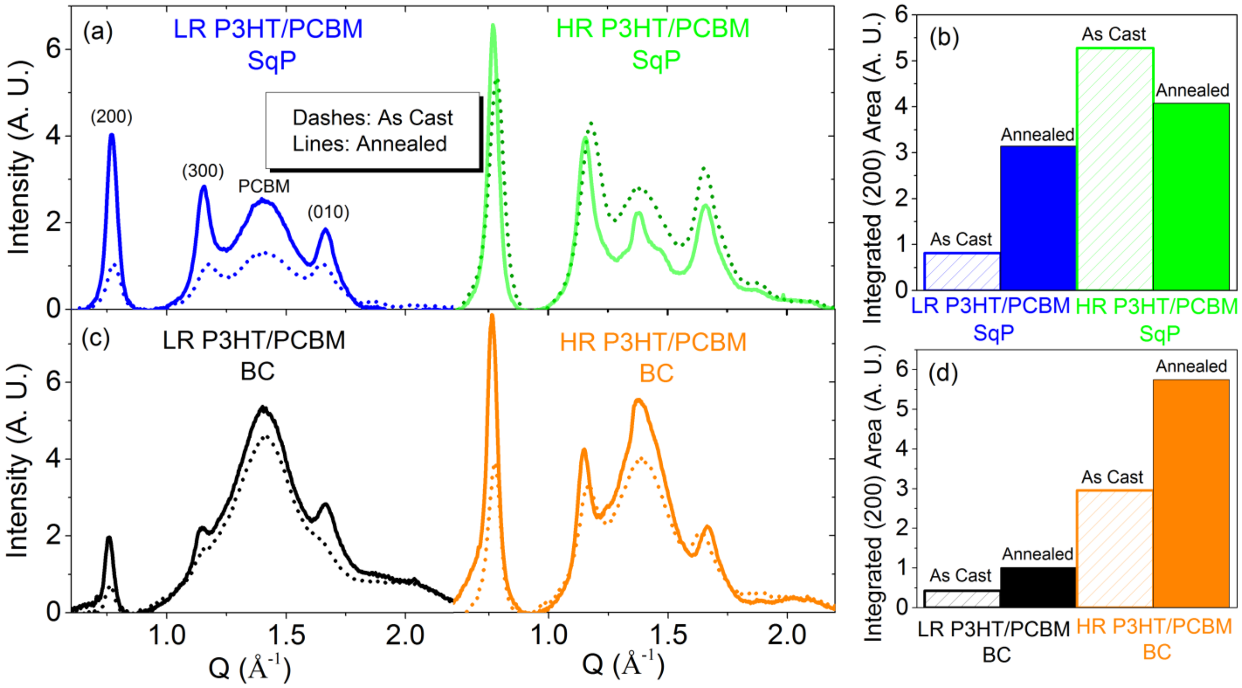

Figure 2.7. (a) Radially-integrated 2-D GIWAXS intensities for P3HT/PCBM sequentially processed active layers cast on a silicon substrate for LR and HR P3HT. In each case, the P3HT film thickness was 110 nm, and the PCBM over-layer was spun from a 5mg/mL solution. (b) Integrated peak area for the (200) polymer peak for SqP. (c) Integrated GIWAXS intensity for P3HT/PCBM BC films. (d) Integrated peak area for the (200) polymer peak for BC-BHJ films. Dashed lines indicate as-cast films and solid lines are after 20 min of thermal annealing at 150 °C for both (a) and (c).

	(200) Peak Position (Å^{-1})	(200) Peak Area (A. U.)	(200) FWHM[a] (10^{-2} A^{-1})	(010) Peak Position (Å^{-1})	(010) Peak Area (A. U.)	(010) FWHM[a] (10^{-2} A^{-1})
LR P3HT/PCBM SqP As Cast	0.778	8.1	6.6	1.657	10.9	10.7
LR P3HT/PCBM SqP Annealed	0.770	31.4	5.6	1.664	13.5	7.7
16k HR P3HT/PCBM SqP As Cast	0.787	52.8	6.9	1.655	35.4	10.0
16k HR P3HT/PCBM SqP Annealed	0.770	40.8	5.1	1.662	23.3	8.9
LR P3HT:PCBM BC As Cast	0.766	4.3	4.6	1.627	15.7	14.9
LR P3HT:PCBM BC Annealed	0.759	10.1	3.9	1.663	29.8	12.0
16k HR P3HT:PCBM BC As Cast	0.776	29.6	5.5	1.634	20.1	11.6
16k HR P3HT:PCBM BC Annealed	0.761	57.4	5.1	1.663	15.0	8.1

Table 2.3. Summary of Parameters from GIWAXS

The HR samples also show closer packing than the LR P3HT-based samples, a fact that likely arises from increased ordering of the hexyl tails in the HR films.

The literature suggests that thermal annealing of SqP films serves the dual roles of facilitating fullerene diffusion into the polymer underlayer and helping to further crystalize amorphous polymer domains.[46,93] Indeed, the solid curves in Figure 2.7(a) show that for both batches of P3HT, annealing causes the (200) peaks to become sharper, indicating the formation of more ordered P3HT domains with larger structural coherence lengths. The change in the intensity of the (200) peak area upon thermal annealing, however, is quite different for the different SqP P3HT batches. For the LR P3HT, annealing increases the peak area by over a factor of three, a result similar to previous studies on BC devices. Surprisingly, the peak area for the HR P3HT actually decreases upon thermal annealing, indicating that annealing this particular polymer/fullerene blend makes the film *less* crystalline. Further investigation reveals that unlike the LR P3HT, where annealing causes essentially no shift of the (200) peak, the HR P3HT (200) peak center also shifts slightly towards lower Q, indicating the d-spacing between the lamellar planes becomes larger after annealing. This likely results from small amount of PCBM diffusing into the P3HT crystallites.

We next turn to investigate the trends of the (010) peak, which corresponds to the polymer π-π stacking direction and is therefore important for charge delocalization and transport. We find that the same general trends with polymer regioregularity and thermal annealing observed for the (200) peak also hold in the (010) direction for our SqP films. For the LR P3HT, however, the increase in (010) peak area upon annealing is less dramatic than that observed for the (200) peak, but the decrease in (010) peak width upon annealing is greater. These data thus indicate that in the (010) direction, thermal annealing predominantly affects on the crystalline coherence length, likely from improvements in π-π stacking upon annealing. For the HR SqP P3HT samples, we saw that the diffraction peaks decrease in intensity upon thermal annealing, and that the decrease of the (010) peak area is slightly greater than the decrease seen in the (200) direction. Overall, the change in both peak with and peak area are qualitatively similar for the (010) and (200) peaks, suggesting that for SqP samples made with HR P3HT, diffusion of PCBM into the film reduces the extent of crystallinity in a fairly isotropic manner, likely by creating amorphous polymer regions where the fullerene can reside. This is in contrast to the LR samples, where annealing of paracrystalline disorder and fullerene diffusion are coupled in a more complex manner.

Clearly, the most significant difference between the two batches of SqP P3HT films is the total amount of amorphous polymer. We believe that a certain amorphous fraction is necessary for the PCBM to penetrate into sequentially processed films. Even though the HR P3HT starts out highly crystalline with few amorphous regions, the thermally induced mixing that drives PCBM into the polymer underlayer actually disrupts the P3HT network by creating additional amorphous regions upon incorporation. This produces the surprising result of a polymer/fullerene sample that becomes less crystalline upon annealing.

2.3.2.2.2. The Polymer Diffraction in BC Samples

In as-cast BC films, the BHJ is formed with the presence of both the polymer and the fullerene, leading to a different morphology than the case of SqP. Based on shifts in diffraction peaks, we find that there is more PCBM intercalation into the BC P3HT network in both the (200) and (010) directions for as-cast BC films relative to SqP films. After thermal annealing, a large amount of the PCBM in BC films is pushed out of the π-π interlayers, as evidenced by a sizable shift towards high Q for the (010) π-stacking peak. This (010) shift upon annealing does not occur with the SqP films. But perhaps more importantly, thermal annealing causes the crystallinity of both the HR and LR P3HT batches to increase when the film is prepared via BC. This provides one reason why the BC devices made from HR P3HT show superior performance compared to those made via SqP.

Another factor that could contribute to the change in device performance with regioregularity is the shape of the polymer crystallites. The widths of the (200) and (010) peaks indicate that the length of the HR P3HT crystallites are shorter than those of the LR P3HT in the (200) direction but longer in the (010) direction. Since the charge carrier transport in the π-π direction is important to the mobility of holes in OPV devices,[91] one might expect hole extraction in HR P3HT active layers to be more efficient than that in LR P3HT samples. Since the hole mobility in P3HT:PCBM blend films is typically lower than the electron mobility,[94] the HR P3HT provides a better mobility-matched active layer and therefore a device with higher fill factor[95] than the LR P3HT BC device, as seen in Figure 2.1.

2.3.2.2.3. The Fullerene Diffraction in SqP and BC Samples

In addition to the changes in the crystallinity of the different batches of P3HT, Figure 2.7 also shows that thermal annealing leads to changes in the crystallinity of the PCBM. For example, the PCBM diffraction (at $q \sim 1.4$ Å^{-1}) in the LR P3HT SqP film shows a significant increase in intensity upon thermal annealing, but the peak remains broad. This is consistent with the formation of many small PCBM crystallites upon thermally annealing SqP LR P3HT films. In contrast, thermal annealing dramatically sharpens the PCBM peaks in the SqP films made with HR P3HT. This indicates that in highly crystalline P3HT, there are too few amorphous regions in which the PCBM can mix with the polymer, so that annealing forces the fullerenes to crystallize into a fewer, but significantly larger domains that are not consistent with an ideal BHJ architecture. These large domains may be accompanied by isolated fullerenes at grain boundaries, but those isolate fullerenes do not diffract and do not create effective conductive paths for photogenerated electrons. This hypothesis is supported by optical images, shown in the SI, which reveal that after thermal annealing, there is optically-visible phase separation of the PCBM in the HR P3HT film.

All of these results make sense in the context of two ideas: first, that PCBM is miscible and mobile only in the amorphous regions of P3HT films,[45,92,96–99] and second, that P3HT only fully crystallizes in the absence of PCBM. The LR P3HT clearly possesses more amorphous regions as-cast, so in SqP films, there is ample opportunity for thermal annealing to cause PCBM to diffuse into the polymer underlayer and form semicrystalline aggregates, as well as for some of the previously amorphous P3HT regions to crystallize. In highly crystalline as-cast polymers, on the other hand, there are almost no suitable amorphous spaces available for PCBM incorporation in SqP devices, so the polymer must partially disorder to make room for fullerene incorporation. Even with this disordering, the majority of the fullerene is still forced to aggregate into large, highly crystalline domains because it cannot mix into the already-crystalline regions of the polymer. In the case of BC films, the high propensity of the polymer to crystallize is important to help drive the phase separation of the polymer and the fullerene. In low regioregularity polymers, the P3HT cannot phase separate as easily, so an ideal interpenetrating BHJ network cannot be formed.

2.4. Conclusions

In summary, we have found that the effects of changing polymer regioregularity and thus crystallinity on active layer morphology and the photovoltaic device performance differ dramatically based on how the active layer is formed. PCBM disperses only into the amorphous regions after sequential processing onto P3HT films, so that controlling the amount of the amorphous phase has a direct impact on the subsequent device performance. SqP of P3HT with too high a polymer regioregularity results in highly crystalline films into which fullerenes cannot easily incorporate even after thermal annealing, leading to unfavorably large scale polymer/fullerene phase separation. SqP films made from P3HT with lower regioregularity possess more amorphous regions, which leads to a better polymer/fullerene network and thus more efficient solar cells. The effect of polymer crystallinity is reversed, however, if the active layer is fabricated through the traditional blend-cast method. The presence of PCBM in the mixed solution prevents P3HT from forming a highly crystalline network. Therefore, more highly regioregular P3HT is favorable because of its stronger propensity to crystallize.

This work has revealed a fundamental mechanism difference for the formation of BHJ active layer morphology between SqP and BC. All of the structural and device performance data show that SqP and BC do not produce films with the same polymer/fullerene morphology, and that different materials parameters affect the film morphology in different ways for the two processing methods. This suggests that the two processing techniques are complementary, and that the appropriate choice of which processing method to use to achieve high efficiency solar cells depends on the details of the particular batch of polymer and fullerene being used.

CHAPTER 3

Polymer/Polymer Blend Solar Cells Using Tetraazabenzodifluoranthene Diimide Conjugated Polymers as Electron Acceptors

3.1. Introduction

Advances in the design and synthesis of hole-conducting (*p*-type or donor) polymer semiconductors[100–102] in the last two decades have enabled major progress in developing increasingly more efficient polymer/fullerene bulk heterojunction (BHJ) solar cells.[8,9,103,104] Since the donor polymer is the main absorber in such fullerene acceptor-based organic photovoltaics (OPVs), the charge photogeneration process critically depends on efficiency of electron transfer from the photoexcited polymer to the fullerene derivative, such as [6,6]-phenyl-C_{60}-butyric acid methyl ester ($PC_{60}BM$) or [6,6]-phenyl-C_{70}-butyric acid methyl ester ($PC_{70}BM$). It is expected that if electron-conducting (*n*-type or acceptor) conjugated polymers can be developed with suitable absorption bands, electronic structures, and high electron mobilities, they could contribute to light harvesting in polymer/polymer (all-polymer) blend BHJ solar cells.[105–116] In such all-polymer solar cells, the efficiency of hole transfer from the photoexcited acceptor polymer to the donor polymer could be as important to the charge photogeneration process, as is the photoinduced electron transfer from the donor to acceptor polymer.[117–119] Understanding of the detailed photophysics and mechanisms of charge photogeneration in polymer/polymer blend solar cells have not yet advanced to the same level as in polymer/fullerene devices in part because of the limited availability of high-mobility *n*-type semicondcuting polymers.

Early studies of all-polymer solar cells were limited to bilayer planar heterojunction devices because of limited processability of the *n*-type or *p*-type polymers.[108,120] Acceptor polymers based on cyano-functionalized poly(*para*-phenylene vinylene)s (CN-PPVs) allowed the study of polymer/polymer blend BHJ solar cells, demonstrating high open circuit voltages (V_{oc}) (~ 1 V) but the efficiencies were limited by low photocurrents.[108,121] *n*-Type semiconducting copolymers derived from 2,1,3-benzothiadiazole moiety have also been explored in all-polymer BHJ solar cells, giving rise to only moderate efficiencies (<2%).[122,123] More recently, availability of perylene diimide (PDI)- and naphthalene diimide (NDI)-based *n*-type semiconducting polymers has enabled the demonstration of polymer/polymer blend BHJ solar cells with improved power conversion efficiencies (~3-5%).[106,107,115,116] Nevertheless, new *n*-type semiconducting polymers, besides NDI- and PDI-based materials, are needed both to enable a broader understanding of structure-photovoltaic relationships and to facilitate improvement of performance of all-polymer solar cells.

In this paper, we report a study of all-polymer blend solar cells based on recently introduced tetraazabenzodifluoranthene diimide (BFI)[124] derivative *n*-type conjugated polymer semiconductor[40] as the electron acceptor component of the active blend layer. The two-dimensional (2D) p-conjugated BFI polymers, exemplified by the 2,5-thienylene-linked PBFI-T (Chart 1), were shown to exhibit unipolar *n*-type charge transport with field-effect electron mobility as high as 0.3 cm^2/Vs.[125] However, their electron-accepting and photovoltaic properties in all-polymer solar cells are yet to be reported. Encouraged by the recent finding that selenophene-linked naphthalene diimide (NDI) copolymers had a superior performance in photovoltaic devices compared to the corresponding thiophene-linked NDI copolymer,[115,116] we herein also report the synthesis and evaluation of a new selenophene-linked BFI

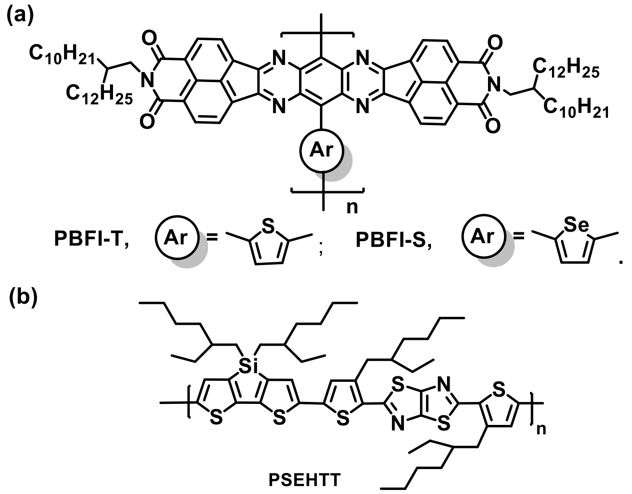

Chart 1. Molecular structures of acceptor polymers (PBFI-T and PBFI-S) (a) and the donor polymer (PSEHTT) (b).

copolymer, PBFI-S (Chart 1), as an acceptor in all-polymer blend solar cells. A known *p*-type semiconducting polymer, poly[(4,4'-bis(2-ethylhexyl)dithieno[3,2-b:2',3'-d]silole)- 2,6-diyl-alt-(2,5-bis(3-(2-ethylhexyl)thiophen-2-yl) thiazole[5,4-d]thiazole)] (PSEHTT, Chart 1),[126,127] was used as the electron donor paired with PBFI-T or PBFI-S in the all-polymer blend solar cells. We found that PBFI-T:PSEHTT blend solar cells had a power conversion efficiency (PCE) of 2.60% whereas the corresponding PBFI-S:PSEHTT cells had a PCE of 0.75%. We show that this unexpected factor of 3.5 difference in the photovoltaic efficiencies of PBFI-T and PBFI-S devices largely originates from the reduced driving energy for hole transfer in the latter blend system among other factors. The bulk charge transport in the blend films was investigated by the space charge limited current (SCLC) technique. Finally, the bulk and surface morphologies of the two photovoltaic blend systems were respectively probed by grazing incidence wide-angle X-ray scattering (GIWAXS) and atomic force microscopy (AFM) imaging.

3.2. Results and Discussion

3.2.1. Synthesis, Optical Absorption and Electronic Structure

The new *n*-type semiconducting polymer, PBFI-S, was synthesized via the Stille cross-coupling copolymerization of the previously reported 8,17-dibromo-7,9,16,18-tetraazabenzodifluoranthene-3,4,12,13-tetracarboxylic acid diimide (BFI-Br2) monomer[124] with 2,5-bis(trimethylstannyl)selenophene,[127] similar to the synthesis of PBFI-T.[40] PBFI-S has excellent solubility in common organic solvents (chloroform, chlorobenzene, toluene, etc) at room temperature. The number average molecular weight (M_n) of PBFI-S, as determined by gel permeation chromatography (GPC) relative to polystyrene standards, is 29.3 kDa with a polydispersity index (PDI) of 3.55. The sample of previously synthesized PBFI-T, which is

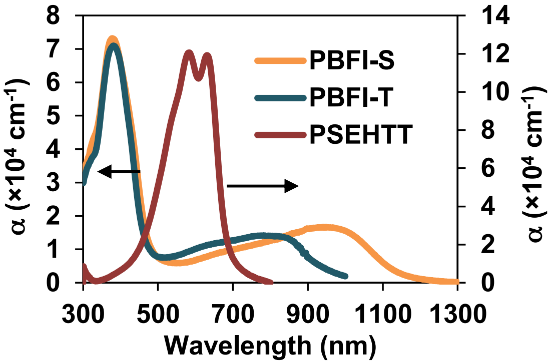

Figure 3.1. Thin film optical absorption spectra of *n*-type polymers (PBFI-T and PBFI-S) and *p*-type polymer (PSEHTT).

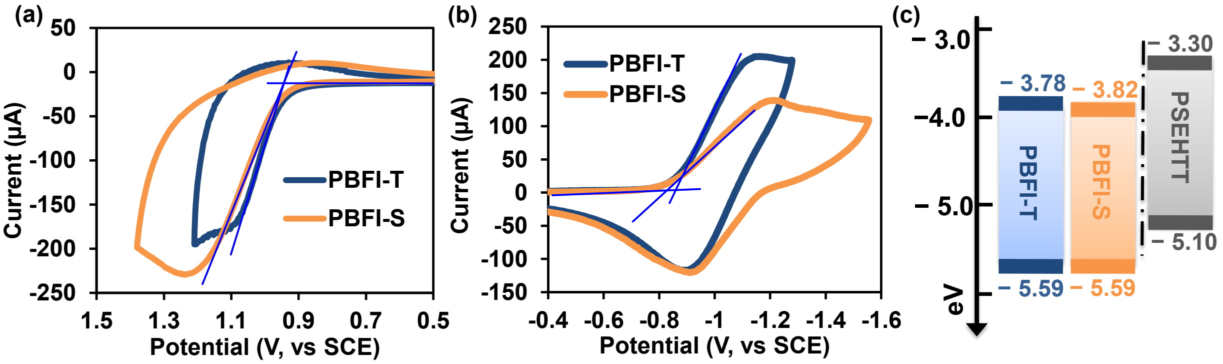

Figure 3.2. Oxidation (a) and reduction (b) cyclic voltammograms of PBFI-T and PBFI-S solid films (in 0.1 M of tetrabutylammonium hexafluorophosphate in CH_3CN with Fc^+/Fc as the internal reference).

investigated here alongside PBFI-S, has an M_n of 61.0 kDa and a PDI of 3.16. Similar to PBFI-T,[125] PBFI-S has excellent thermal stability with an onset thermal decomposition temperature (T_d) of 430 °C from thermogravimetric analysis (TGA) experiments in flowing nitrogen. Differential scanning calorimetry (DSC) scans in the 20-400 °C range did not show any thermal transitions for either polymer.

Figure 3.1 shows the thin film absorption spectra of the *n*-type polymers PBFI-T and PBFI-S, as well as that of the *p*-type polymer PSEHTT. The absorption profile of PBFI-S is very similar to that of PBFI-T; both have a high energy band with identical l_{max} centered at 380 nm (a = 7.3×10^4 cm^{-1}). However, the lower energy absorption band of PBFI-S has a l_{max} = 948 nm (a = 1.7×10^4 cm^{-1}), which is significantly red-shifted (>100 nm) from that of PBFI-T.[125] The absorption edge optical band gap (E_g) of PBFI-S (1.13 eV) is much smaller than that of PBFI-T (E_g = 1.38 eV). The highest occupied molecular orbital (HOMO)/ lowest unoccupied molecular orbital (LUMO) energies of PBFI-T and PBFI-S were determined from the onset oxidation and reduction potentials, respectively, from cyclic voltammograms (Figure 3.2). The HOMO/LUMO energy levels of the proposed donor polymer PSEHTT[41] are also shown in Figure 3.2c for comparison. PBFI-T and PBFI-S have deep LUMO energy levels of −3.78 eV and −3.82 eV, and the same HOMO energy levels of -5.59 eV, potentially providing sufficient driving energy for photoinduced charge transfer and charge separation in blends with PSEHTT.

3.2.2. Photovoltaic Properties

Inverted BHJ solar cells with the structure of indium tin oxide (ITO)/zinc oxide (ZnO)/polymer blend/molybdenum oxide (MoO_3)/Ag (Figure 3.3a) were fabricated to evaluate the photovoltaic properties of the new acceptor polymers (PBFI-T and PBFI-S) based on the

PSEHTT donor polymer. The current density (*J*)-voltage (*V*) characteristics were measured under AM1.5 solar illumination at 1 sun (100 mW/cm^2) in ambient air. The active layer with a blend composition of PBFI-T:PSEHTT (2:1 *wt*/*wt*) showed the optimal performance with a PCE of 2.60%, short circuit current (J_{sc}) of 7.34 mA/cm^2, open circuit voltage (V_{oc}) of 0.67 V and fill factor (FF) of 0.52 (Figure 3.3b, Table 1). In stark contrast, although the optimal PBFI-S:PSEHTT devices consisted of the same blend ratio of 2:1 (*w/w*), their performance was significantly lower with PCE = 0.75%, J_{sc} = 3.43 mA/cm^2, V_{oc} = 0.51 V, and FF = 0.43 (Figure 3.3b). This large difference in performance between PBFI-S and PBFI-T devices is due to the large disparities in V_{oc}, J_{sc} and PCE; in the case of the PCE, PBFI-T cells are a factor of 3.5 superior to those of PBFI-S. These large differences in photovoltaic properties of otherwise two very similar *n*-type polymer semiconductors is very surprising and not obvious from their absorption spectra (Figure 3.1) and electronic structures (Figure 3.2c).

The external quantum efficiency (EQE) spectra of both PBFI-T:PSEHTT and PBFI-S:PSEHTT blend solar cells are shown in Figure 3.3c. The EQE spectrum of the PBFI-T:PSEHTT photodiode shows that the photocurrent turns on at about 950 nm and has peaks of 24% at 380-420 nm and 42% at 560-680 nm. The spectrum covers a broad range from 300 nm to 950 nm, suggesting that both donor (PSEHTT) and acceptor (PBFI-T) polymers contributed to the photocurrent (Figure 3.3c). The J_{sc} calculated from the EQE spectrum is 6.94 mA/cm^2, which is within 6.0% in agreement with the direct *J-V* measurement. The EQE spectrum of PBFI-S:PSEHTT photodiode turns on at around 700 nm, close to the absorption edge of PSEHTT, suggesting that the longer wavelength absorption of PBFI-S did not contribute to photocurrent. The intensity of the EQE spectrum in the 300-700 nm range is also much lower for PBFI-S:PSEHTT than PBFI-T:PSEHTT cells with peaks of 10% at 380-420 nm and 21% at 560-680

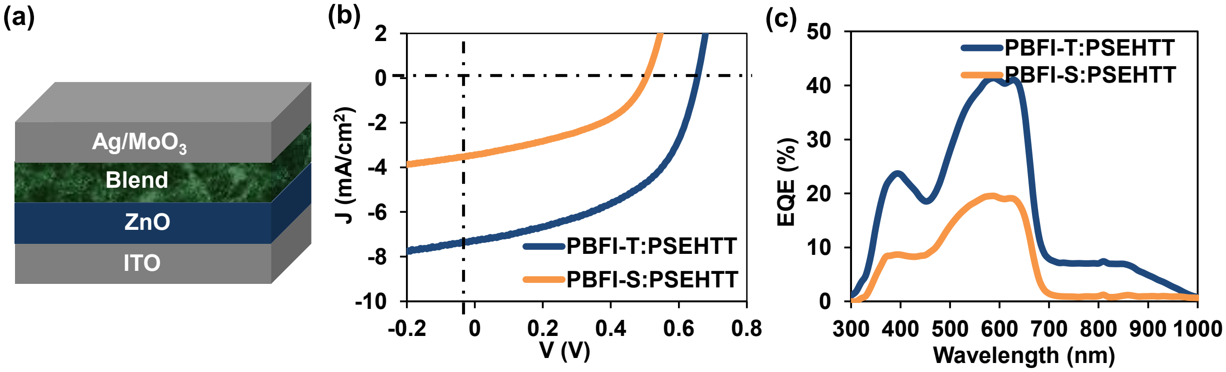

Figure 3.3. Schematic of the inverted all-polymer BHJ solar cell (a), J-V curves (b) and EQE spectra (c) of PBFI-S:PSEHTT and PBFI-T:PSEHTT blend solar cells.

Blend	J_{sc} (mA/cm^2)	V_{oc} (V)	*FF*	PCE (%)	m_e (cm^2/Vs)	m_h (cm^2/Vs)
PBFI-T: PSEHTT	7.34 (7.28±0.0)	0.67 (0.67±0.0)	0.52 (0.52±0.0)	2.60 (2.50±0.1)	2.2×10^{-6}	4.8×10^{-5}
PBFI-S: PSEHTT	3.43 (3.35±0.0)	0.51 (0.51±0.0)	0.43 (0.43±0.0)	0.75 (0.74±0.0)	4.6×10^{-8}	2.7×10^{-5}

[a] Active layers were deposited from the PBFI-X (X = T or S):PSEHTT (2:1 *wt*/*wt*) blend solutions in chlorobenzene, respectively, followed by annealing at 175 ºC for 10 min.

Table 3.1. Summary of photovoltaic properties and SCLC carrier mobilities of PBFI-T:PSEHTT and PBFI-S:PSEHTT blends[a]

nm. The J_{sc} calculated from the EQE spectrum of the PBFI-S cell is 3.21 mA/cm^2, which is within 6.4%, in agreement with that measured directly from *J-V* curve.

Among the possible reasons that could account for the large loss in short-circuit current (J_{sc}) and power conversion efficiency in going from PBFI-T acceptor to PBFI-S acceptor, include: (i) inefficient charge photogeneration at the PBFI-S:PSEHTT interface; (ii) poor bulk charge transport and collection in the PBFI-S blend system; and (iii) blend morphology. A simple view of the HOMO/LUMO energy levels of both blends (Figure 3.2c), PBFI-T:PSEHTT and PBFI-S:PSEHTT, suggests that there is identical driving energy for charge separation via either photoinduced electron transfer or photoinduced hole transfer in both blends.[28-30] However, the EQE results (Figure 3.3c) clearly show that there is inefficient dissociation of excitons generated in both PSEHTT and PBFI-S; in fact, light absorption in PBFI-S contributes only a small amount to the photocurrent mainly in the 350-420 nm region. Adapting the empirical expression for the free energy for photoinduced electron transfer (DG_{CT}) in polymer/fullerene systems[28,30] to the present all-polymer systems we have:

$$DG_{CT} = E_{CT} - E_g^{opt} = q\,V_{oc} + 0.47\text{ eV} - E_g^{opt} \qquad (1)$$

where E_{CT} is the charge transfer energy, V_{oc} is the value at room temperature and 1 sun illumination and q is the elementary charge. For the PBFI-T:PSEHTT blend system, with E_{CT} of 1.12 eV and E_g^{opt} of 1.38 eV we have $DG_{CT} = -0.26$ eV. An E_{CT} of 0.98 eV and E_g^{opt} of 1.13 eV results in $DG_{CT} = -0.15$ eV for the PBFI-S:PSEHTT blend system, indicating an almost two-fold increase in free energy for charge transfer compared to the PBFI-T acceptor. We examine below the other possible contributions to the loss of photocurrent and conversion efficiency in these all-polymer solar cells by investigating bulk charge transport and morphology of the active layers.

3.2.3. Bulk Charge Transport

The bulk charge transport properties of PBFI-T:PSEHTT and PBFI-S:PSEHTT blend solar cells were investigated by using the space-charge-limited current (SCLC) measurement. Electron mobility was measured in an ITO/ZnO/active layer/LiF/Al device structure whereas hole mobility was measured in an ITO/PEDOT:PSS/active layer/Au device structure. We found that the bulk hole mobility was 4.8×10^{-5} cm^2/Vs in PBFI-T:PSEHTT blend and 2.7×10^{-5} cm^2/Vs in PBFI-S:PSEHTT blend (Figure 3.4, Table 1), which are quite comparable for both blend systems. In contrast, a large difference was observed in the bulk electron mobility of the two blends. The electron mobility in the PBFI-T:PSEHTT blend (2.2×10^{-6} cm^2/Vs) was nearly two orders of magnitude higher than that in the PBFI-S:PSEHTT blends (4.6×10^{-8} cm^2/Vs) (Figure 3.4, Table 1). The relatively higher and nearly balanced bulk carrier mobilities of PBFI-T:PSEHTT blend compared to the PBFI-S:PSEHTT blend could partly explain the higher photovoltaic performance of PBFI-T:PSEHTT cells. These results suggest that the poorer bulk electron transport in the active layer blend of PBFI-S:PSEHTT solar cells could partly account for the significant loss in photocurrent and power conversion efficiency compared to the corresponding PBFI-T:PSEHTT devices.

3.2.4. Surface and Bulk Morphologies

The surface and bulk morphologies of the all-polymer blend solar cells were investigated respectively by atomic force microscopy (AFM) imaging and grazing incidence wide-angle X-ray scattering (GIWAXS). AFM topographic and phase images taken directly from the surfaces of the active layers are shown in Figure 3.5. Both PBFI-T:PSEHTT and PBFI-S:PSEHTT blends

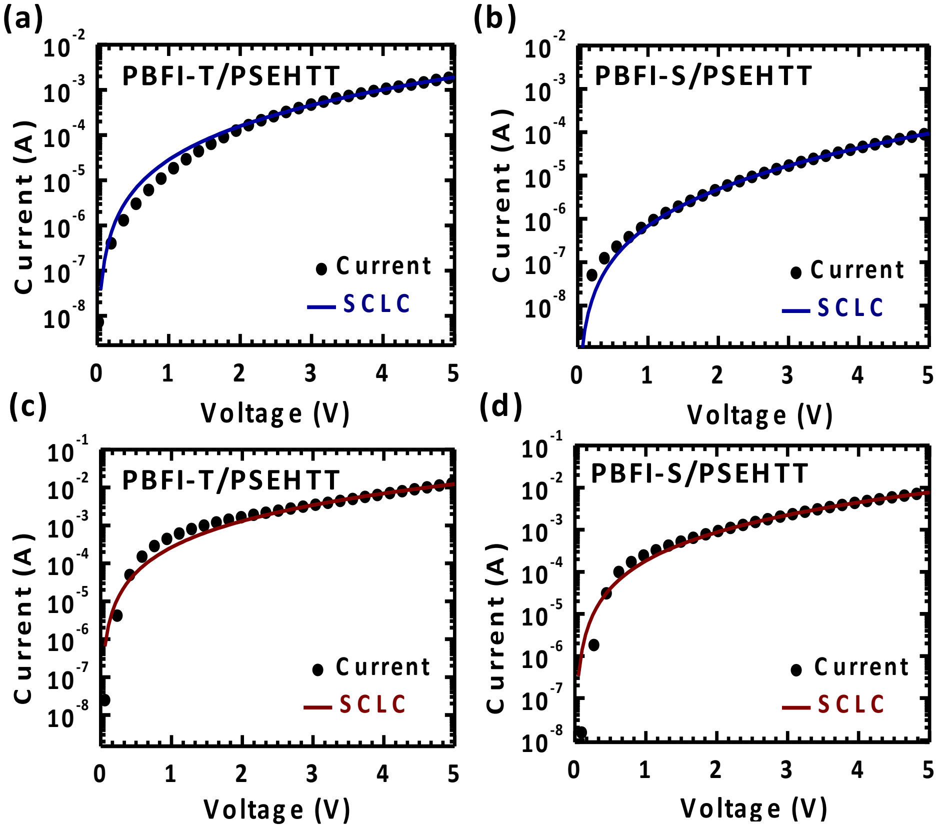

Figure 3.4. Current (J) – voltage (V) characteristics and space charge limited current (SCLC) fittings of devices measured in ambient conditions: Electron-only SCLC devices of ITO/ZnO/blend/LiF/Al (a, b) and hole-only SCLC devices of ITO/PEDOT:PSS/blend/Au (c, d).

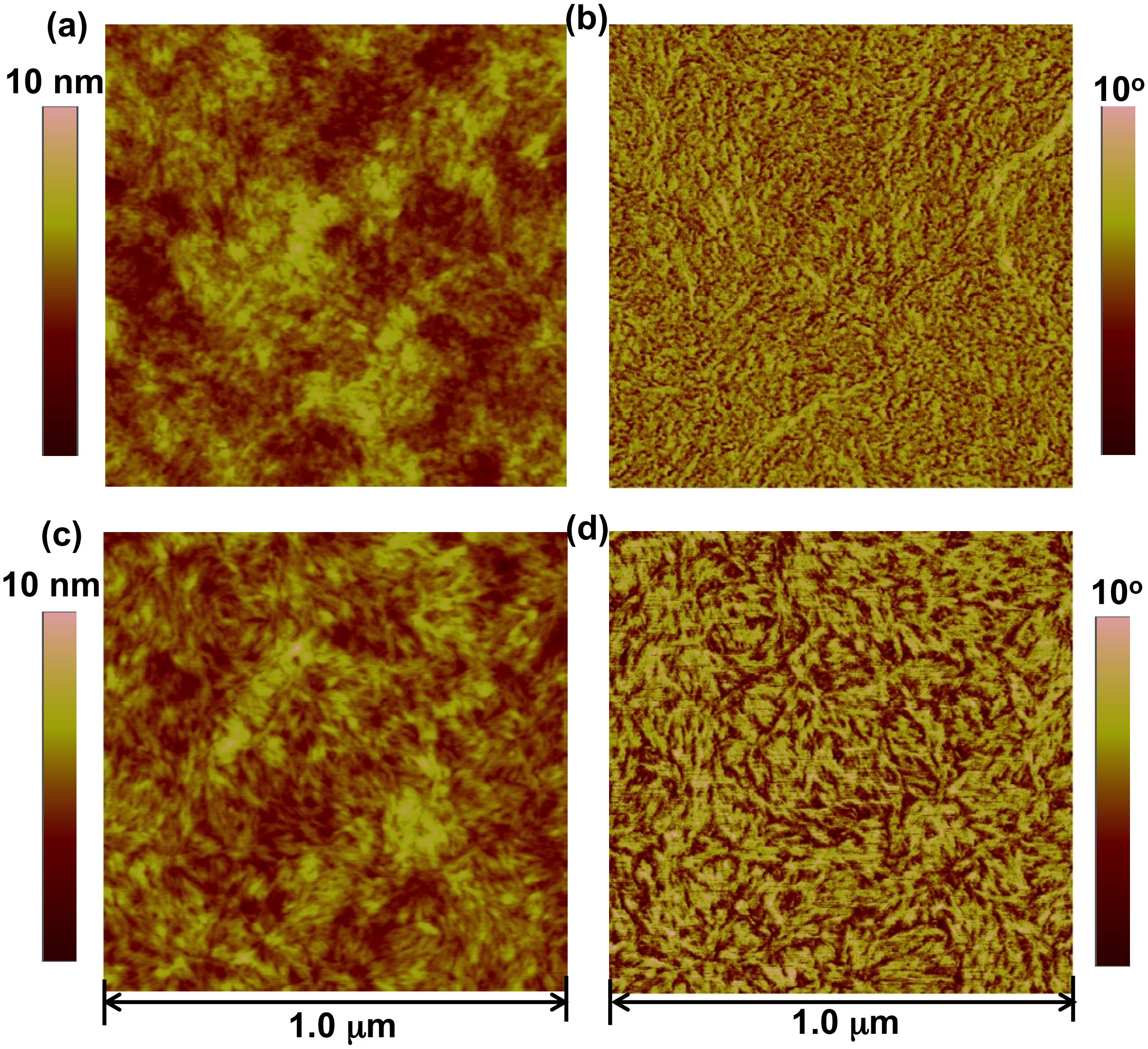

Figure 3.5. AFM topographic (a and c) and phase (b and d) images of the surface of PBFI-T:PSEHTT (a and b) and PBFI-S:PSEHTT (c and d) blend active layers.

formed good quality active layer films with smooth surfaces ($R_g < 1$ nm) as shown in the height images (Figure 3.5a and 5c). The phase images in Figure 3.5b and 5d revealed surface features of interconnected nanoscale networks. The observed phase domains in PBFI-T:PSEHTT blend are finer than those of PBFI-S: PSEHTT blend, suggesting a greater interface area between the donor and the acceptor phases. Although the surface morphology of a polymer/polymer blend film is not necessarily identical to its bulk morphology because of the potential for vertical phase segregation,[44] the observed nanoscale phase separation and a bicontinuous network structure in the AFM images suggest that efficient charge separation could be obtained in both all-polymer blend devices. In other words, the observed similar surface morphology could not explain the observed large difference in photovoltaic properties.

To further address the electronic differences between PBFI-T and PBFI-S, we performed GIWAXS to study bulk film morphology and crystallinity. Fortunately, in blends of different polymers, each component has unique diffraction peaks that can be used to examine each polymer in the blend. Moreover, this technique yields 2D-scattering information that can be used to examine chain orientation by separately integrating the in-plane and out-of-plane components of the diffraction patterns. For this study, the pure PBFI-T and PBFI-S polymers show diffraction patterns typical of semi-crystalline conjugated polymers[128,129] with lamellar (100) and π-π stacking (010) peaks at 0.22 $Å^{-1}$ and 1.5 $Å^{-1}$, respectively (Figure 3.6). There is also a monomer-to-monomer repeat distance (001) peak at around 0.8 $Å^{-1}$. The PBFI-T (100) peak has a higher integrated intensity out-of-plane compared to in-plane, implying an edge-on stacking motif (Figure 3.6a,c). The same general trend is observed for PBFI-S, but the difference in peak areas between out-of-plane and in-plane diffraction is less and the PBFI-S peaks are all broader, indicating smaller crystalline coherence lengths and less edge-on orientation in PBFI-S (Figure 3.7) compared to PBFI-T (Figure 3.6b,d). Interestingly, the (100) peaks for both PBFI-T and PBFI-S show a larger repeat distance in-plane than out-of-plane. For PBFI-T, the in-plane repeat distance is 2.9 Å larger than the out-of-plane value, and for PBFI-S, the difference is 4.1 Å. Because the out-of-plane diffraction is susceptible to artifacts caused by the specular reflection we were integrated in 10^{o} slices to determine if the shifts present between the in and out-of-plane diffraction exists at all angles (Figure 3.8 and 3.9). Typically, the diffraction is obtained by integrating one 10^{o} slice in both the horizontal (xy, in-plane) and vertical (z, out-of-plane) directions; here we analyzed all of the slices that span from the in-plane slice to the out-of-plane slice (9 slices, $0\text{-}90^{o}$). PBFI-T and PBFI-S both show shifts in (100) and (010) peaks towards higher q when integrating from in-plane to out-of-plane. The in-plane (100) and out-of-plane (010) peaks together describe polymer chains with a face-on orientation in these films. We find that the in-plane (100) is shifted to lower q and the out-of-plane (010) is shifted to a higher q. This supports the picture where interactions with the substrate straightens polymer chains and promotes close π-stacking distances while ordering the alkyl chains on this large monomer unit, thereby causing the lamellar stacking distance to increase. By contrast, polymers with an edge-on stacking motif are described by the out-of-plane (100) peak and the in-plane (010) peak. When this large monomer unit assembles edge-on, the alkyl chains are no longer aligned resulting in a decrease of the lamellar stacking distance and an increase in the π-stacking distance. Similar effects are observed in the PBFI-S:PSEHTT and PBFI-T:PSEHTT BHJs, where the PBFI polymer peaks and the (100) of PSEHTT shifts but the rest of the PSEHTT peaks ultimately remain unaffected. These findings indicate that the interactions with the substrate can have a significant effect on the lamellar stacking in these polymers with large monomer units and thus shifts between the in and out-of-plane diffraction are observed.

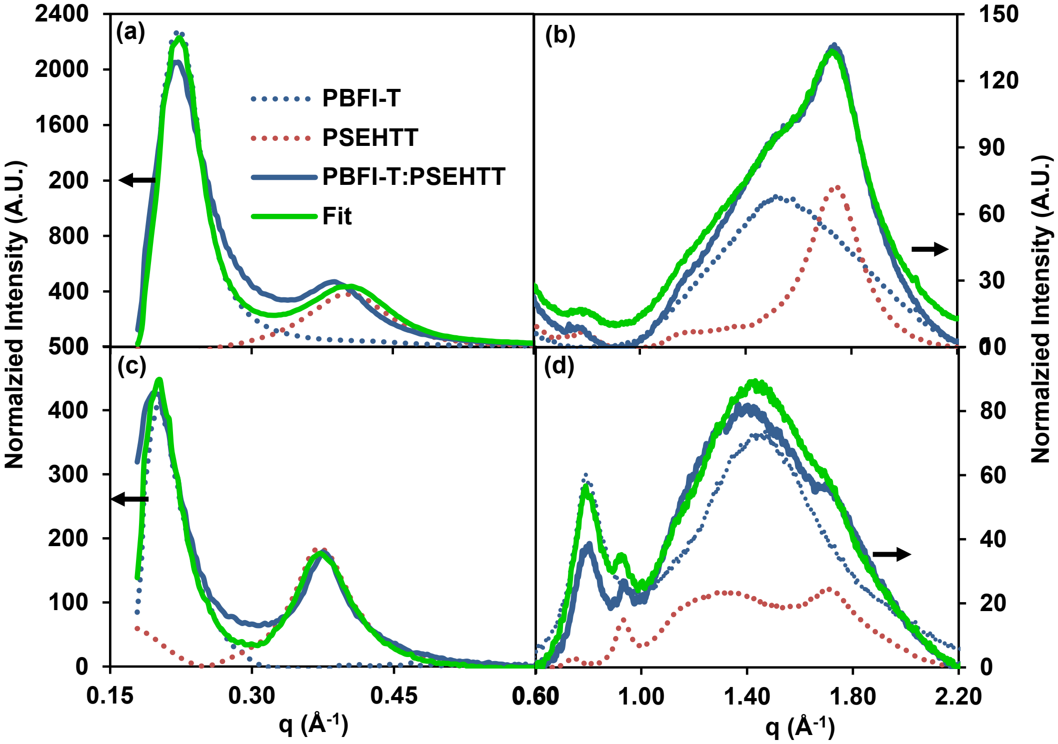

Figure 3.6. GIWAXS radially averaged scattering patterns for PBFI-T, PSEHTT and the PBFI-T:PSEHTT blend as well as the linear regression of the blend: (a) and (b) out-of-plane scattering (c) and (d) in-plane scattering.

The PSEHTT shows similar diffraction, but with the lamellar diffraction peak shifted to higher *q* because of the smaller size of the monomer unit in PSEHTT (Figure 3.6). For PSEHTT, peaks are observed at 0.38 $Å^{-1}$ for the (100) diffraction peak, and at 1.3 $Å^{-1}$ and 1.7 $Å^{-1}$ for the (010) diffraction peaks (Figure 3.6). The two peaks likely correspond to highly ordered lamellar stacking and more disordered π-stacking domains. Again, we observe the (001) distance peak at around 0.8 $Å^{-1}$. For PSEHTT, the highly ordered π-stacking peak shows distinctively greater out-of-plane scattering intensity, suggesting a face-on orientation of these domains. The less ordered π-π stacking peaks show slightly higher in-plane intensity, suggesting that these domains are either edge on or isotropic. Potentially, interactions between the polymer and the substrate help planarize polymer chains near the substrate interface, producing a smaller π-π stacking distance and a distinct face-on orientation. In the bulk of the film, π-π stacking distances would then be greater and the domain orientation more isotropic. Other than the changes in intensity for the two (010) peaks, no additional peak shifts are observed between in-plane and out-of-plane diffractions for PSEHTT, in contrast to the results presented above for the neat PBFI-T and PBFI-S.

To a first approximation, diffraction from PBFI-T:PSEHTT (Figure 3.6) and PBFI-S:PSEHTT (Figure 3.7) blend films appear to be a linear combination of the pure polymers. The first conclusion from the diffraction data is that both PBFI-T:PSEHTT and PBFI-S:PSEHTT films are dominantly separated into mostly pure component domains. To gain more insight, the blend data was fit as a linear combination of the two pure polymers for both in-plane and out-of-plane diffraction. Figures 6 and 7 show the pure polymers, the polymer blends, and the best fit sum for both PBFI-T:PSEHTT and PBFI-S:PSEHTT blends, respectively. By comparing the out-of-plane integrated data of the polymer blend films against the linear regression fit of PBFI-

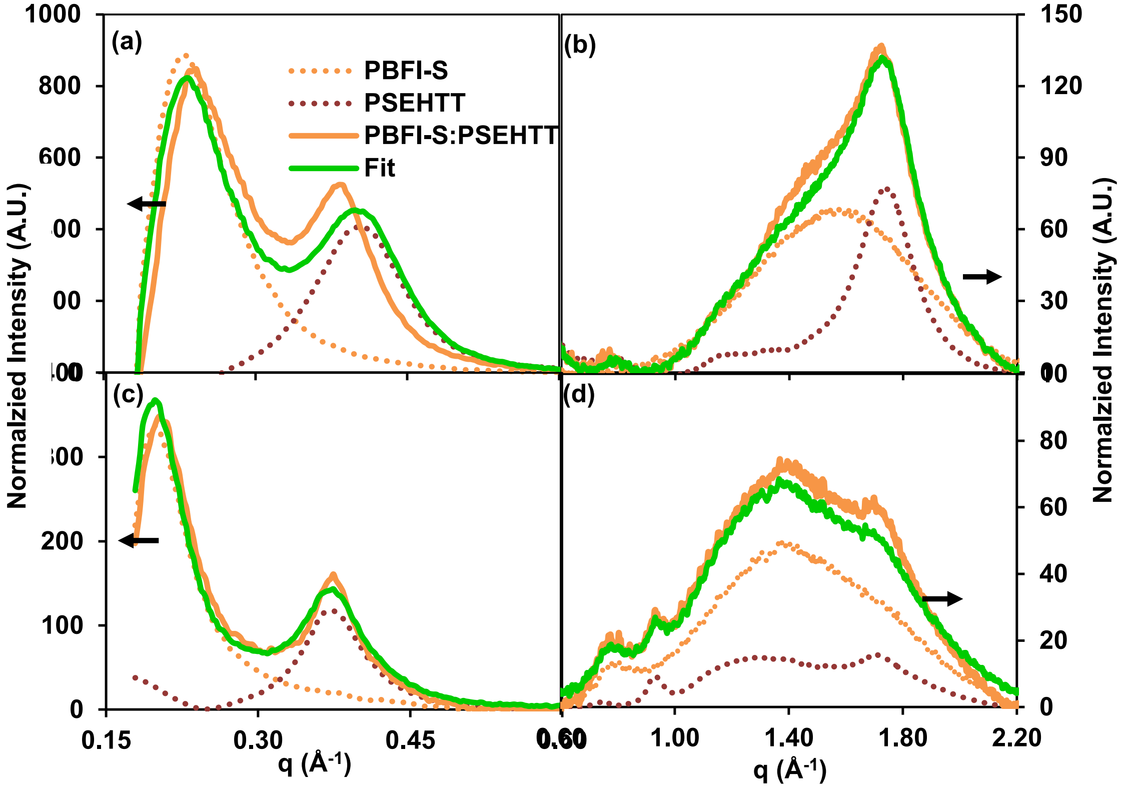

Figure 3.7. GIWAXS radially averaged scattering patterns of PBFI-S, PSEHTT and the PBFI-S:PSEHTT blend as well as the linear regression of the blend: (a) and (b) out-of-plane scattering (c) and (d) in-plane scattering.

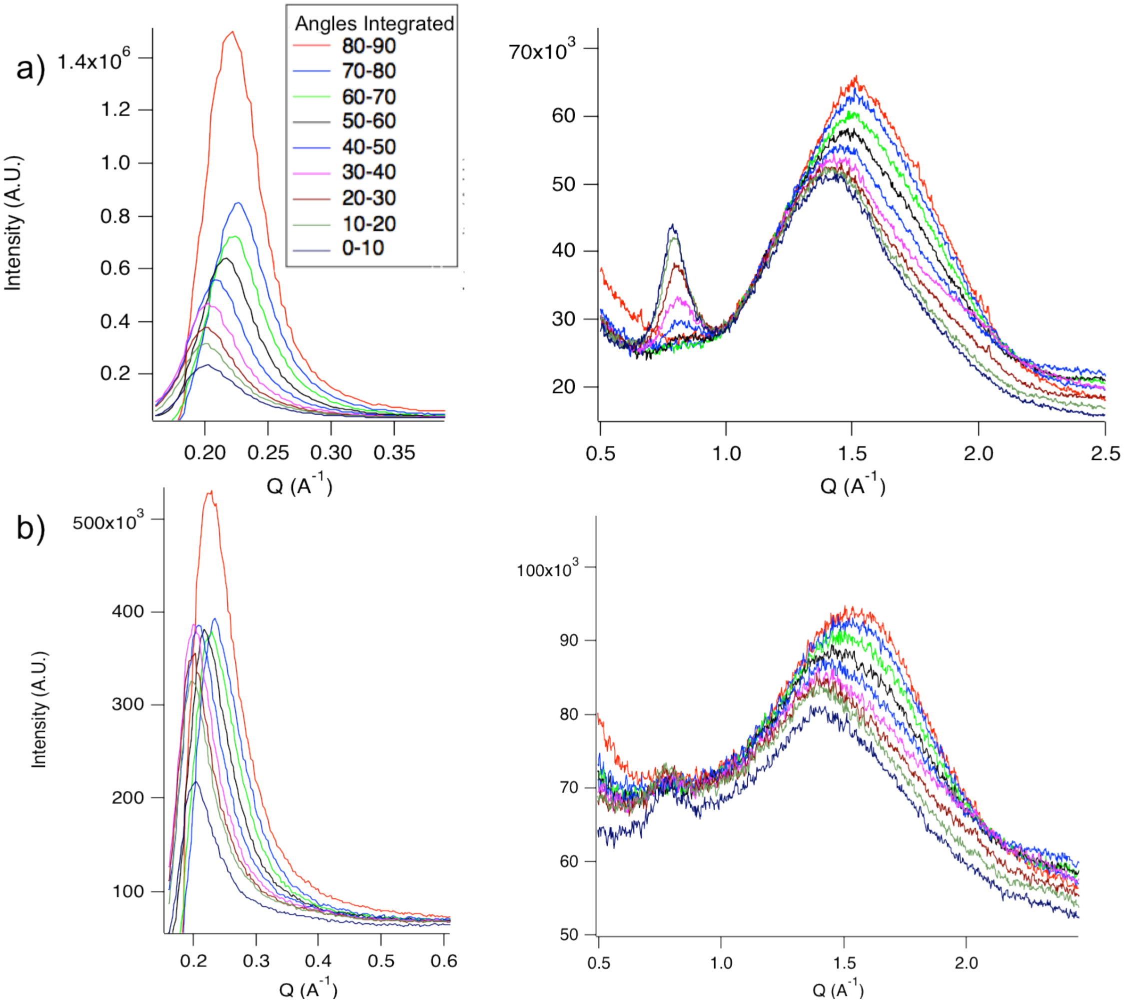

Figure 3.8. X-ray diffraction patterns as a function of diffractometer angle chi. Pure PBFI-T (a) and pure PBFI-S (b) integrations of 2D diffraction pattern in 10° slices from 0-90°. The 0-10° integration corresponds to the in-plane diffraction and the 80-90° integration is the out-of-plane diffraction. The shift between in and out-of-plane is significant for both the (100) and (010) peaks. Because a gradual peak shift is observed going from in- to out-of-plane diffraction, this shift is likely indicative of a real change in lattice constant caused by packing differences between edge-on and face-on oriented polymer chains. It is unlikely to be caused by interference from specular reflectance, which should only affect angle near 90°.

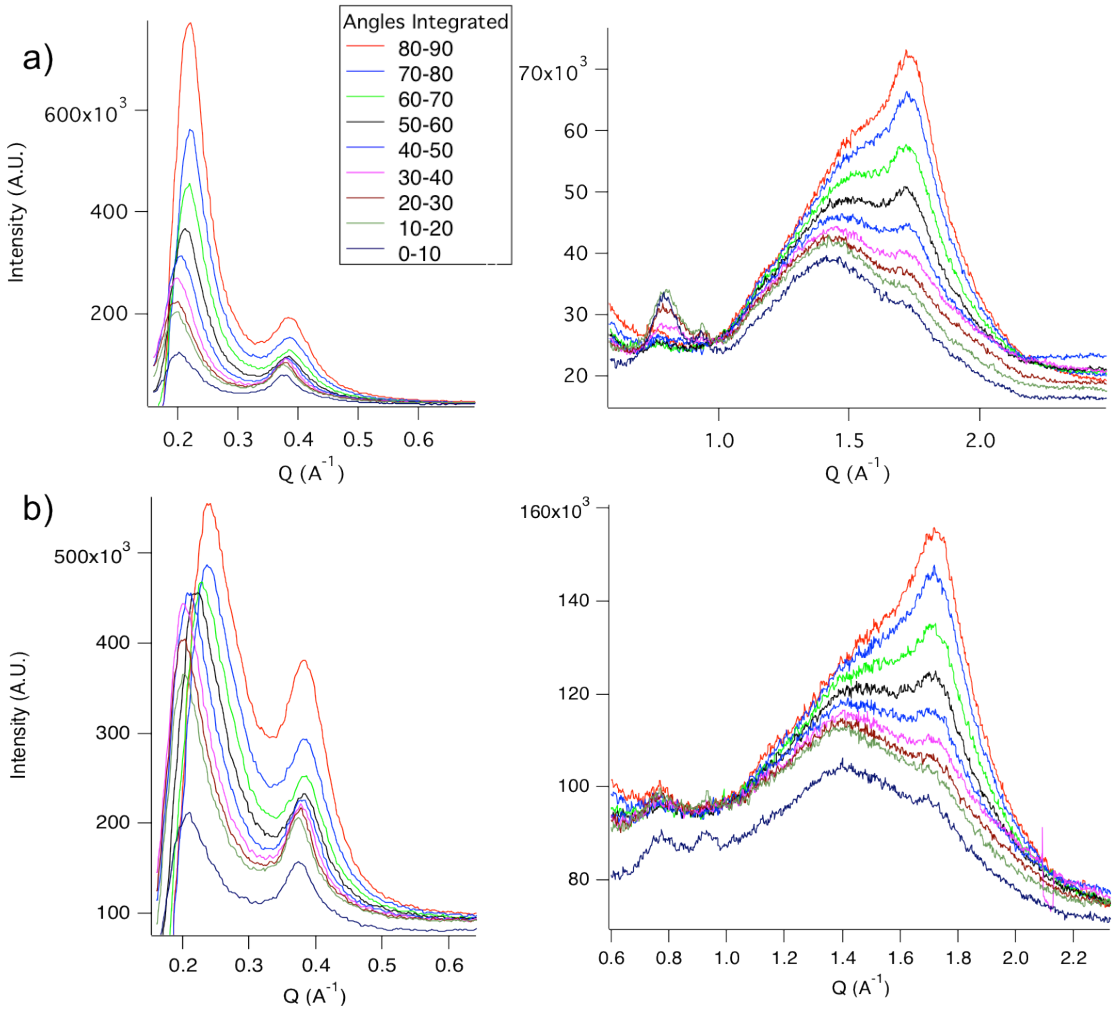

Figure 3.9. a) X-ray diffraction patterns as a function of diffractometer angle chi. PSEHTT:PBFI-T BHJ blend (a) and PSEHTT:PBFI-S blend (b) integrations of 2D diffraction pattern in 10° slices from 0-90°. The 0-10° integration corresponds to the in-plane diffraction and the 80-90° integration is the out-of-plane diffraction. Significant shifts are again observed for the PBFI-T and PBFI-S peaks, but the PSEHTT peaks show almost no shifts, indicating less conformational freedom for the PSEHTT.

T:PSEHTT, we observe a peak shift of 0.7 Å in the PSEHTT peak in Figure 3.6a. This indicates some mixing of PBFI-T into the pure PSEHTT domains, which results in an increase in the lamellar stacking distance of PSEHTT. In contrast, the out-of-plane PBFI-T (100) peak does not shift, implying no mixing of the PSEHTT molecules into the pure PBFI-T domains. Interestingly, the in-plane data shows minimal shifts for both PBFI-T and PSEHTT data when compared to the linear regression fit, as shown in Figure 3.6b, indicating less mixing for PSEHTT domains oriented face-on with respect to the substrate. There are no shifts in the π-π stacking peaks for either PBFI-T or PSEHTT in any orientation and the data are well fit by a linear combination of the pure polymers, indicating that polymer mixing does not disrupt the π-π interactions. We note that the combined data was fit simply by scaling and adding the pure polymer patterns and a single scaling parameter produced good agreement with the experimental data across both low- and high-*q* regions, giving us confidence in this method.

In contrast to the PBFI-T blends, Figure 3.7a shows that for blends of PBFI-S with PSEHTT, the out-of-plane (100) peak for PSEHTT shifts to a larger lamellar spacing by 0.7 Å and PBFI-S shifts to a smaller lamellar spacing by 0.8 Å, indicating mixing of the two polymers. For mixtures of two polymers, the lamellar spacing is generally an average of the two, with the lamellar spacing for the larger spacing polymer shifting to higher *q* and the lamellar spacing for the smaller polymer shifting to lower *q*. This happens because a polymer with a shorter lamellar spacing allows for disordering of the polymer side chains in the polymer with the longer lamellar spacing and a decrease in the average lamellar spacing.[130,131] Overall, these shifts indicate that for edge-on domains, PBFI-S can mix into PSEHTT domains and PSEHTT molecules can mix into PBFI-S domains. The in-plane diffraction for PBFI-S:PSEHTT blend film shows minimal shifts in Figure 3.7c-d compared to the shifts observed in the out-of-plane direction, again suggesting that face-on domains show less mixing than edge-on domains. In addition, the π-π stacking peaks again appear to be a linear combination of PSEHTT and PBFI-S and do not shift.

Comparing these GIWAXS findings to device performance suggest that the presence of relatively pure PBFI-T domains is important to device performance, because the PBFI-T blends show significantly higher efficiency than the PBFI-S blends. Some mixing of acceptor polymer molecules into the PSEHTT domains occurs in both systems, and it is possible that device performance could be further improved if this mixing could be reduced.

3.3. Conclusions

The tetraazabenzodifluoranthene diimide-based n-type semiconducting polymers, PBFI-T and PBFI-S, have been investigated as new electron acceptors in polymer/polymer (all-polymer) blend solar cells. All-polymer blend solar cells using the thiophene-linked acceptor polymer (PBFI-T) with PSEHTT donor had a PCE of 2.60% with a J_{sc} of 7.34 mA/cm^2, V_{oc} of 0.67 V, and 52% FF. Although the selenophene-linked acceptor polymer (PBFI-S) has a much smaller optical band gap (1.13 eV) than the thiophene-linked acceptor polymer (PBFI-T), PBFI-S:PSEHTT blend solar cells had a much reduced performance (0.75% PCE, V_{oc} = 0.61 V, and FF = 43%), showing that light harvesting by PBFI-S did not contribute significantly to photocurrent generation. Among the factors that explain the large reduction in photovoltaic efficiency of PBFI-S:PSEHTT blends compared to PBFI-T:PSEHTT blends are: the reduced driving energy for charge separation (DG_{CT}) and reduced electron mobility in the former blend system; and the differences in miscibility of the polymers in the two blend systems as observed in GIWAXS experiments.

3.4. Experimental

3.4.1. Materials

Tris(o-tolyl)phosphine and bis(dibenzylideneacetone)palladium (0) (Pd(dba)2) were purchased from Aldrich. 8,17-Dibromobenzodifluoranthene-3,4,12,13-tetracaboxylic acid diimide (BFI-Br2)[39], 2,5-bistrimethylstannylselenophene[12] and poly[(7,9,16,18-tetraazabenzodifluoranthene-3,4,12,13-tetracarboxylic acid diimide)-8,17-diyl-alt-thiophene-2,5-diyl] (PBFI-T)[40] were synthesized by following the reported procedures. The synthesis of poly[(4,4'-bis(2-ethylhexyl)dithieno[3,2-b:2',3'-d]silole)-2,6-diyl-alt-(2,5-bis(3-(2-ethylhexyl)thiophen-2yl)thiazolo[5,4-d]thiazole)] (PSEHTT) was previously reported.

3.4.2. Synthesis of PBFI-S

BFI-Br2 (200 mg, 0.14 mmol) and 2,5-bis(trimethylstannyl)selenophene (65 mg, 0.14 mmol) were dissolved in 20 mL of anhydrous toluene and purged with Ar for 10 min. A solution of Pd(dba)$_2$ (6 mg) and Tris(o-tolyl)phosphine (12 mg) was added to the monomer solution. The mixture was slowly heated to reflux and kept stirring for 5 days. At the end of the polymerization, 2-tributylstannylthiophene (0.1 mL) with a solution of Pd(dba)$_2$ (3 mg) and P(o-tol)$_3$ (6 mg) and bromobenzene (0.15 mL) were successively added to the mixture to remove the remaining end (functional) groups. Each ending-capping reaction took 12 hr. After cooling back to room temperature, the volatile materials were evaporated and the solids were re-dissolved in 6 mL of toluene and precipitated into a mixture of 100 mL of methanol and concentrated HCl (20:1, *v*/*v*). The green solid was collected and further purified by successive Soxhlet extraction with methanol, acetone and hexanes. Yield (126 mg, 64.4%). GPC (at 60 °C in chlorobenzene against polystyrene standards): M_w = 104 kDa, Mn =29.2 kDa, PDI (M_w/M_n) = 3.55. 1H NMR

($CDCl_3$, 25 °C, 500 MHz): δ = 10.5-7.4 (br, 10H, aromatic-H), 4.6-3.7 (br, 4H, CH_2), 2.4-0 ppm (m, 94H). UV/Vis/NIR: l_{max} (in $CHCl_3$, 5.2 mM) 894 nm ($\varepsilon = 3.1\times10^3$ $M^{-1}cm^{-1}$), 378 nm (2.0×10^4 $M^{-1}cm^{-1}$); l_{max} (thin film) 948 nm (1.7×10^4 cm-1), 377 nm (7.3×10^4 cm^{-1}). CV (thin film, in 0.1 M of Bu_4NPF_6 in CH_3CN): $E_{1/2}$(red) −1.06 V (irreversible), E_{peak}(ox) 1.23 V (irreversible). TGA (N_2, 10 ºC/min): Td = 428 ºC (onset), 55.7% residue at 800 ºC. Elemental analysis calcd for $C_{86}H_{108}N_6O_4Se$: C 75.46%, H 7.95%, N 6.14%; found C 74.79%, H 7.84%, N 5.99%.

3.4.3. Characterizations

Gel permeation chromatography (GPC) analysis was performed using Polymer Lab Model 120 gel permeation chromatograph (DRI/high sensitivity refractive index detector and PL-BV400HT viscometer) against polystyrene standards in chlorobenzene at 60 ° C. Thermogravimetric analysis (TGA) of the polymers was conducted on a TA Instrument model Q50TGA at a heating rate of 10 ˚C/min under a flow of N_2 with scans from room temperature to 800 ˚C. Differential scanning calorimetry (DSC) analysis was performed on a TA Instruments Q100 under N2 by scanning from 20 ˚C to 400 ˚C at a heating rate of 20 ˚C/min. Cyclic voltammetry was performed on an EG&G Princeton Applied Research potentiostat/galvanostat (model 273A). The CV data were analyzed by using a Model 270 Electrochemical Analysis System Software on a PC computer. A three-electrode cell was used, using platinum wire electrodes as both counter and working electrodes. A thin film of the polymer sample was drop casted onto the working electrode from a solution of polymer in chloroform (10 mg/mL) and dried under vacuum. Silver/silver ion (Ag in 0.1 M $AgNO_3$ solution, Bioanalytical System, Inc.) was used as a reference electrode. Ferrocene was used as an internal standard with ferrocene/ferrocenium (Fc/Fc^+) couple at 0.16 V vs SCE. All solutions were purged with argon for 20 min before each experiment. Optical absorption spectra were collected on a Perkin-Elmer model Lambda 900 UV/vis/near-IR spectrophotometer.

3.4.4. Fabrication and characterization of inverted solar cells

Solutions of 20 mg/mL PSEHTT and 20 mg/mL PBFI-T in chlorobenzene were prepared separately. Then a PSEHTT:PBFI-T blend solution was prepared by mixing the two polymer solutions at a volume ratio of 1:2, followed by adding chlorobenzene to obtain a total concentration of 15 mg/mL. the PSEHTT:PBFI-S blend solution was similarly prepared. Solar cells with the inverted device structure of ITO/ZnO/active layer/MoO_3/Ag were fabricated. ITO substrates (10 Ω/□, Shanghai B. Tree Tech. Consult Co., Ltd, Shanghai, China) were cleaned sequentially with acetone, deionized water and isopropyl alcohol in an ultrasonic bath, and blown with nitrogen until dried, followed by oxygen plasma treatment. Zinc oxide (ZnO) precursor was prepared as reported in the literature,[47] spin-coated on top of the ITO and annealed at 250 ° C for 1 hr in air. The ZnO film thickness was approximately 30 nm. The active layer was then spin-coated from the PSEHTT:PBFI-X (X = T or S) blend solution to make a thin film of ~60-80 nm thickness and thermally annealed at 175 ° C for 10 min in a glovebox. The substrates were then loaded into a thermal evaporator (BOC Edwards, 306) to deposit an anode composed of thin layer of 10.0 nm MoO_3 and 100 nm Ag under high vacuum (8×10^{-7} Torr). Five solar cells, each with an active area of 4 mm^2, were fabricated per ITO substrate. The current density–voltage (*J*–*V*) curves of solar cells were measured using a HP4155A semiconductor parameter analyzer under laboratory ambient air conditions. An AM1.5 illumination at 100 mW/cm^2 was provided by a filtered Xe lamp and calibrated by using an NREL-calibrated Si photodiode. The external quantum efficiency (EQE) was measured by using a QEX10 solar cell quantum efficiency measurement system (PV Measurements, Inc.) and was calibrated with an NREL-certified Si photodiode before measurement.

3.4.5. Space Charge Limited Current (SCLC) Measurement

Current-voltage (J-V) characteristics of the SCLC devices were measured by using a HP4155A semiconductor parameter analyzer (Yokogawa Hewlett-Packard, Tokyo). The carrier mobility was extracted by fitting the J-V curves in the near quadratic region according to the modified Mott-Gurney equation,

$$J = \frac{9}{8}\varepsilon\varepsilon_0\mu\frac{V^2}{L^3}\exp\left(0.89\beta\frac{\sqrt{V}}{\sqrt{L}}\right)$$

where J is the current density, ε_0 is the permittivity of free space, ε is the relative permittivity, μ is the zero-field mobility, V is the applied voltage, L is the thickness of active layer, and β is the field-activation factor.

3.4.6. Grazing incidence X-ray Scattering (GIWAXS)

2D grazing incidence wide-angle X-ray diffraction (GIWAXS) experiments were performed at the Stanford Synchrotron Radiation Lightsource (SSRL) on beamline 11-3 using a wavelength of 0.9742 Å. The beamspot was approximately 150 μm wide and a helium chamber was utilized to reduce signal-to-noise. Samples were prepared by spinning films onto silicon substrates. The data was analyzed using the WxDiff software package.

CHAPTER 4

Understanding Local and Macroscopic Electron Mobilities in the Fullerene Network of Conjugated Polymer-based Solar Cells: Time-Resolved Microwave Conductivity and Theory

4.1. Introduction

There are a number of factors that can limit the power conversion efficiency (PCE) of organic photovoltaics, including the efficiency of exciton generation and separation,[12,132–134] the mobilities of the subsequently generated electrons and holes,[135–137] and the nanometer-scale morphology of the bulk heterojunction (BHJ) network that determines how easily carriers can reach the electrodes or recombine.[138–143] The importance of the network morphology can be seen in the fact that a number of organic electron donors and acceptors with seemingly optimally matched energy levels produce poorly performing solar cells because they have an improper degree of phase segregation when blended together.[144,145] Because of this, there has been a great deal of effort to use processing conditions to control BHJ morphology, including the use of solvent additives,[27–29] post-fabrication thermal annealing,[21,146,147] and sequential deposition of the donor and acceptor layers.[43,52,55,56,61,148,149] All of these techniques greatly increase the parameter space for optimizing power conversion efficiency, which is detrimental when most of the progress in increasing PCE for a given set of materials is made via exploring this parameter space through trial-and-error.

In previous work, we developed a method to control the nanometer-scale morphology of the BHJ network in polymer/fullerene photovoltaics using pentaaryl-substituted fullerenes that self-assemble into one-dimensional stacks.[150–152] The idea is that pentaaryl substitution creates fullerene molecules with a self-complementary shape that promotes stacking; because of their shape, we (and others[153,154]) have referred to this class of fullerene derivatives as ’shuttlecocks’ (SCs). When exploring the behavior of SCs in photovoltaic blends with poly(3-hexylthiophene) (P3HT), we found that the SCs that formed 1-dimensional stacks had significantly improved photovoltaic performance compared with nearly identical fullerenes that had *meta* substitution on the SC ‘feathers’ that inhibited the ability to stack.[150] Subsequently, we worked to control the propensity for stacking by varying the size of alkyl substituents in the *para* position of the SC feathers. We found using X-ray diffraction and atomic force microscopy that varying the functionalization of the pentaaryl feather substituents by a single methyl group lead to dramatic differences in nanoscale morphology in blends with P3HT.[151] This is because SCs with shorter alkyl feather substituents tend to stack less easily than those with longer substituents[152]; non-stacking SCs prefer to phase separate from the donor polymer, whereas the more self-assembling fullerene derivatives preserve the desired blended nanoscale architecture.[151] As a result, the PCE of devices based on fullerene selfassembly was improved due both to enhanced charge separation and an increase in electron mobility throughout the assembled fullerene network.[150]

Even though we were able to demonstrate that self-assembly produces a fullerene network that leads to improved photovoltaic performance, the power conversion efficiency of devices based on SCs fell well short of those utilizing the well-studied [6,6]-phenyl-C_{60}-butyric acid methyl ester (PCBM) fullerene derivative as the electron acceptor. Since PCBM does not self assemble into one-dimensional stacks, the fact that PCBM devices perform better than SC-based devices indicates that network formation is not the only factor contributing to electron mobility in a BHJ device. This suggests that there are (at least) two length scales over which electron mobility is determined in the fullerene network: the macroscopic length scale (i.e., the active layer thickness) over which the electrons must move to be extracted from the device, and a shorter-ranged molecular length scale over which the probability for an electron to hop from one fullerene molecule to the adjacent one is determined. Although a high local electron mobility does not guarantee high macroscopic mobility (since macroscopic mobility can be limited by grain boundaries, the fractal nature of the network etc.), poor local mobility clearly limits the macroscopic performance of a device. It is therefore plausible that molecules like PCBM have local electron mobilities that are so high compared to those of SC derivatives that SC-based devices do not perform as well PCBM-based devices, even though SCs form a better macroscopic network.

Although there are many methods for measuring the macroscopic mobility of the carriers in organic photovoltaics, it is less clear how to measure the role that local mobility plays in device performance. Thus, in this paper we aim to ascertain how device-wide network formation and local molecular arrangements collectively determine electron extraction from polymer/ fullerene solar cells. We start by developing a density functional theory (DFT)-based computational technique to examine the electronic coupling between adjacent fullerene molecules, providing a theoretical estimate of the 'local' electron mobility. To verify that our calculation protocol makes physical sense, we then turn to time-resolved microwave conductivity (TRMC) experiments that directly measure local conductivities in P3HT/ fullerene blend films. We find that the experimentally-measured TRMC local mobilities correlate well with the theoretical predictions. Taken together, the two techniques are able to explain general features of organic photovoltaic device performance, including why PCBM is the acceptor of choice for most polymer-based solar cells even though it does not form the best macroscopic network. The fact that the theoretical predictions are validated by experiment also indicates that we can use such calculations to determine ‘design rules’ for new fullerene acceptors that could potentially outperform PCBM. And perhaps more importantly, the fact that most fullerene acceptors (including PCBM) do not form networks that simultaneously optimize both the local and macroscopic electron mobilities indicates that there is still significant room for improvement in the fullerene component of polymer/fullerene solar cells.

4.2. Results and Discussion

4.2.1. Electronic Coupling Determined through Density Function Theory Calculations

In polymer/fullerene solar cells, electron mobility at the local level consists of charge transfer between neighboring fullerene acceptors. To understand how the local rate of electron transfer varies between different fullerene derivatives, we developed a DFT-based protocol to calculate the electronic coupling between pairs of fullerene molecules in a variety of geometries. The electron transfer problem we consider consists of moving charge between two fullerene molecules, which we label left (L) and right (R):

$$L- + R \rightarrow L + R- \qquad (1)$$

The fundamental quantity of interest is the electronic coupling γ between the L and R molecules, which has the form:[155,156]

$$\gamma(L \rightarrow R) = |\langle \Psi_L | H | \Psi_R \rangle| \qquad (2)$$

where H is the total Hamiltonian and Ψ_i is the localized wavefunction of the transferred electron on molecule i (i.e., the LUMO of the neutral molecule). In our case, the Hamiltonian and wavefunctions are calculated with DFT, which has been shown to give good accuracy within the

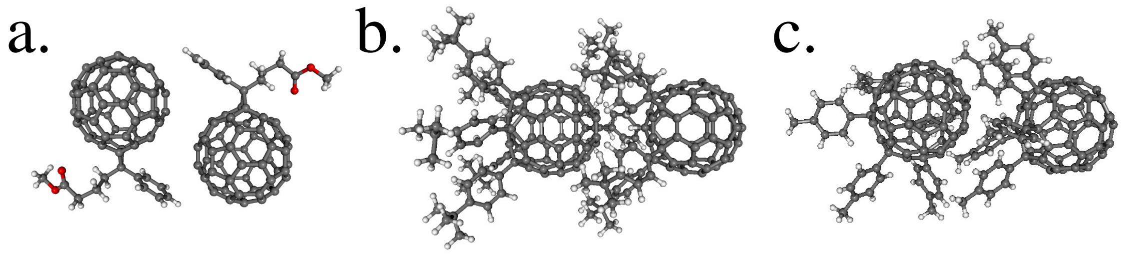

PCBM TBP (native stack) TOL (zigzag stack)

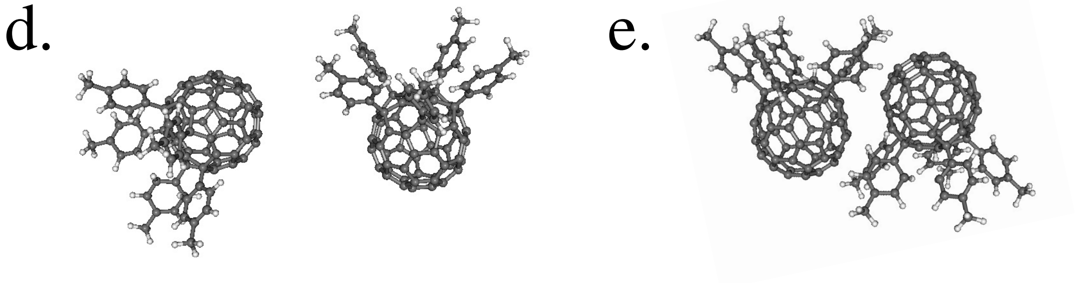

TOL (interstack) TOL (inverted)

Figure 4.1. Chemical structures of the fullerene derivatives considered in this work and the geometries of the fullerene pairs used in our DFT calculations. a) PCBM, taken from the crystal structure in Ref. [157]; b) the 4-*t*Bu shuttlecock molecule in its stacked orientation; c) the 4-Me shuttlecock in its native crystal structure: note the 4-Me molecules crystallize in a ’zigzag stack’ motif rather than the linear ’ball-in-cup’ exhibited by 4- *t*Bu; d) the 4-Me molecule in its interstack geometry over which we varied the separation distance of the individual molecules; e) 4-Me molecules in a head-to-tail (’inverted stack’) geometry similar to that of PCBM molecules. The red color in PCBM denotes oxygen atoms; none of the other molecules contain any hetero-atoms.

Molecule	Center-to-Center Distance [Å]	Coupling [eV]
4- *t* Bu (native stack)	10.8	2.95×10^{-4}
4-Me (zigzag stack)	10.9	2.64×10^{-4}
4-Me (interstack)	11.2–15.2	$1.75 \times 10^{-7} - 4.15 \times 10^{-4}$
4-Me (inverted)	9.9	1.45×10^{-3}
PCBM	10.2	1.00×10^{-2}

Table 4.1. Calculated electron couplings for fullerene molecular dimers with the geometries shown in Figure 1. Couplings were calculated using DFT-based methods.

Marcus theory framework,[157–160] using the B3LYP functional and STO-3G basis set. Direct calculation of γ, however, can be problematic. This is because if the effects of the environment are ignored, the electron can be artificially localized on an individual molecule due to asymmetry in the system. To overcome this problem, when calculating γ we apply an electric field to delocalize the excited states across the two-molecule system. This is because in a real BHJ system, each fullerene molecule sees, on average, an identical chemical environment; our application of an external field in effect 'equilibrates' the system and allows the electron to delocalize between the two molecules the way it would in the bulk system. This means that with the application of the field, the LUMO and LUMO+1 orbitals are not localized on the same molecule, so we can easily calculate γ from the energy splitting between these two orbitals. More specifically, in a two-level system, the coupling between the two levels is equal to the half-splitting of the levels in the diagonal basis. Therefore, we rotated the two-level Hamiltonian into the diabatic basis, and found the coupling simply from the off-diagonal elements.

To tie in with our previous work on self-assembling fullerenes, we started by examining the coupling between two SC molecules, 6,9,12,15,18-pentakis(4-*tert*-butylphenyl)-1-hydro[60] fullerene (4-*t*Bu) and 6,9,12,15,18-pentakis(4-methylphenyl)1-hydro[60]fullerene (4-Me). We chose these two SC fullerenes because they present a sharp contrast in their ability to self-assemble. Previously, we found that 4-*t*Bu was a 'universal stacker', assembling into one-dimensional stacks when crystallized from essentially every solvent we explored,[152] which in turn lead to the best solar cell performance of all the SC fullerenes we examined.[151] In contrast, the 4-Me molecule, which is electronically identical to 4-*t*Bu, appeared to show little propensity for columnar self-assembly,[152] which resulted in poor device performance.[151] Finally, to understand how local mobility among the fullerenes influences overall device performance, we also elected to examine coupling between molecules of the well-studied PCBM. The chemical structures of the 4-*t*Bu, 4-Me and PCBM fullerene derivatives, as well as the geometries we used for calculating the electronic coupling between pairs of these molecules, are shown in Figure 4.1.

Although we do not know the distribution of geometries of pairs of fullerene molecules in a working BHJ device, it seems reasonable that on molecular length scales, the spatial relationship between adjacent fullerene molecules should be similar to that in single crystals. Thus, we chose geometries for our calculations for the 4-Me and 4-*t*Bu derivatives from the crystal structures found in our previous work.[152] For the electronic coupling in 4-*t*Bu dimers, we considered only the linearly stacked orientation found in the crystals derived from most different organic solvents (Figure 4.1b). For pairs of 4-Me molecules, we calculated the electronic coupling in a ’zigzag stack’ geometry taken from crystals formed in toluene (Figure 4.1c) and a head-to-tail ’inverted’ geometry taken from crystals formed in methanol (Figure 4.1*e*). For completeness, we also calculated the coupling between 4-Me dimers at their ‘interstack’ geometry (Figure 4.1d). In the native crystal, the interstack 4-Me orientation contains interstitial solvent molecules, which prevent the 4-Me molecules from residing close together. Since there likely is not any solvent present between fullerene molecules in a BHJ device, to calculate the electron transfer probability between 4-Me molecules in this orientation, we eliminated the solvent from the crystal structure and repeated the calculation over intermolecular distances ranging from 11.2 Å to 15.2 Å center-to-center fullerene separation (the lower end of this range is limited by van der Waals contact between the 4-Me molecules, while the upper end is what is found in the native crystal with interstitial solvent molecules). Finally, for the electronic coupling between PCBM molecules (Figure 4.1a), we took the geometry from the PCBM crystal structure in Reference [157]. Using these geometries and our DFT-based method, we calculated the electronic coupling between multiple pairs of fullerene molecules and obtained the results summarized in Table 4.1. For the SC fullerene derivatives, we find that both the 4-Me and 4-*t*Bu molecular pairs have essentially the same electronic coupling (within 10%) when placed in their respective ‘stacking’ orientations; this result makes sense given that 4-Me and 4-*t*Bu have an identical electronic structure, so the overlap of their LUMOs is about the same when adjacent molecules are forced to have similar geometries. When the SC molecules are not in the desired stacked geometry, the electronic coupling varied strongly (roughly exponentially) with the average distance between the fullerene balls. At the closest possible non-stacked distance (limited by steric hindrance of the alkyl substituents), the coupling is actually slightly higher than that in the stacked geometry. Thus, even though we do not know the precise geometry between neighboring SC fullerene molecules in BHJ devices, we can conclude that as long as these molecules stay in close van der Waals contact, the electronic coupling of the pentaaryl fullerenes is comparable in any geometry, lying in the range of 10^{-4} to low 10^{-3} eV.

The fact that the molecular length-scale coupling between pentaaryl fullerenes is similar in nearly every geometry has important implications for solar cells built from these materials. Since the local coupling of these molecules is the same because the molecules have identical electronic structure (i.e., identical HOMO and LUMO levels with similar orbitals), the large differences in device performance we observed for these two molecules[151] must be the result of differences in the macroscopic geometry of the fullerene network. This makes sense given that 4-*t*Bu shuttlecocks self-assemble into long stacks, creating a much better macroscopic fullerene network throughout the active layer than 4-Me molecules, which phase segregate from the polymer into unconnected islands.[151] Thus, self-assembly can indeed improve the macroscopic network of polymer-fullerene BHJ solar cells, as we demonstrated experimentally in previous work.[150]

Also shown in Table 4.1 are the results of the electronic coupling calculation for a pair of PCBM molecules. We find that the electronic coupling between neighboring PCBM molecules is roughly two orders of magnitude larger than the average coupling between the SC fullerenes. This explains why devices built from the SC fullerenes perform so much more poorly than devices built with PCBM, even though the assembled macroscopic 4-*t*Bu fullerene network is likely better than the random PCBM network: electrons are simply more efficiently moved between PCBM molecules than between SC molecules.

Why is the electronic coupling so much higher between PCBM molecules than other fullerenes? For PCBM, the LUMO and LUMO+1 orbitals are highly delocalized around the molecule in a nearly spherically symmetric fashion, as shown in Figure 4.2a. This allows for greater orbital overlap between neighboring molecules no matter what their relative geometry. In contrast, the frontier orbitals of the 4-*t*Bu and 4-Me shuttlecocks are fairly localized, with the electron density avoiding the regions near and inside the pentaaryl feathers, as illustrated in Figure 4.2b. This means that when the SC molecules are stacked, there is relatively poor overlap of the orbitals on the neighboring molecules: the electron density on the ball of one SC has little overlap with the electron density in the ’bowl’ of the next SC in the stack. The non-spherical orbital distribution of the SCs also explains why the electronic coupling in the non-stacking direction is roughly equivalent to that in the stacked direction, since the electronic overlap in this geometry is equally as poor.

In summary, our calculations suggest that even though pentaaryl fullerenes self-assemble into excellent macroscopic BHJ networks, the electron mobility of these compounds is limited at

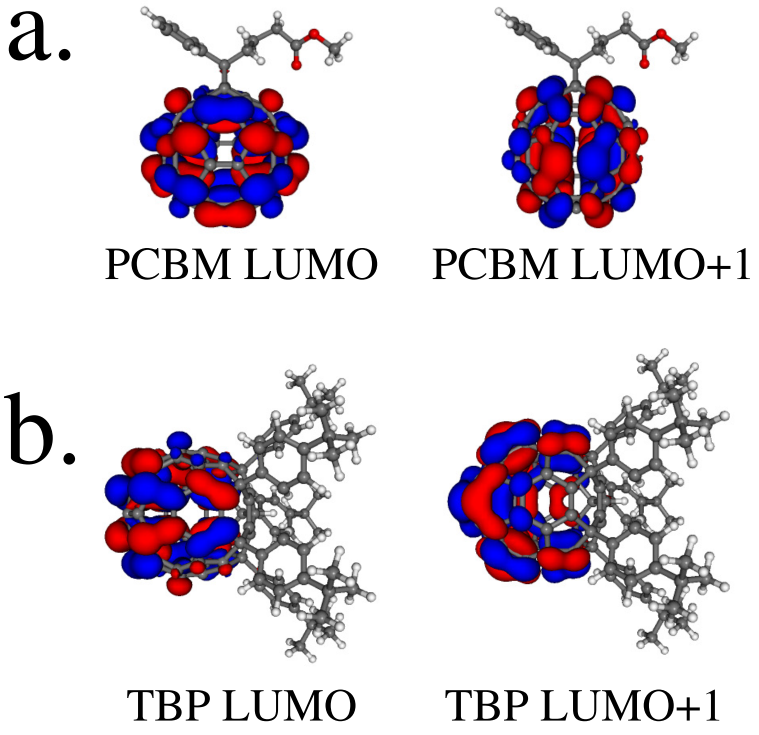

Figure 4.2. Kohn-Sham orbitals from our DFT calculations corresponding to the LUMO and LUMO+1 of the isolated fullerene molecules: a) PCBM, and b) 4-*t*Bu. The orbitals were calculated using the B3LYP functional and STO-3G basis set.

the local, molecular length scale. Moreover, our calculations also suggest that PCBM is a champion electron acceptor for organic photovoltaics because the electron transfer rate between PCBM molecules is not only outstanding, but also is roughly independent of the molecular geometry. In the next section, we turn to time-resolved microwave conductivity (TRMC) to provide an experimental verification of these ideas concerning local mobility. But most importantly, what these calculations tell us is that if one wishes to create new self-assembling fullerene acceptors, a key design goal must be to have strong orbital overlap between adjacent fullerenes.

4.2.2. Local Electron Mobility Determined through Time-Resolved Microwave Conductivity

Although there are numerous methods for estimating the mobility of the carriers in organic photovoltaic devices (e.g., fitting space-charge-limited current models to single-carrier diodes built from the active materials,[161] building field effect transistors from the materials,[162] various transient photovoltage and photocurrent experiments,[163–166] etc.) all of these methods measure carrier motion only at the macroscopic, device length scale. Moreover, most of these methods also are sensitive to the nature of the contacts between the electrodes and the active material(s). To experimentally probe the local mobility of photogenerated carriers, it is necessary to turn to an electrodeless pump-probe method. Flash photolysis TRMC provides exactly such a method,[167,168] and thus offers the perfect test bed for comparing our calculations in the previous section to an experimental measure of local electron mobility; the TRMC technique has been used previously to comparing local and network-wide hole mobility in samples of P3HT.[74]

The flash photolysis TRMC technique measures the time dependent change of the microwave power in a cavity that contains the sample following the photogeneration of charges in that sample. The microwave power absorbed is directly related to the photoconductance of the sample, which is proportional to the yield of photogenerated carriers per photon absorbed (φ) and the (sum of the) high-frequency (local) effective mobility ($\Sigma\mu$) of those carriers.[169] For TRMC experiments, the measured photoconductance peak (ΔG_{peak}) is given by:

$$\Delta G_{peak} = \beta q_e d(n\mu_e + p\mu_h) \qquad (3)$$

where β is the ratio of the interior dimensions of the microwave waveguide (2.2 for our experimental set-up), q_e is electronic charge, d is the sample thickness, and n and p are the density of the photogenerated electrons and holes, respectively. Since it is difficult to measure the densities of the individual carriers, Equation (3) is usually rewritten as:

$$\Delta G_{peak} = \beta q_e I_0 F_A \varphi(\mu_e + \mu_h) \qquad (4)$$

where I_0 is the incident flux of photons used to excite the sample to create photoconducting carriers, and F_A is the fraction of those photons that are absorbed, given by $F_A = 1 - 10^{-\mathrm{OD}}$, where OD is the optical density of the sample at the excitation wavelength. Since β, q_e, I_0, and F_A are all easily measured, the TRMC experiment directly yields the product of the yield (or quantum efficiency) of free carriers per absorbed photon (ϕ) and the sum of their mobilities, $\mu_e + \mu_h$, or $\varphi\Sigma\mu$. Details of how we perform our TRMC measurements are described in the Supporting Information.

To understand the nature of the local mobility for the molecules we examined theoretically in the previous section, we prepared BHJ films of P3HT with both the 4-Me and 4-*t*Bu shuttlecock molecules and with PCBM. For some samples, we prepared the BHJ blends in a manner identical to our previous work studying photovoltaic devices made from these materials

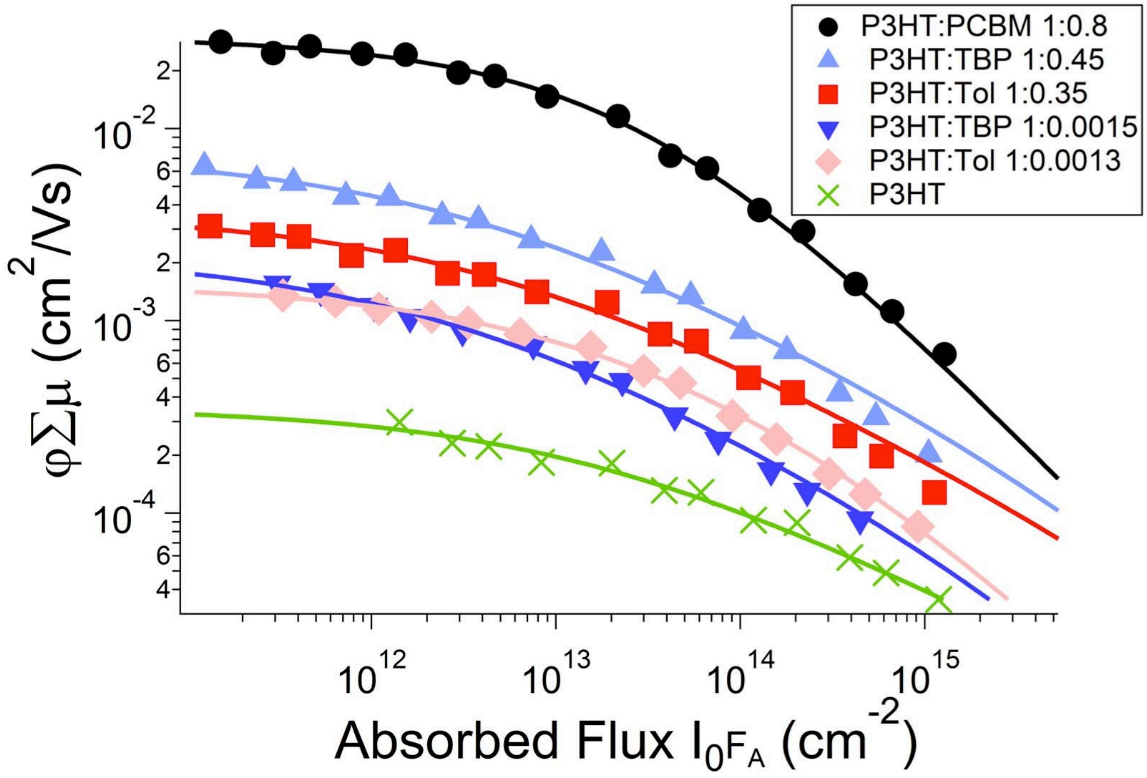

Figure 4.3. The dependence of φΣμ calculated from the measured TRMC photoconductance via Equation 1, on absorbed photon flux ($I_0 F_A$) for pure P3HT and blends with different fullerenes.

using equimolar ratios of PCBM, 4- *t* Bu, and 4-Me (polymer:fullerene weight ratios of 1:0.8, 1:0.45 and 1:0.35, respectively);[151] for others, we used very low loadings of the different fullerenes (P3HT:fullerene weight ratios of 1:0.0015 and 1:0.0013 for 4-*t*Bu and 4-Me respectively). Figure 4.3 shows how the φΣμ product—the carrier yield times the effective mobility—varies in all of our samples as a function of absorbed photon flux. Although Equation (4) predicts a linear relationship between ΔG_{peak} and I_0F_A, there is a sublinear relationship at higher light intensities observed in Figure 4.3 that is due to exciton-charge annihilation, which causes the carrier concentration (φ) to drop at high excitation intensities. [56] Since our experimental apparatus cannot measure the absorbed microwave power at intensities low enough to be entirely in the linear regime to extract an extrapolated low-light intensity value for φΣμ. These extrapolated values are summarized in Table 4.2 .

The first thing that is clear from Figure 4.3 and Table 4.2 is that the BHJ samples with low loadings of fullerene show increased photoconductivity compared to pure P3HT. This results from the fact that the presence of even a limited number of fullerene acceptors greatly increases the number of photogenerated carriers relative to pure P3HT.[169] We find that at these low acceptor loadings, the photoconductance of both the 4-*t*Bu and 4-Me pentaaryl fullerenes are fairly similar to each other, although different from what has been measured previously for low concentrations of PCBM in P3HT.[169] Since we expect the mobility of the holes on P3HT to be independent of the choice of fullerene at such low concentrations and there to be little electron mobility when the fullerenes are isolated at such low concentrations, most of the difference in photoconductance we measure must result from differences in the number of photogenerated carriers when different fullerenes are used. We will use this difference in carrier yields for different fullerenes, in combination with photoluminescence quenching experiments,

Sample	φΣμ	Exciton Lifetime [b)]	PL Quenching Carrier Yield	TRMC Carrier Yield	ns/ps Yield Ratio	'Corrected' ns Yield	Hole mobility[c)]	Calculated electron mobility[c)]
P3HT:4-Me 1:0.0013	0.15	121	41%	11%	0.26	NA	1.4	0
P3HT:4- *t* Bu 1:0.0015	0.21	128	37%	15%	0.40	NA	1.4	0
P3HT:4-Me 1:0.35	0.30	78	62%	NA	0.26[d)]	16%	1.4	0.44
P3HT:4- *t* Bu 1:0.45	0.60	43	79%	NA	0.40[d)]	32%	1.4	0.49
P3HT:PCBM 1:0.8	2.79	47	77%	NA	NA	77%	1.4	2.2
Pure P3HT	0.02	204	NA	1.4%	NA	NA	1.4	NA [a)]

Table 4.2. Summary of low-light-intensity photoconductance and average exciton lifetimes in differene P3HT:fullerene blends.

to extract the local mobility of electrons among the network of different fullerenes present at device loadings, as described further below.

Figure 4.3 and Table 4.2 also show that increasing the concentration of fullerenes in P3HT blend films to that present in typical photovoltaic devices further increases the photoconductance signal. Moreover, blend films containing 4-*t*Bu show a higher photoconductance than samples utilizing 4-Me as the acceptor, and neither of the SC fullerenes gives a photoconductance as high as that in P3HT:PCBM blends. To understand where these differences in photoconductance come from at high loadings, we examined the photoconductance decay profiles of the different blends, which are shown in Figure 4.4. The difference we observe between the photoconductance decay profiles of the P3HT:PCBM blend and that of pure P3HT has been attributed in previous work to differences in the type of carrier that dominates the TRMC signal: the mobility of electrons in PCBM is higher than that of holes in P3HT, hence the electrons dominate the photoconductance in the P3HT:PCBM sample.[169] The slow decay of ΔG observed in this case is attributed to slow bimolecular recombination at low excitation intensities. In contrast, the photoconductance decays of the P3HT:SC blends are similar to those of the pure P3HT sample, indicating that for these blends the dominant ΔG term arises from the holes in P3HT, which have distinctly different dynamics than the electrons. Although Figure 4.4 only shows representative transients at a specific excitation intensity, this observation holds at all the light intensities we used in this work. We therefore conclude that in P3HT:SC blends, the electron mobility in the SC domains is lower than the hole mobility in P3HT, and thus significantly lower than the electron mobility in PCBM.

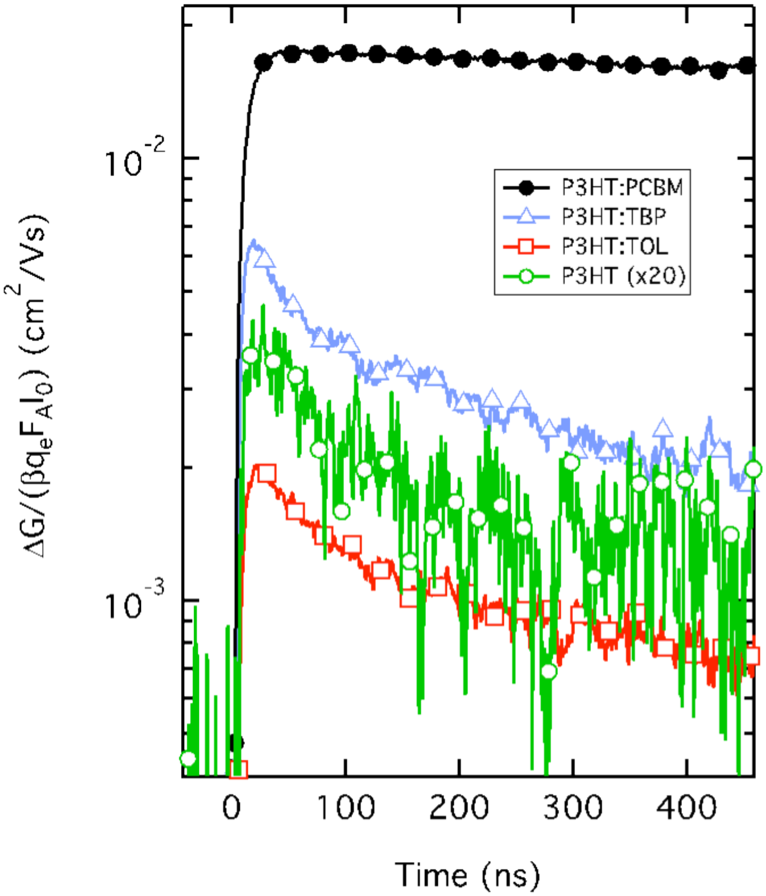

Figure 4.4. TRMC photoconductance transients (normalized for absorbed photon flux and physical constants, see Equation (4)) for P3HT-based samples at device loadings with different fullerenes. The photoexcitation wavelength was 500 nm, and the data shown are for an absorbed photon flux of 10^{12} cm^{-2}, which corresponds to a fluence of 0.56 mJ/cm^2. The results were similar, however, at all photon fluxes examined in this work.

Even though the photoconductance decay profiles in Figure 4.4 show that the electrons on different fullerenes have different local mobilities, the data does not allow us to directly make quantitative mobility comparisons between the samples. This is because the overall carrier yield at high fullerene loadings not only depends on the fullerenes' intrinsic ability to split excitons, but also depends on the donor/acceptor interfacial area, which is sensitive to the degree of phase segregation between P3HT and the different fullerenes. Thus, to extract quantitative information about differences in local carrier mobility among the different fullerenes, we need to find a way to determine the carrier yields (φ) in the blend films with different fullerenes. We chose to estimate φ from the degree of fluorescence quenching observed via time-correlated single photon counting (TCSPC). We excited each of our TRMC samples at 510 nm and monitored the decay of the photoluminescence (PL) at 720 nm, producing the TCSPC data shown in Figure 4.5. After deconvoluting the instrument response function and fitting the resulting PL transients to a sum of two exponentials, we obtained the PL lifetimes given in Table 4.2. Presuming that every quenched exciton produces carriers that survive on the TRMC time scale, fluorescence quenching provides a direct measure of the fraction of absorbed excitation photons that produce charge carriers. Unfortunately, not all of the carriers generated through exciton quenching survive to the ns time scales measured in TRMC. We can estimate how many carriers survive to this time scale, however, using our measurements on the dilute fullerene-containing samples. Since all of the measured photoconductance in these samples comes from hole mobility on P3HT, we can use the literature value for P3HT's TRMC hole mobility (0.014 cm^2/Vs [167,169]) to calculate φ for each of the different fullerenes on the TRMC time scale. We can then compare this value of φ to that determined from our PL quenching measurements to determine the ratio of carriers generated on the ps time scale to those that survive on the ns time scale.

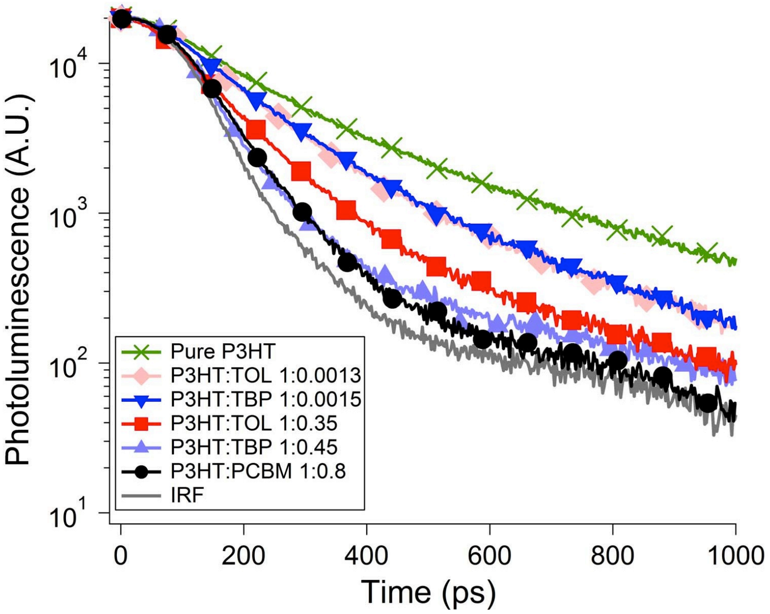

Figure 4.5. Fluorescence quenching of the polymer:fullerene blend samples used for the TRMC experiments shown in Figure 4.3 measured by time correlated single photon counting. Symbols have the same meaning as in Figure 4.3.

Using this procedure, we were able to determine the local electron mobilities of the 4-Me and 4-*t*Bu SC fullerenes at device-level loadings. Table 4.2 shows that at high concentrations, the 4-*t*Bu pentaaryl fullerene has a PL lifetime that is shorter than that of the 4-Me molecule, indicating that there is ~30% more PL quenching for P3HT:4-*t*Bu blends than for P3HT:4Me blends. This result is in excellent agreement with steady-state fluorescence measurements in our previous work, and can be attributed to the enhanced phase separation of the nonstacking 4-Me molecule relative to the self-assembling 4-*t*Bu.[151] Thus, even though the photoconductance of the 4-*t*Bu sample at device loadings is higher than that of the 4-Me sample, most of this difference results from changes in carrier yield. In fact, when we use the information from the dilute samples, we conclude that on the ns time scale of TRMC, the carrier yield for the 4-*t*Bu sample is roughly twice as large as for the 4-Me sample. Since the measured photoconductance for these two samples also differs by a factor of two, this means that the local mobilities of these two SC fullerenes must be roughly similar, in accord with the DFT calculations presented in the previous section. This also implies that the dramatic differences in device performance observed between BHJs with these two fullerenes must result from differences in the macroscopic mobility of the fullerene network, verifying that the self-assembling 4-*t*Bu molecule forms a significantly better interpenetrating network than its non-assembling 4-Me analogue.

Also of interest in Figure 4.3 and Table 4.2 is the fact that the PL lifetimes of P3HT:4-*t*Bu and P3HT:PCBM blends at device loadings (high weight ratios) are essentially identical, resulting in fairly similar carrier yields on the ps time scale of the TCSPC measurement. If we continue to assume that the hole mobility of P3HT does not change when increasing fullerene loading, then the difference in the TRMC-measured $\varphi\Sigma\mu = \varphi(\mu_e + \mu_h)$ product at higher fullerene loadings are caused both by a decreased φ and a decreased local electron mobility for the SCs relative to PCBM. We note that the value for the local electron mobility that we extract for PCBM at the 1:0.8 blend ratio is somewhat lower than previously reported, which is caused by the different processing conditions used here. Our analysis confirms, however, that the local electron mobility in PCBM is at least a factor of five higher than that in 4-*t*Bu, as summarized in Table 4.2. This is also consistent with our DFT calculations in the previous section, and verifies that the reason PCBM is such a good electron acceptor for use in polymer blend solar cells is because it has outstanding local mobility due to the strong overlap of the LUMOs between adjacent molecules, even though it doesn't necessarily form the best macroscopic BHJ network.

Finally, to examine how the macroscopic fullerene network changes with the different SCs molecules, we constructed diodes out of films of the pure 4-*t*Bu and 4-Me molecules; the details of the fabrication and construction of these fullerene-only diodes are given in the Figure 4.6. We fit the measured current-voltage curves for these SC diodes to the Mott-Gurney law, and extracted the space-charge limited macroscopic electron mobilities for these fullerenes of 3.9 and 0.7×10^{-6} cm^2/Vs for 4-*t*Bu and 4-Me, respectively. Since the local electron mobilities of these two fullerenes are similar to each other (0.49 and 0.44×10^{-2} cm^2/Vs), this result verifies that the nature of the electron-conducting network is also important for macroscopic mobility/overall charge extraction. Although carriers may be able to move with similar ease between adjacent 4-*t*Bu and 4-Me fullerene molecules, the global network formed with the 4-*t*Bu fullerene is more than five times more effective at moving charges across macroscopic distances than the network formed by 4-Me fullerenes. It is important to emphasize that this conclusion was based on diodes fabricated from pure fullerene films, so the data is influenced only by the macroscopic connectivity of the fullerene network and not by polymer/fullerene

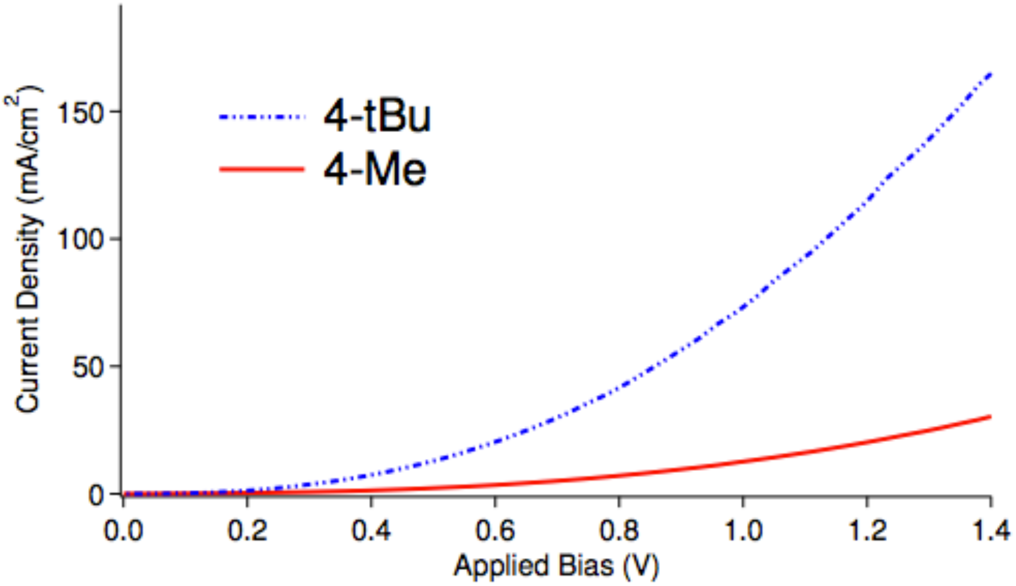

Figure 4.6. SCLC curves for 4-tBu and 4-Me.

phase separation. For comparison, it is worth noting that the space-charge limited electron mobility of both SC fullerenes is much lower than that of PCBM (2.0×10^{-4} cm^2/Vs[170]). Thus, as we have argued throughout this work, both network formation and good local electronic coupling are important to obtain efficient charge extraction from an organic photovoltaic device.

4.3. Conclusions

In this paper, we have used both theoretical and experimental techniques to better understand the distinction between the local mobility and the macroscopic mobility of electrons on the fullerene network of polymer-based BHJ photovoltaic devices. Our work shows that there are indeed two significant components to electron mobility: the intrinsic ability of electrons to move between adjacent fullerenes (local mobility), and the overall architecture and morphology of the fullerene network on device length scales (macroscopic mobility). The macroscopic mobility is what is typically measured in device physics experiments, and we have shown that a good understanding of local mobility can be obtained from a combination of DFT calculations and TRMC experimental measurements.

To understand the differences between local and macroscopic mobility, we examined the behavior of BHJ blends of P3HT and a pair of pentaaryl fullerene derivatives that have an identical electronic structure but different propensities to self-assemble on macroscopic length scales. Our DFT calculations found that the coupling between adjacent molecules is quite similar for the self-assembling 4-*t*Bu and non-assembling 4-Me shuttlecock fullerenes, so that with their nearly identical electronic structure, their local electron mobilities are also nearly identical. Our TRMC experiments on blends of these fullerenes show that the local electron mobilities on these are indeed comparable; the slightly higher net local mobility for the 4-*t*Bu molecule is likely directly related to the fact that self-assembly can assist mobility even on the local length scales probed by TRMC. More importantly, however, photovoltaic devices fabricated with 4-*t*Bu show dramatically better performance than those fabricated with 4-Me and diodes built from 4-*t*Bu have a higher space-charge limited mobility than those built from 4-Me, verifying that changes in the macroscopic network morphology affect device performance even when the local mobilities are comparable.

We also used the idea of separate local and macroscopic electron mobilities to understand why PCBM is the fullerene of choice for nearly every polymer-based photovoltaic. Our DFT calculations show that the local electronic behavior of PCBM is nearly ideal for solar cells: the coupling between adjacent molecules is very high, and the delocalization of the frontier orbitals allows for efficient charge transfer in almost every orientation. This is in contrast to the SC fullerenes, whose frontier orbitals are perturbed by the presence of the pentaadducts, leading to poorer electronic overlap. Our TRMC experiments verified that the local electron mobility on PCBM is significantly higher than that on the SC fullerenes, consistent with the fact that PCBM consistently produces the best photovoltaic devices.

Finally, all of our results suggest that there is further room for improvement in the fullerene component of polymer BHJ solar cells. Since self-assembly can produce macroscopic networks that dramatically improve device performance, it seems clear that designing new fullerenes that both self-assemble and have high local electron mobilities should produce devices that are even better than those using PCBM, particularly since it has been argued that electron mobility on the fullerene network is what limits overall device performance.[14] Furthermore PCBM has a low LUMO compared to novel fullerene acceptors like ICBA.[171] Future fullerene acceptors that utilize self assembly and possess a higher lying LUMO will potentially lead to improvements in both open circuit voltage and short circuit current. The fact that our DFT calculations are corroborated by experiment means that we can design new fullerenes and test them for local mobility before synthesizing them. In combination with TRMC and other measurements, this should provide a way to explore new self-assembling fullerenes that are simultaneously optimized for both local and macroscopic electron mobility, thus helping polymer-based photovoltaic devices to reach their ultimate potential.

CHAPTER 5

On the Structure and Conductivity of Semiconducting Polymer Hydrogels

5.1. Introduction

Conjugated polyelectrolytes (CPEs) are a class of polymers that consists of a π-conjugated backbone with ionic pendant groups.[172–175] Due to the charged side chains, these CPEs can self-assemble into various motifs, including nanoparticles[176–178] and rods.[175,179,180] This assembly is driven by the kinetics of polymer aggregation in various solvents, and can result in changes of physical properties, including absorption[181,182] and conductivity.[179] Due to these unique properties, these assembling materials have been integrated into organic photovoltaics[183,184,3] and sensors[185,186] and have been used for biomedical imaging.[187–189]

These CPEs have the ability to form hydrogels if the building blocks self-assemble into extended structures. For example, cetyl trimethyl ammonium bromide (CTAB) can be induced to form long worm-like micelles which can result in gel formation.[190] Polymer hydrogels consist of a three dimensional network held together either by chemical or physical means. A chemical hydrogel requires cross-linkers to create an interconnected network;[191–193] whereas a physical hydrogel network is held together by electrostatic interaction of charges, Van der Waals forces, hydrogen bonds, etc.[194,195] The <10 nm structure of most gel networks is challenging to characterize through standard methods such as transmission electron microscopy (TEM) because these disordered networks both lack periodicity, and consist mainly of carbon, which lacks a high electron density needed to achieve high contrast over such small distances. In this work TEM is used to observe the existence of an interconnected network of rod-like micelles. This is then complemented by solution phase small angle x-ray scattering (SAXS), Dammin bead modeling, and rheology, which are used to deduced more about the hydrogel structured via indirect methods.

The structure of CPEs is essential to their implementation in electronic devices. For example, in organic photovoltaics (OPVs) a continuous nanostructured polymer network is required for movement of charges out of the devices.[4] When discontinuous networks form in real devices due to polymer aggregation kinetics, photogenerated current is lost. By circumventing these issues with a self-assembling polymer system that forms fully interconnected networks, we could potentially create thermodynamically stable films that could be beneficial for electronic devices.

In this study we show that the conjugated polyelectrolyte, poly(fluorene-alt-thiophene) (PFT), self-assembles into a network of cylindrical micelles in solution. Cryo-TEM provides a visualization of the polymer micelles that form in dilute solutions. Using solution SAXS in combination with Dammin bead modeling, we are able to determine the size and shape of the micelles as well as the branching structure. Finally, with rheology, we are able to determine the strength of the polymer network, and postulate the type of connection that promotes gel network formation. Dammin bead modeling is used to visualize that improvement in network connectivity, and time-resolved microwave conductivity (TRMC) is used to show how THF annealing can be used to increase charge carrier mobility. The strongly interconnected network formed in PFT gels could increase local conductivity in heterogeneous networks of conjugated polymer chains, creating an ideal system for charge transport through a nanostructured organic thin film.

5.2. Experimental

Polymer synthesis was performed as previously reported.[179] To further purify the PFT into high and low molecular weight fractions, 250 mg of PFT was dissolved in 5mL of DMSO. Once dissolved, ethyl acetate was added to the PFT/DMSO solution until the polymer began to precipitate out of solution. At this point the solution was centrifuged to pull the precipitated PFT out of the suspended solution. The solution was poured off and the PFT was dried, this fraction is what we refer to as high MW PFT. More ethyl acetate was added to the remaining solution and the rest of the polymer is precipitated out of solution, this fraction is what we refer to as low MW PFT.

Tetrahydrofuran (THF) annealing was performed by adding 0.05 mL of THF to 0.5 mL of H_2O with various amount of PFT. The PFT gel becomes a liquid upon addition of THF. The THF is then removed by heating and stirring at 80°C for 4 hours. The removal of THF was studied by mass spectroscopy to determine the optimal temperature and time required to remove THF.

Cryo imaging grids for transmission electron microscopy were prepared by placing a small drop (~4 μl) of sample solution onto glow discharged holy carbon mesh Quantifoil 200 mesh grids with 3.5 μm holes spaced 1 μm apart. The grids were then blotted and plunged immediately into liquid nitrogen cooled liquid ethane to rapidly freeze the samples in vitrified ice. The cryo grids were visualized with an FEI Tecnai F20 transmission electron microscope with an accelerating voltage of 200 kV. Images were collected at ~50,000x magnification with a defocus of approximately 3 μm.

Small-angle X-ray scattering (SAXS) experiments were conducted at the Stanford Synchrotron Radiation Lightsource (SSRL) Beamline 4-2. Using a syringe, 100 μL of each sample was loaded in a quartz capillary and held at 25°C. Scattered X-rays (at 12 keV) were collected with a Rayonix MX225-HE detector (sample to detector distance = 1.7 m). The two-dimensional data was radially averaged to obtain one-dimensional scattering curves.

Bead models were performed on the solution SAXS data using Dammin, a Monte-Carlo type modeling software that uses beads and solvent to fit a shape that could have generated the experimental curves. The expert setting was used and the bead size set to have a radius of 5 Å, corresponding to the width of a single polymer chain. The diameter of the sphere was set to be 140 Å. Each data set was run at least five times to ensure trends were comparative. Only a subset of the overall data is shown in the figures.

Rheological properties were measured on a Rheometrics RFS2 strain-controlled rheometer. The geometry used was the cone-and-plate for both strain-controlled and frequency-controlled experiments. Strain-controlled measurements were performed at a constant frequency of 5% and the frequency-controlled measurements were performed at a strain of 1 rad/s.

Flash photolysis time resolved microwave conductivity (TRMC) was used to measure photoconductivity using methods that have been previously reported.[196–199] Briefly, samples for microwave conductivity measurements were prepared onto 10 x 24 mm quartz substrates that were cleaned by subsequent ultrasonic baths in detergent, deionized water, acetone and isopropanol for 10 minutes each. Samples are placed into an X-band microwave cavity containing a grating that is transparent to optical excitations but reflective to microwaves. The samples are excited through the quartz substrates by a 5-ns 500 nm laser pulse produced from an Optical Parametric Oscillator (Continuum Panther) pumped by the 355-nm harmonic of a Q-switched Nd:YAG laser (Continuum Powerlite) with a typical fluence of 0.56 mJ/cm^2. The intensity of the excitation was controlled by switchable neutral density filters. The photoinduced carries absorb the incident microwaves, and the change in microwave power is measured and related to the conductance of the sample.

5.3. Results and Discussion

The chemical structure of PFT is shown in Figure 5.1a. This CPE can form micelles in water because of its amphiphilic character and because each monomer unit has an overall wedge-shaped with a large hydrophilic volume, a fact that results from the sp^3 carbon on fluorene unit where the charged side chains attach.[179,200] These factors, combined with the fairly linear nature of the PFT backbone, allows, PFT assembles into rod-like micelles where the backbone of PFT runs along the long axis of the micelle, as shown by cartoon illustration in Figure 5.1b and characterized in detail for low molecular weight polymers in our previous work.[179] At concentrations as low as 1 wt/v%, however, PFT forms a hydrogel, illustrated by the inverted vial shown in Figure 5.1c. The molecular weight (MW) of PFT is critical to the formation of the gel network, thus size selective precipitation is used to obtain both high and low MWs. The low MW polymer does not form a gel network, as the high MW polymer does, indicative that the interactions between polymer micelles is based on the polymer chain length. Unless explicitly stated otherwise, all experiments described below use only the high MW polymer fraction.

Using cryo-electron microscopy on dilute solutions (cryo-EM, Figure 5.1d) we can observe both the micellar nature of the PFT assemblies and interconnections between those micelles, which should lead to hydrogel formation at higher concentrations. The cryo-EM samples were prepared by flash-freezing a droplet of PFT solution, and thus they allow us to observe micelles that are both in the plane on of the image, which appear as rods, and micelles

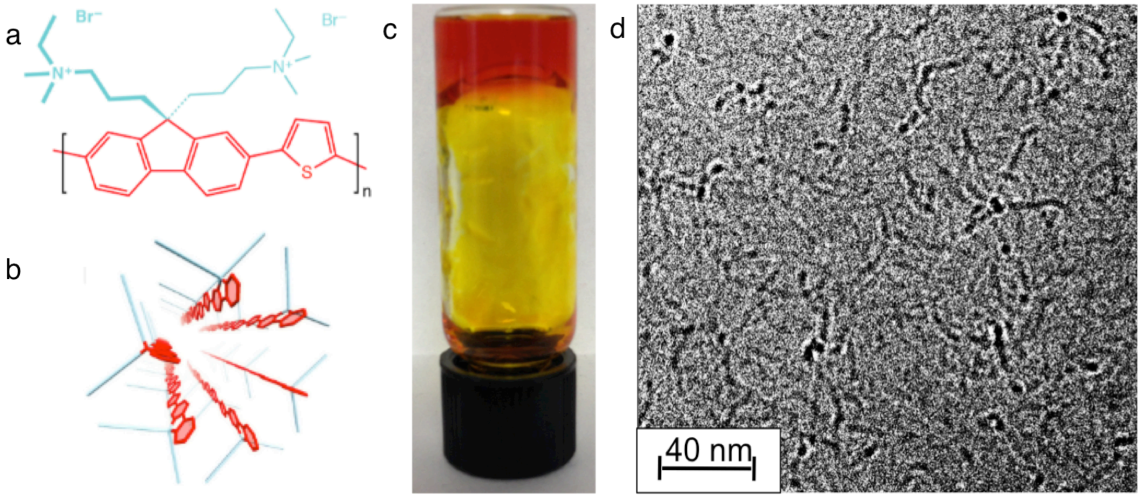

Figure 5.1. a) PFT monomer b) Cartoon of PFT micelle c) Upside-down vial of PFT hydrogel and d) Cryo-TEM of PFT micelles.

standing on end, which appear as darker spots. From this data, we can approximate the diameter of the micelles to be about 4 nm, a size that correlates well with solution SAXS published previously.[179] The cryo-EM data provides clear evidence for PFT micelle formation and for the formation of interconnections between micelles, but because of the limited region that can be imaged at one time, it does not provide good statistical data on the average structure of the sample as a whole.

To further study the structure of the PFT micelle system we thus turned to solution SAXS. Solution SAXS has been used extensively to examine the nanometer scale structure of assemblies in solution.[201–203] By fitting SAXS data to a power law equation, $I = q^{-\alpha}$, we can relate the exponential slope, $-\alpha$, to the structure of the polymer in solution. Figure 5.2a shows that PFT fits to two distinct slopes: -1.5 at low q and -3.7 at high q. The low q value of -1.5 is indicative of a rod-like shape at large distance, concomitant with the length of a rod; the high q value of -3.7 is indicative of a sphere-like shape, concomitant with the radius of the rod. This measured rod-like shape correlates well with the micelle-shapes observed by TEM.

Along with the power-law analysis, the raw data can be fit using the software Gnom to enable smoothing of the data before the bead model analysis. The Dammin bead model fits this smoothed data and outputs a structure that may have caused the scattering data.[204] Comparing the bead models for high and low MW PFT (Figure 5.2b and c, respectively), indicates that the high MW PFT is more branched then the low MW PFT. As stated above, the low MW polymer does not form a gel, while the high MW PFT does. From this data, we thus postulate that the low MW polymer is present mostly in the form of discrete polymer micelles, while the high MW PFT forms a branched network that enables gel formation. The base unit of the polymer hydrogel, as proven by TEM, SAXS, and Dammin bead

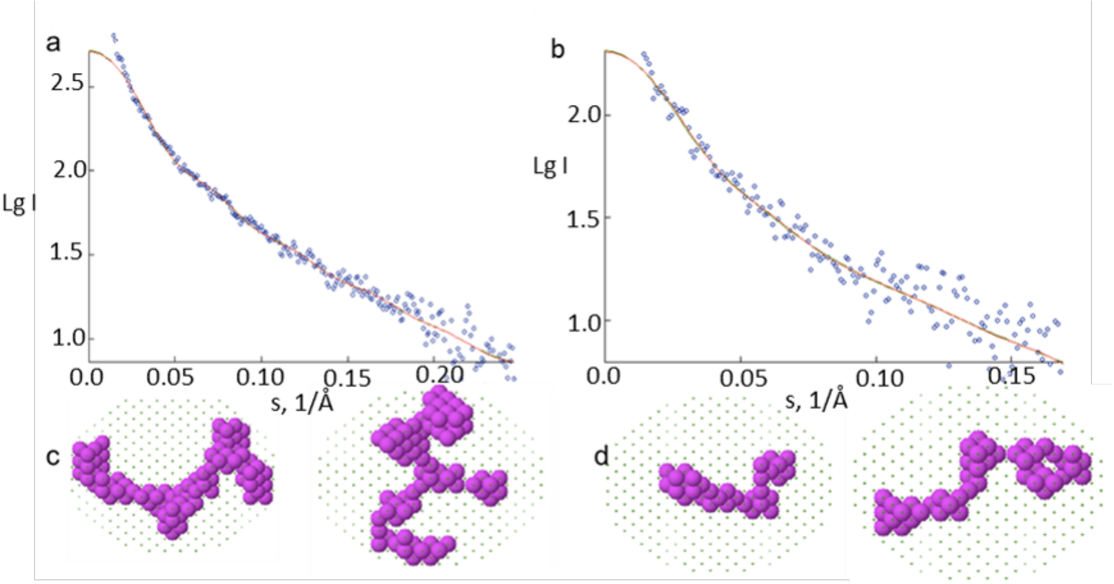

Figure 5.2. Dammin Bead models. Fit of PFT SAXS a) high MW data and b) low MW data. c) High MW PFT bead models and d) low MW PFT bead models

modeling, is the rod-shaped polymer micelle. We will now use polymer rheology as a tool to help determine how that polymer network is held together.

Rheology is the study of the deformation or flow of matter and one of the most useful techniques to use to study the physics of a gel network.[205] Two main components of this study are the elastic modulus (G') and the viscous modulus (G"). The elastic modulus is a measure a of a material's reversible or non-reversible (elastic or plastic, respectively) response to an external force, where the viscous modulus is a measure of a materials resistance to deformation.[206] If the elastic modulus is larger than the viscous modulus, the system is by definition a solid. If a large enough strain is applied to such a solid system then the elastic modulus may dip below the viscous modulus, allowing the system to become a liquid in a process call shear thinning. By studying the viscoelastic response of a conjugated polyelectrolyte hydrogel under various strain and frequency studies, we can learn something about the structure of the gel network.

We begin our rheology experiments with a gedanken model for the structure of the gel network and then attempt to prove or disprove that model. Given the micellar nature of PFT in solution, the very low concentrations where PFT begins to gel, and the fact that PFT has no significant potential to make either covalent or hydrogen bonds between polymer chains, we hypothesize that it is the micelle formation itself that results in gel formation. For example, polymer chains can bridge between micelles, linking micelles together in much the same way that bridging actin fibers bridge between fiber bundles in actin gel networks.[207] We can describe these bridging polymer chains as "sticky ends" because in the absence of a second PFT micelle, a dangling polymer chain is likely to adopt a high energy, coiled conformation in aqueous solution, which would prefer to associate with another polymer micelle.

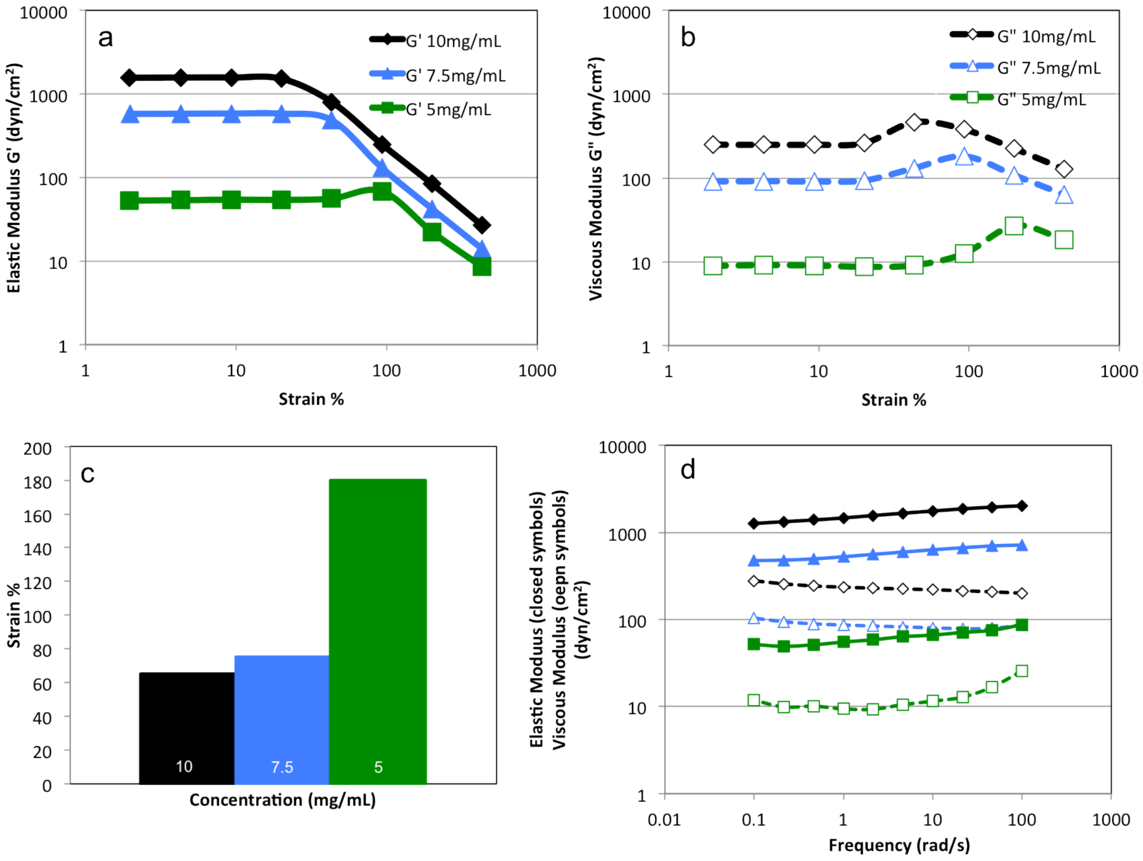

Figure 5.3. Concentration study of 10 mg/mL, 7.5 mg/mL and 5 mg/mL. a) strain-dependent elastic modulus and b) viscous modulus c) gel break point (frequency: 1 rad/s) d) frequency-dependent elastic and viscous modulus (strain amplitude: 5 dyn/cm^2).

We can study the response of these PFT hydrogels, that is both elastic or plastic deformations, under constant strain or constant frequency to help learn about the PFT network structure. Figure 5.3a and b shows the values of G’ and G” as a function of strain amplitude at a constant frequency of 1 rad/s for gels with concentrations of 10, 7.5 and 5 mg/mL. As expected, both the G’ and G” values of the PFT gel increase as the polymer concentration increases, indicating that more concentrated gels have more interconnections. The elastic modulus for PFT shows a linear viscoelastic regime, where the modulus does not change with strain amplitude; this value is often referred to as the plateau modulus. The 10 mg/mL and 7.5 mg/mL samples both show weak strain overshoot,[208] which is where G’ has a linear viscoelastic regime at low strain and then decreases rapidly at high strain. In contrast, G” begins with a linear viscoelastic regime but has an increase or peaks at high strains before decreasing similarly to G’. Structurally, the elastic modulus reflects the number of junctions in the polymer network, where the viscous modulus correlates with the volume that the polymer network occupies. Using this idea, the increase in G” is indicative of an expansion of the network at higher strain amplitude. If the intramolecular interactions of the polymer micelles are disrupted, it should create more unbound “sticky ends”, which should be loosely coiled due to steric constraints, increasing the volume and consequently increasing the viscous modulus of the sample.[209] Because the 10 mg/mL and 7.5 mg/mL samples are too concentrated to allow the polymer chains to reorient, an increase in G’ is not observed. This type of weak strain overshoot is observed in many polymer solutions.[208,210] By contrast, the 5 mg/mL samples shows strong strain overshoot. Strong strain overshoot occurs when an increase is observed in both G’ and G” at higher strain amplitude before the gel network breaks. In this less concentrated sample, the increase of both the elastic and viscous modulus is expected, because lower concentrations mean fewer connections between micelles and a weaker PFT network. When a large enough strain is applied to the system, it disrupts both the polymer micelles and the network. The polymer micelles can then reorient to bridge with other micelles in a more ideal configuration. In this case, we observe an increase in both the number of junctions and in the sample volume. The observation of both weak and strong strain overshoot thus supports the idea that bridging polymer chains are responsible for the formation of the PFT network.

Another important parameter that we can take from this polymer rheology study is the break point or failure point of the gel. The breakpoint of the hydrogel, shown in Figure 5.3c, is the point where the strain amplitude applied to the system is sufficient to cause the network to break so that the entire system begins to flow. In the case of PFT micelles, the bridging polymer chains would need to detach from one micelle and then align, allowing the samples to become liquid-like. There is only a slight difference between the break points for the 10 mg/mL and 7.5 mg/mL gels. However, the 5 mg/mL gel has a breakpoint that is more than twice as high as the 10 mg/mL and 7.5 mg/mL gels. This increase in breakpoint results from the lower density network that has the ability to dynamically reform junctions as strain is applied; this is the same phenomenon that produces the strong strain overshoot. Conclusions from examining the break point of the gel thus agree well with the conclusions gleaned above from the weak and strong strain overshoot.

Frequency dependent measurements can be used to gain further insight about the nature of the gel. The frequency study in Figure 5.3d was performed at a constant strain amplitude of 5%, chosen to be in the plateau region for all gel samples. As in the strain amplitude measurements, we find that G' is always higher than G", proving that we have a solid-like gel. Also, as higher frequency oscillations are applied to the PFT gel, the slopes of the curves remain close to zero. This lack of response with increased frequency is also characteristic of physical gels because the network is strong enough to resist changes.[203] This implies that even though these are not exceptionally strong gels, the interactions that hold the gels together are quite robust. The viscous moduli for the 5 mg/mL sample does vary more with frequency than the 10 mg/mL and 7.5 mg/mL samples, likely due to the fact that the 5 mg/mL is a much less connected gel, and so it is easier to reorient the micelles in this sample at high frequencies. These frequency measurements thus provide further information about the bridged PFT network.

Studying the chemical factors that destroy these PFT hydrogels can also provide information about what holds them together. For example, the gel network is destroyed when PFT is exposed to THF.[211] Upon removal of the THF from the polymer system by thermal evaporation, the gel-network reforms. We hypothesize that this behavior arises because THF can enthalpically stabilize the coiled “sticky end” of the bridging polymer chains, allowing the system to break these low entropy connections between micelles. This process can be followed by SAXS and modeled using Dammin bead models. Figure 5.4 shows representative bead models for PFT samples before THF annealing, with THF, and after THF removal. The effect of THF on the micelle system is clearly observed by the loss of branching after the addition of the THF. The width of the structure has decreased to be approximately the width of a single bead, indicating that the THF causes the solution to become either single PFT chains or much smaller micelles. Upon removal of the THF, the PFT network becomes stronger, with the plateaus modulus increasing from 3380 dyn/cm^2 to 4080 dyn/cm^2, as seen in Figure 5.5a. Apparently, the gel network reforms in a more interconnected state than it is able to attain initially because network formation is kinetically limited when samples are first prepared. In agreement with these

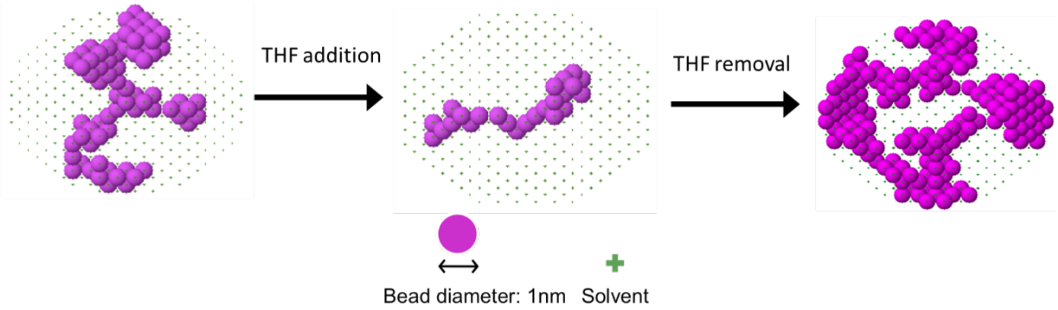

Figure 5.4. Dammin bead model representing before THF annealing, THF annealing and THF removal

ideas, Dammin modeling indicates that upon removal of the THF, both the branched structure and the width of the polymer micelles are restored. Intersting, the branching density increases, indicating that the post-annealed gel network contains more interconnected polymer micelles, compared to its pre-annealed counterpart. SAXS modeling is thus in good agreement with rheological studies and with the idea that THF annealed samples have a more interconnected network.

If THF annealing increases the density of network connections, then it follows that THF annealing should also increase the conductivity of the PFT network. TRMC is a unique tool that allows for measurement of local mobilities in solid-state films.[169,212] In TRMC photoinduced carriers are created by an incident laser pulse on the sample. The carriers are then induced to move by the electric field from microwave radiation, and the change in microwave power is measured as these photoinduced carriers absorb microwaves. The change in microwave power after passing through the sample is proportional to the local nm-scale photoconductivity of the sample, which is the carrier yield times the sum of the mobilities of all carriers, which in our case is both electron and hole mobilities. Figure 5.5b, shows that the PFT after THF annealing has a 6-fold increase in photoconductivity. If we assume that the carrier yield is comparable in these samples (a reasonable assumption, given their identical chemical nature), then the carrier mobility must be higher in the sample treated with THF. We attribute this increase mobility to both the increased interconnectivity of polymer network after THF annealing, and additionally from decreased chain coiling in the THF annealed samples. It has been shown that kinks and bends in polymer chains can cause trap sites that reduce carrier mobility.[213,214] This data thus suggests that in addition to making more interconnections between micelles, THF annealing may

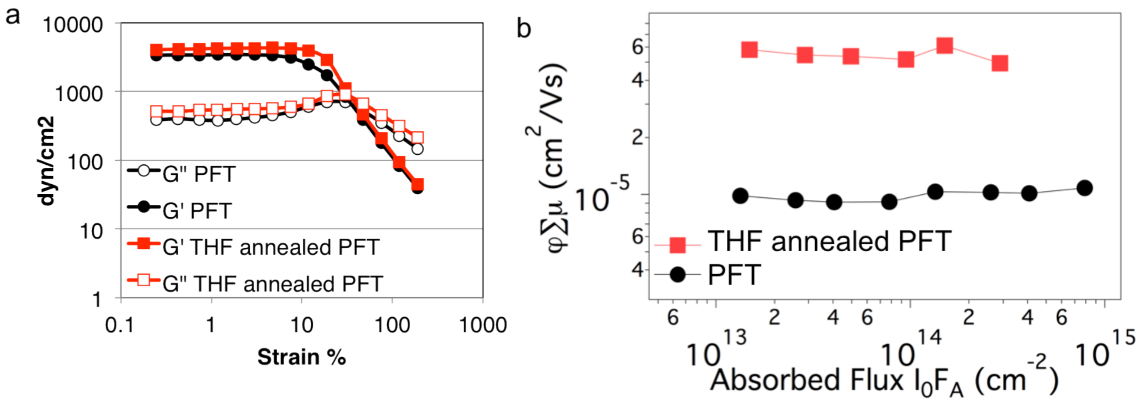

Figure 5.5. a) Strain-dependent curves comparing before and after THF annealing b) TRMC before and after THF annealing (Frequency: 1 rad/s).

also allow for increased polymer ordering within micelles, a fact that could further increase the plateau modulus.

While the experiments described above provide much information about the nature of these PFT hydrogels, they do not concretely prove the idea that bridging polymer chains act as "sticky ends" that link micelles together. To further support this model, we take advantage of the fact that we obtain both high and low MW PFT by size selective precipitation from a single polymer synthesis. Here we selectively recombined the high and low MW PFT at various ratios, maintaining the same overall polymer concentration, to further support our bridging-polymer hypothesis for gel formation. As a reminder, we know that the low MW PFT does not form a gel, where high MW PFT does. Figure 5.6a and b shows the G' and G" respectively for a series of samples that all contain a total concentration of 10 mg/mL, made up of different fractions of low and high MW polymer. The samples contain polymer ratios of 9 mg high MW PFT to 1 mg low MW PFT (9:1), 8 mg high MW PFT to 2 mg low MW PFT (8:2), and 7 mg high MW PFT to 3 mg low MW PFT (7:3). There is also a pure high MW 10 mg/mL PFT sample (10), which has no low MW PFT. This is the strongest gel and is used as a standard of comparison for all of the mixed high and low MW PFT samples. There is an order of magnitude decrease in plateau modulus between the 10 mg/mL and the 9:1 samples, and another order of magnitude decrease between the 9:1 and 8:2 samples. The plateau modulus for the 7:3 sample is yet another four times lower than the 8:2 sample. This decrease in the strength of the gel is caused not just by the decreasing amount of high MW polymer, but also by the addition of the low MW PFT. For example, the pure 7.5 mg/mL sample in Figure 5.3a has a G' plateau value of 575 dyn/cm^2, where the 7:3 sample, which contains a very similar amount of high MW polymer, has a G' plateau value of just 4.5 dyn/cm^2. The overall concentration of high MW polymer in both

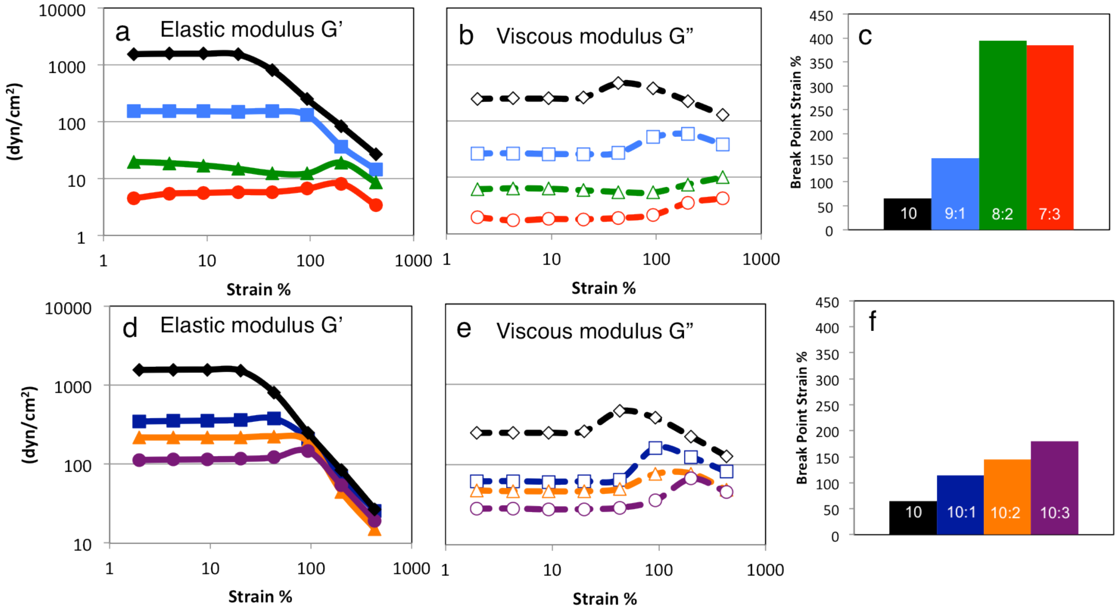

Figure 5.6. Constant overall concentration study a) elastic modulus, b) viscous modulus and c) break point. Constant high MW concentration study d) elastic modulus, e) viscous modulus and f) break point. (Frequency: 1 rad/s)

samples is very similar, but the elastic modulus is two orders of magnitudes less in the mixed sample than the high MW 7.5 mg/mL sample. We postulate that the reason for the decrease in gel strength is due to the fact that the low MW polymer is able to cap the “sticky ends” of the high MW PFT micelle, allowing the high MW polymer to achieve an enthalpically favorable conformation without the entropic constraints of bridging between micelles.

More information can be obtained by again focusing our attention on strong and weak strain overshoot. The pure 10 mg/mL PFT samples and the 9:1 samples show only weak strain overshoot, where the 8:2 and 7:3 samples show strong strain overshoot. This suggests that there are still sufficient interconnections in the 9:1 sample to prevent dynamical network reformation under strain. However, with the 8:2 and 7:3 samples, the ends of the micelles are capped with the low MW PFT, when strain is applied the low MW PFT may transiently disengaged from the high MW PFT so that the “sticky ends” can bridge polymer micelles. The breakpoint, in Figure 5.6c, also increases from the 10 mg/mL samples to the 9:1 sample. The 8:2 and 7:3 breakpoints are similar, but these are both very weak gels again, and we do expect an increase in the breakpoints due to the strong strain overshoot.

While the data presented above provides strong indication that low MW PFT disrupts the nature of the gel network, the fact that the total amount of high MW PFT is not constant in these samples, complicates the issue. We thus performed a second set of experiments using a fixed concentration of high MW PFT concentration and a varying total polymer concentration. For this experiment in Figure 5.6d and e, the concentration of high MW PFT was kept at 10 mg/mL, and low MW PFT was added in 1, 2, and 3 mg amounts (10:1, 10:2, 10:3). Here again we observe a decrease of G’ and G” (Figure 6d and e) upon the addition of low MW PFT, despite the fact that the total polymer concentration increases. The decrease of the elastic modulus after

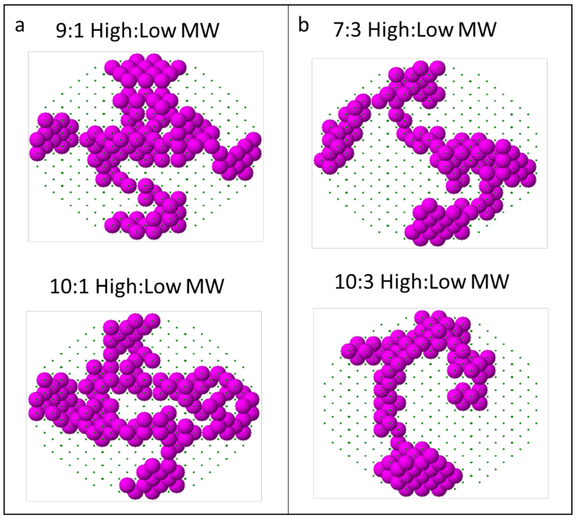

Figure 5.7. Dammin bead models a) constant overall concentration study b) constant high concentration study

addition of 1 mg of low MW PFT is roughly an order of magnitude, although it is less than that observed in Figure 5.4a for the 9:1 sample. Indeed, the plateau modulii show a decrease as more low MW PFT is added to the system. Weak strain overshoot is observed for the 10:1 and 10:2 samples, while strong strain overshoot is found in the 10:3 sample. It follows that the 10:1 and 10:2 samples still exhibit significant micelle bridging, as the ratio of low:high MW PFT is not high enough to effectively break up the gel network. However, in the 10:3 samples, enough low MW PFT is present to cap the ends of the polymer micelles and disrupt the network. Notice the breakpoint in Figure 5.4f steadily increases as the low MW PFT is added, but it is not as large of an increase as in Figure 5.4c. This data thus indicates that both the total concentration of high MW polymer, and the low MW:high MW ratio interplay to control the density of connection within the network.

The structural effect of adding low MW PFT to high MW PFT was further analyzed using solution SAXS and Dammin bead modeling on diluted, 1mg/mL, samples. Figure 5.7 shows the fits for only the 9:1, 7:3, 10:1, and 10:3 high MW:low MW samples. In comparing the 9:1 and 7:3 samples, we find that although the total polymer concentration is the same, the density of beads in the two models differs, indicating that in the 7:3 sample, a larger fraction of the polymer chains are individually dissolved or in the form of very small aggregates, too small to see in the scattering vector range used for this experiment. The 9:1 sample contains a higher density of beads, indicating larger aggregates in solution, and possibly higher branching overall. When the 10:1 and 10:3 samples are compared, we see a similar trend. Here, a higher bead density might be expected for the 10:3 sample due to the higher overall polymer concentration, but the opposite effect is observed. Although the 10:1 sample contains less polymer and the same amount of high MW PFT as the 10:3 sample, a higher overall bead density is observed, again indicting larger aggregates in solution for the 10:1 sample. More branching can also be seen in the 10:1 sample. This bead modeling thus supports the idea that low MW PFT caps the sticky ends of bridging high MW PFT strands, resulting in less branching, and more linear, single rod structures in samples with more low MW polymer.

5.4. Conclusions

In this study we examined the network structure of semiconducting polymer PFT hydrogels. TEM and SAXS were employed to examine the micellar building blocks of the hydrogel and Dammin models to the solution SAXS data helped to visualize the network structure and further supported the hypothesis of rod-like micelle building units. Rheology was used to examine interconnections within the gel network, and a combination of TRMC and rheology indicated that a more interconnected and potentially more ordered network was formed after THF annealing of the gel. Lastly, bead models and rheology studies of mixed low MW and high MW networks were used to further our understanding of the interactions that hold this unique semiconducting gel-network together. All of this data together strongly supports a picture where the gel network is held together by polymer chains that bridge neighboring micelles, co-assembling with more than one micelle based on amphiphilic interactions. These bridging polymer chains, or "sticky ends" can be disrupted by either the addition or organic solvents or by adding low MW polymers that can co-assemble with the "sticky ends" in a non-bridging fashion.

A key conclusion that comes from this work is the fact high MW polymer chains bridge between micelles, offering the potential for facile electrical conductivity between micelles. While direct electrical measurements on the hydrogel network are complicated by the high conductivity of water, the TRMC results on dried gel networks are very promising for future device applications. The strongly interconnected nature of these conjugated polymer hydrogel networks could be ideal for a variety of polymer based electronic devices as they rely on good conductivity in a heterostructured network.

CHAPTER 6

Long-Lived Photoinduced Polaron Formation in Conjugated Polyelectrolyte/Fullerene Assemblies

6.1. Introduction

In biological photosynthetic systems, energy cascade structures promote the spatial separation of photogenerated charges created at the reaction center, preventing their recombination. These energy cascade structures require close proximity of the electron donors and acceptors (on the scale of ~1 nm), and the corresponding electron transfer (ET) processes take a few ps[215]. Similar to natural photosynthesis, in man-made organic photovoltaic (OPV) cells, photoexcitations are dissociated into charges at a donor-acceptor interface on sub-ps time scales. But OPVs have the drawback that there is significant recombination of the newly-separated charges, typically on time scales ~20 ps *(2)*. This is because most efficient OPV systems rely on nm-scale phase separation of a conjugated polymer donor and fullerene acceptor into domains of length scale of 10-20 nm to facilitate efficient exciton diffusion and charge transfer [4]. However, the high charge densities present in OPVs, coupled with the low dielectric constant of the organic materials, results in significant carrier recombination before the charges can be extracted through external electrodes, thereby diminishing the device efficiency. If OPVs could be designed to use ET cascade structures that are reminiscent of photosynthetic complexes, it should be possible to improve charge separation and reduce recombination losses[217].

In this work, we describe how molecular self-assembly can be used to enable dissolved OPV materials (conjugated polymers and fullerenes) in aqueous solution to mimic the ET cascade structures of biological complexes, allowing us to 'spatially' control photogenerated charges. We are able to demonstrate efficient long-time charge separation following photoexcitation: the ET cascade we form produces separated polarons that are stable for weeks, a lifetime that is unprecedented for OPV materials. In addition, our use of self-assembly provides potential future advantages in reproducibility and scalability, both of which are major hurdles for conventional OPVs with kinetically-controlled structures[184,218,219]. Finally, the photoinduced charge separation we achieve takes place in water, opening possibilities for 'green' production of artificial photosynthetic devices.

6.2. Results and Discussion

The particular materials we have chosen for this study are a combination of a conjugated polyelectrolyte, poly(fluorene-alt-thiophene) (PFT)[179], and several isomers of the charged fullerene derivative C_{60}-N,N-dimethylpyrrolidinium iodide ($C_{60}(PI)_n$), where *n* is the number of charged pyrrolidinium groups[220]; the chemical structures of these molecules are shown in Figs. 6.1.A-C. PFT is a water-soluble semiconducting polyelectrolyte whose sp^3 carbon yields a wedge-shaped monomer that facilitates the assembly of the polymer into rod-like micelles (Fig. 6.1.B); details of how this polymer assembles have been published previously[179]. Due to the charged nature of the polymer, the electron acceptor(s) must also carry a cationic charge to avoid heterocoagulation. The synthesis of $C_{60}(PI)_n$, depending on the precise conditions, produces products with *n* ranging from 2 and 5, and with multiple isomers for each *n*. To avoid confusion, we will refer to $C_{60}(PI)_n$ with n = 3-5 as 'higher' adducts, and fullerenes with n=2 will be referred to as 'mixed-bis' adducts.

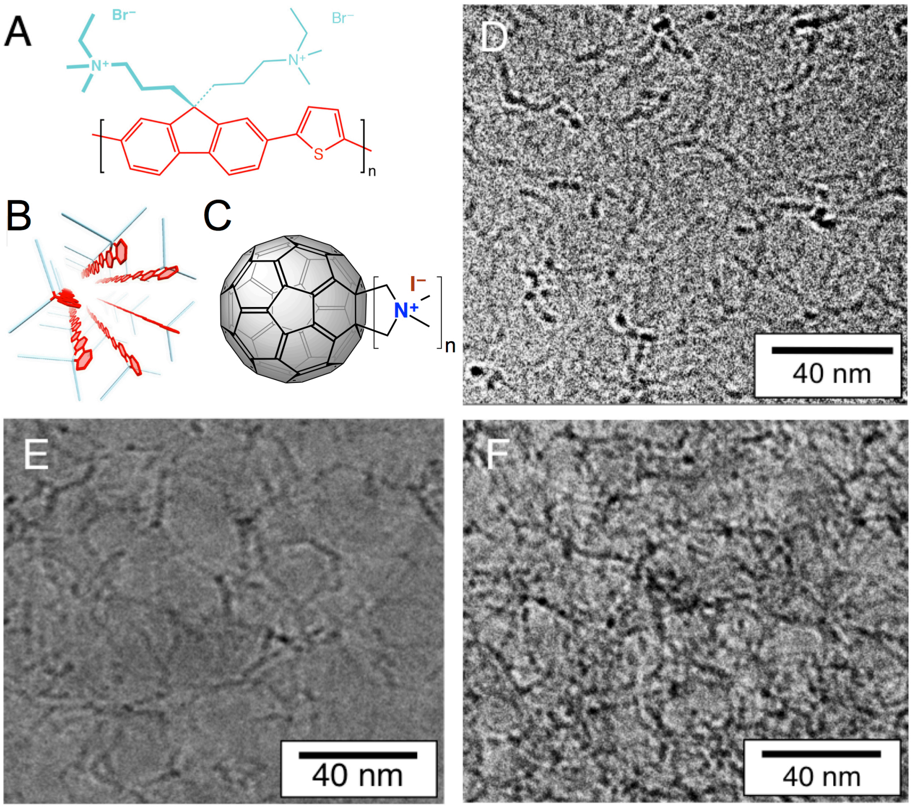

Figure 6.1. PFT and charged fullerene structure and assembly. PFT structure (A), cartoon of a PFT micelle (B), charged fullerenes (C). CryoEM images of pure PFT (D), PFT:'mixed-bis' adducts (E) and PFT:high adducts (F).

To create assemblies, we need to control solution phase aggregation and we do this using solubility. ‘Mixed-bis’ adducts show essentially no solubility (without PFT) in solution, while ‘higher’ adducts are fully water-soluble. This suggests coassembly of ‘mixed-bis’ adducts in aqueous solution with PFT, a result that is confirmed by cryo electron microscopy (cryoEM), small angle X-ray scattering (SAXS), and luminescence quenching studies. CryoEM images of pure PFT, PFT:‘mixed-bis’ adducts and PFT:high adducts are show in Figs. 6.1.D-F. Pure PFT samples self-assemble into branched micelles that are roughly 4 nm in diameter and 40 nm in length. CryoEM images of PFT assembled with ‘mixed-bis’ adducts are visually similar to the pure PFT, indicating association of the $C_{60}(PI)_2$ with the PFT micelles. In contrast, cryoEM images of PFT:high adducts appear blurry, presumably because the solution contains separate PFT and fullerene agglomerates.

This interpretation is supported by SAXS measurements (Figs. 6.2.A-B), and with more statistical averaging. By fitting the SAXS data to a power law, the exponent α, which is related to the polymer fractal structure can be extracted [201,203]. Values of α=1, 2 and 4 correlate to rigid rod, lamellar structure, and spheres, respectively, although interactions between molecules cause deviations from these ideal slopes. SAXS data for pure PFT shows α=1.5 at low *q* (rod-like at large size), increasing to α=3.7 at high *q* (sphere-like at small size). Deviation from α=1 arises from the branched network seen by cryoEM (Fig. 6.1.D) [221]. SAXS power-law slopes for $C_{60}(PI)_n$ high-adducts correspond to a percolation network at low *q* and rod-like behavior at high *q*, indicating aggregation [201,222]. SAXS data from the combined PFT:high adducts solution is well approximated as the mass-scaled sum of the pure PFT and pure fullerene scattering, suggesting a non-assembled mixture, similar to that seen by cryoEM. By contrast, mass-scaled

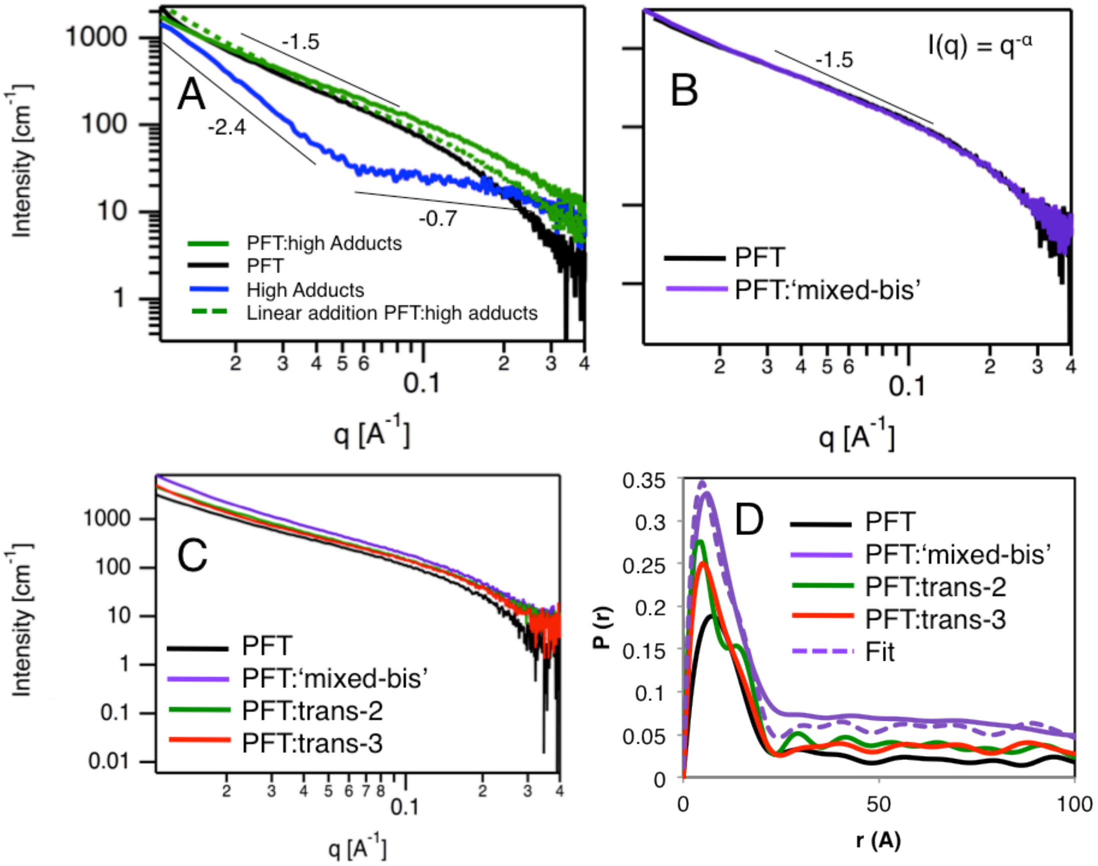

Figure 6.2. SAXS data for PFT and PFT/fullerene mixtures. A) Data for PFT:high-adducts is reasonably approximated by a sum of PFT+high-adducts. B) The PFT:'mixed-bis' profile overlap mass-scaled PFT data. C) Raw data for all PFT and PFT:bis-fullerene samples are similar. D) Fourier transformed P(r) data for the samples in (C) shows different fullerene environments for *trans*-2 and *trans*-3, with PFT:mix-bis corresponding to the sum of the two.

SAXS from solution of PFT and 'mixed-bis' adducts is nearly identical to the pure PFT. This provides strong evidence that the $C_{60}(PI)_2$ and PFT coassemble into a single micellar aggregate.

Finally, electronic interactions in the assemblies are confirmed using luminescence quenching, which provides an indirect measure of the photo-induced charge transfer from the polymer to the fullerenes [223]. In Fig. 6.3.A, we see that solutions of PFT:high adducts show relatively little PL quenching, presumably because donors and acceptors are not in close physical proximity. By contrast solutions of PFT with the 'mixed-bis' adducts have significant PL quenching, indicating both physical and electronic contact.

With a donor/acceptor system that co-assembles in aqueous solution, we next consider the efficiency of charge separation in those assemblies using ultrafast broad-band transient absorption spectroscopy on aqueous solutions of co-assembled PFT:'mixed-bis' adducts. Representative transient absorption spectra at different probe delays following excitation at 470 nm are shown in Fig. 6.3.B. We assign the negative transient absorption peak near 520 nm to stimulated emission, as the spectral features and the lifetime (Fig. 6.3.C) match the fluorescence emission. Interestingly, the 690-nm absorption of the PFT hole polaron (P^+) appears on a sub-ps timescale following photoexcitation [224,225]. This ultrafast appearance of P^+ reconfirms that the $C_{60}(PI)_2$ adducts must be co-assembled with PFT, since there is no other way that charge transfer could occur so quickly: there is simply no time for diffusion or any other structural rearrangement to occur. Once formed, Fig. 6.3.C shows that about 75% of the PFT polarons decay back to the ground state in ~200 ps. The remaining polarons survive past the ns time scale.

To mimic biological charge-separation systems, co-assembly and rapid charge separation are required, but if they are followed by rapid recombination, the charges cannot be used. We

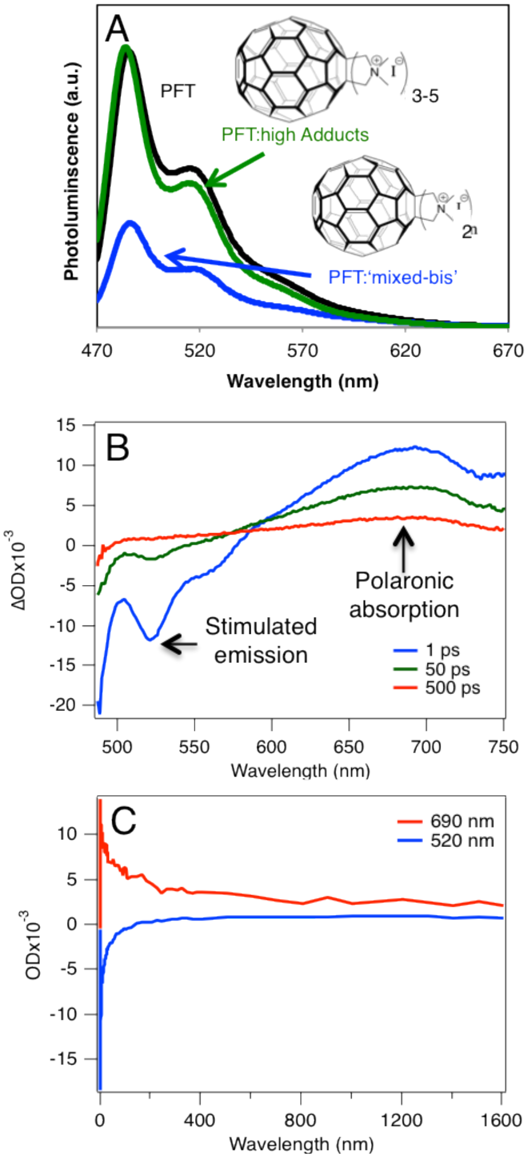

Figure 6.3. Formation of P^+ and N^- polarons requires intimate assembly of the polymer and fullerene. (A) PL of PFT, PFT:high adducts, and PFT:'mixed bis'; (B) pump-probe spectroscopy for PFT:'mixed bis' solutions excited at 470 nm showing the rapid formation of both excitons and polarons; (C) time decays for the stimulated emission and the polaronic absorption from (B).

thus wanted to further optimize our fullerene acceptors for charge separation. We did this by creating molecules that could assemble intimately with the PFT for efficient charge transfer and molecules that would assemble more loosely, allowing us to pull the electron away from the PFT and prevent recombination. Both types of molecules are available simply by separating $C_{60}(PI)_2$ isomers. Our 'mixed-bis' samples are primarily composed of four isomers (10% *trans*-1, 39% *trans*-2, 44% *trans*-3 and 7% *trans*-4). Structures of the dominant isomers are shown in Fig. 6.4.A-B. We were able to partially separate these isomers, producing fractions that we refer to as predominantly *trans*-2 (85% *trans*-2 and 15% *trans*-1) and predominantly *trans*-3 (72% *trans*-3 and 28% *trans*-2). The *trans*-1 and 2 fullerenes have charges on opposite sides of the ball and can be viewed as an isotropically-charged molecule that should not easily insert into a PFT micelle. By contrast, the angle between charges in *trans*-3 is 145^o, suggesting a more amphiphilic molecule that could insert into the PFT micelle.

The co-assembly of PFT with *trans*-2 and *trans*-3 was examined via SAXS. Raw scattering data for all of the samples looks similar to pure PFT (Fig. 6.2.C), but Fourier analysis with the assumption of monodispersed rods does show subtle variations. In Fig. 6.2.D, PFT and PFT:*trans*-3 show similar probability distributions, supporting the picture of insertion of fullerene into the PFT micelle. Interestingly, PFT:*trans*-2 shows two peaks, reminiscent of a polymer micelle with a partial "shell" of fullerenes surrounding the outside. The PFT:'mixed-bis' data can be well fit by a simple linear combination of the PFT:*trans*-2 and PFT:*trans*-3 probability distributions, further supporting idea that *trans*-3 assembles on the inside of the polymer micelle while *trans*-2 surrounds the outside.

Fig. 6.4.D shows luminescence quenching measurements that further support the idea that different isomers of $C_{60}(PI)_2$ assemble in different places in the PFT micelle. The data indicates

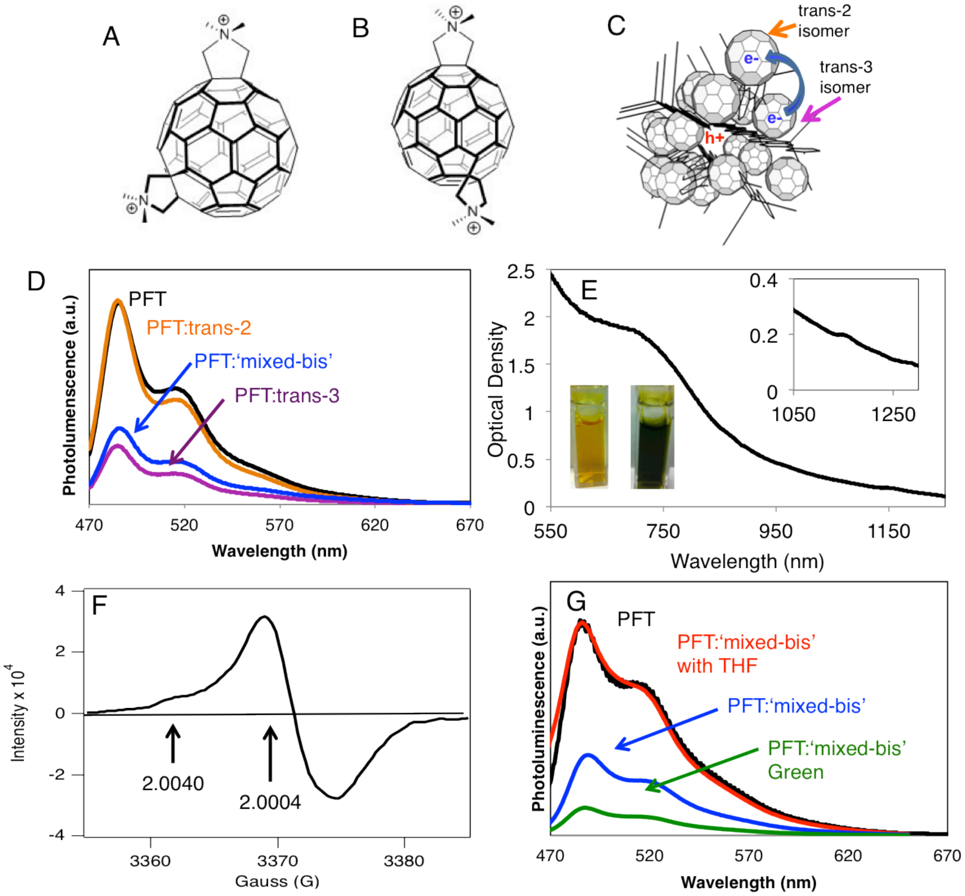

Fig. 6.4. Spectroscopic evidence for long-lived charged species in solution. Chemical structure of *trans*-3 bis (A) and *trans*-2 bis (B). Cartoon depicting the assembly of trans-2 and trans-3 bis with PFT leading to long-lived polarons in solution (C). PL of PFT, PFT:'mixed-bis', PFT:*trans*-3 bis, and PFT:*trans*-2 bis (D). Absorption from a green PFT/fullerene solution showing both P^+ and N^- polarons (E). EPR from a similar green solution, again showing both P^+ and N^- polarons (F). PL for various PFT:'mixed bis' showing that polarons quench luminescence, but the addition of THF, which, destroying the PFT/fullerene assembly, restores PL intensity (G).

that assemblies of PFT with the *trans*-2 fullerenes produces little luminescence quenching, while PFT assembled with an equal amount of *trans*-3 fullerenes show strong quenching. These quenching results suggests that not only can we selectively associate fullerenes with polymer micelles using the number of charges, we also can control the position of the fullerene within the micelle by the placement of the charges, as depicted in Fig. 6.4.C.

Given this degree of control, the next step is to form assemblies of PFT and 'mixed-bis' adducts containing both intimately assembled *trans*-3 and more isotropically-charged *trans*-2 fullerenes. This co-assembly should permit rapid photo-induced electron transfer from PFT to the *trans*-3 fullerenes, followed by a second electron transfer step to the *trans*-2 fullerenes. If this type of directed ET cascade occurs, electrons on the *trans*-2 fullerenes should be stabilized in the high dielectric environment of the water surrounding the micelle, preventing recombination with the PFT. Indeed, we find that photoexcitation of aqueous PFT:'mixed-bis' adduct solutions causes a dramatic color change from yellow to dark green (inset of Fig. 6.4.D); once exposed to light, and the color change is essentially permanent, lasting days to weeks.

PFT is a blue-absorbing polymer with an absorption maximum at 430 nm in water and little to no absorbance past 550 nm[179]. When oxidized with iodine, the hole polaron (P^+) of PFT absorbs in the sub-gap region at 690 nm[226]. The color change in Fig. 6.4E is thus due to the formation of positive polarons on the PFT, as evidenced by their 690-nm absorption. The inset shows that simultaneously, a significantly weaker negative (N^-) polaron absorption peak due to the $C_{60}(PI)_2$ molecular anion is observed at 1180 nm. The low intensity of the N^- absorption has several origins: 1) the absorption cross-section of fullerene anions is much smaller than that of the polymer polarons[227]; 2) the weak N^- absorption peak sits on top of a broad scattering background from the co-assembled micelles in solution; and 3) the N^- polaron might react with impurities in the water, despite our best efforts to deoxygenate the solutions by freeze-pump-thaw techniques[228].

To further confirm the formation of stable, separated N^- and P^+ polarons after exposure to light, we turned to electron paramagnetic resonance (EPR) experiments. Figure 6.4.F shows the EPR signal from the green PFT:'mixed-bis' adducts solution; the *g*-factors for the N^- and P^+ polarons are 2.0004 and 2.0040, respectively, in good agreement with literature values for many other polymer/fullerene systems[229]. The N^- polaron line width we observe is broader than that in other polymer/fullerene systems because of both the interaction of the water dipoles with the polarons, and the different spin-relaxation times for the electron and hole[230,231]. The most significant difference between our co-assembled system and previous systems, however, is that the previous EPR work required active photoexcitation (light-induced EPR) in order to observe the polaron signals. In contrast, once exposed to light, the polarons created in our PFT:$C_{60}(PI)_2$ solutions remain stable indefinitely.

Further confirmation that the long-lived separated charges result from a self-assembled ET cascade comes by examining the details of luminescence for a range of samples. Aqueous solutions of predominantly *trans*-2 bis fullerenes with PFT do briefly turn green during the course of the dissolution, indicating polaron formation (possibly from disordered polymer:fullerene assemblies). On the other hand, despite the efficient luminescence quenching in solutions of PFT co-assembled with the predominantly *trans*-3 bis fullerenes, the solutions do not turn green and there is no other evidence for the formation of long-lived separated charges. Indeed, our ultrafast experiments show that polarons are formed on sub-ps time scales (as in Fig. 6.3.B, but recombine with 100% yield over the next few hundred ps). These results indicate that controlling the spatial position of the fullerenes can dramatically affect carrier dynamics.

Finally, upon photoexcitation of PFT:'mixed-bis' fullerene solutions, we observe increased luminescence quenching due to exciton quenching by P^+-polarons (Fig. 6.4.G). However, if tetrahydrofuran (THF), which is known to disassemble polymer micelles [232], is added to the co-assembled green system, the luminescence signal regains intensity (Fig. 6.4.G). This further supports the idea that intimate assembly is required to facilitate a charge transfer cascade and avoid recombination, resulting in stable polarons.

6.3. Conclusions

The self-assembly of the PFT polymer with a combination of *trans*-2 and *trans*-3 charged bis-fullerene isomers forms an ET cascade that promotes the creation of long-lived charge species. Upon photoexcitation of PFT, an electron is transferred to *trans*-3 fullerenes sitting within the micelle; the electron is then funneled to the adjacent *trans*-2 fullerene sitting the gallery region of the micelle, where it is stabilized by reorganization of the surrounding water. The electron and hole are now spatially separated, decreasing the probability of recombination to near zero, so that the separated charges are stable in aqueous solution for weeks. The key to producing these stabilized, separated charges lies in controlling the nanoscale structure of our polymer/fullerene assemblies. Now that the general principles of designing artificial self-assembled ET cascades are known, it should be possible to apply these principles to the production of water-based OPV devices.

6.4. Experimental

6.4.1. Materials Synthesis

PFT synthesis previously reported [179].

Bis-N-methylpyrrolidine adducts were synthesized according to published methods [233,234] and were separated according to the following procedure: The crude product was dry loaded onto a silica column pre-treated with 2% triethylamine in toluene with an unusually large ratio of silica gel to product 1:~500 and the column was run with an extremely slow elution rate (~1-2 mL/min). The column was first eluted with toluene to yield a purple fraction of C_{60} followed by a second brown fraction containing the monoadduct (r_f = 0.70 2/10/88 TEA/Et_2O/PhMe). After elution of the monoadduct, the eluent was changed to 2/10/88 TEA/Et_2O/PhMe and two closely spaced fractions. The first fraction gives two spots by TLC corresponding to the *Trans-1* and *Trans-2* isomers (r_f = 0.50 and r_f = 0.43 2/10/88 TEA/Et_2O/PhMe) and the second fraction gives a two spots by TLC corresponding to the *Trans-2* and *Trans-3* isomers (r_f = 0.43 2/10/88 TEA/Et_2O/PhMe r_f = 0.33 2/10/88 TEA/Et_2O/PhMe) Subsequent fractions contain many spots with r_f ranging from 0.2 to 0.33 (2/10/88 TEA/Et_2O/PhMe) corresponding to a complex mixture of *Trans-3*, *4*, *e*, and *cis-3* isomers which can be separated by HPLC using published methods.[234] ^{1}H NMR, ^{13}C NMR, and MALDI-TOF spectra for the *Trans-1* and *Trans-2* and *Trans-2* and *Trans-3* mixtures match with previously reported spectra for the pure compounds.[234]

6.4.2. Methods

For cryoEM, grids were prepared by placing a small drop (~4 μl) of sample solution onto glow discharged holy carbon mesh Quantifoil 200 mesh grids with 3.5 μm holes spaced 1 μm apart. The grids were then blotted and plunged immediately into liquid nitrogen cooled liquid ethane to rapidly freeze the samples in vitrified ice. The cryo grids were visualized with an FEI Tecnai F20 transmission electron microscope at an accelerating voltage of 200 kV. Images were collected on a 16 megapixel CCD camera at ~50,000x magnification with a defocus value of approximately 3 μm.

Small-angle X-ray scattering (SAXS) experiments were conducted at the Stanford Synchrotron Radiation Laboratory (SSRL) Beamline 4-2. Using a syringe, 100 μL of each sample was loaded in a quartz capillary and held at 25^{o}C. Scattered X-rays (at 12 keV) were collected with a Rayonix MX225-HE detector (sample to detector distance = 1.7 m). The two-dimensional data was radially averaged to obtain one-dimensional scattering curves.

Electron paramagnetic resonance was performed at UCLA in the Molecular Instrumentation Center (MIC). Experiments were performed on the Bruker EMX EPR spectrometer in a nitrogen finger dewar to keep the sample frozen at 95 K. The microwave frequency was 9.437 GHz, amplitude of 4 G, microwave power of 0.02 mW and a scan time of 20.972 s for 32 accumulated scans.

A femtosecond Ti:Sapphire amplifier (Coherent, Legend Elite) seeded with a broadband Ti:Sapphire oscillator (Coherent, Mantis) was used for ultrafast pump-probe transient absorption experiments. Spectral and kinetic data acquisition was accomplished using a commercially built spectrometer (HELIOS, Ultrafast Systems LLC). The amplifier output consisting of 40 fs, 3 mJ pulses centered around 800 nm (at 1 kHz repetition rate) was split into two beams of roughly equal power. One of the beams was directed to an Optical Parametric Amplifier (Light Conversion, TOPAS-C) to create 470 nm pump pulses. A small portion of the amplifier output was focused onto a sapphire crystal to generate white light continuum (WLC) probe laser pulses. The probe beam was directed onto a computer-controller translation stage so that the time-delay between the pump and the probe could be varied. The pump and probe pulses were focused into the sample in a non-collinear geometry, making it possible to select only the WLC probe pulses for detection. The probe beam was focused onto the sample such that the spot-size of probe beam was smaller than the pump beam in order to ensure that the data collected came from a uniformly excited region. Solution-phase samples of a concentration of 1mg/ml were filled in glass cuvettes with 1 mm path-length to ensure sufficient transmission of the probe light. The transmitted probe beam through the sample was collimated onto a fiber optic cable using a telescope and then dispersed onto a one dimensional CCD detector. We chopped the pump beam at a frequency of 500 Hz and recorded the pump on/pump off signals for each consecutive pair of pulses to calculate the normalized transient absorption spectrum for a particular probe delay. We used a modest pump pulse energy of 60 nJ (spot size ~ 5 mm) for excitation and ensured that we were safely in the linear regime.

UV-vis absorption spectra were taken on a Perkin-ElmerLambda25spectrometer in a 0.1 cm glass cell in DMSO. ^{1}H and ^{13}C NMR spectra were taken on a 500 MHz Bruker Avance AV 500 spectrometer equipped with a 5mm dual cryoprobe.

CHAPTER 7

CONCLUSIONS

This work provides insight into how important nm-scale morphology is to charge separation and device performance. By utilizing different device fabrication techniques we can aim to scale-up OPV devices to industrial roll-to-roll printing, allowing OPVs to become a commercially available product. Additionally, due to the harmful halogenated solvents that are typically used in processing these organic polymers and fullerenes, we have found a viable pathway towards a water-soluble polymer:fullerene system that includes both P^+ (holes) and N^- (electrons) that are stable in solution for days to weeks. We aim to transfer this assembly into a solid state OPV device.

OPV device fabrication requires a nm-scale intimately mixed system; however surprisingly BC and SqP techniques require different polymer crystallinities to obtain the most efficient device. In this work we provided a study that shows explicitly what is required in BC and SqP for P3HT, a traditionally edge-on oriented semicrystalline polymer. However, as presented in literature, different polymers require their own specific conditions to fabricate the most efficient device. Where this research can be applied broadly to other semicrystalline polymers, it does not necessarily translate to amorphous polymers. These amorphous polymers have some of the highest efficiencies in literature and need to be fully investigated in regards to these device fabrication techniques. Especially because the SqP method that would provide a more reproducible pathway towards industrial roll-to-roll devices.

Although the most efficient organic solar devices contain an electron donating polymer and electron accepting fullerene, it is important to investigate other electron acceptors, such as the n-type polymers that were studied here. PBFI-T is a promising n-type polymer for all-polymer solar devices; it out-performed its very similar selenophene copolymer, PBFI-S. We determined that the main difference between these two polymers was the amount of mixing present when performing GIWAXS experiments. PBFI-S mixed more with PSEHTT then PBFI-T, which suggests that pure polymer domains result in better device performance.

TRMC is a unique method to determine the local mobility in a pure fullerene films. By examining these shuttlecock derivatives first with theory and then building up to TRMC, we determined that the local mobilities of these fullerenes are similar to that of PCBM. However, when SCLC devices are fabricated the mobilities are significantly lower then that of PCBM. This study elucidates that local assembly is important, but macroscopic assembly of these fullerenes is just as necessary as the local assembly to achieve respectable macroscopic mobilities.

Device morphology is essential to charge separation but the structure of the individual organic components is also vital to device performance. By studying a self-assembling semiconducting polymer, PFT, we have the ability to straighten polymer chains along the long-direction of the micelle and thus improve conductivity along the polymer backbone. Additionally, through rheology we determined that the PFT network consists of “sticky ends” that bridge other polymer micelles creating an interconnected network. This network was also observable through cryoEM. Due to the bridging nature of PFT, the photogenerated charges in this network can travel along the polymer chains more efficiently then a random walk unassembled polymer.

To achieve our goal of creating a water-processable solar cell we synthesized a water soluble fullerene, $C_{60}(N^{+})_{n}$, that assembles with the PFT micelle in solution. The assembly of these two molecular components in water results in long-lived charge carriers that are stable on the length scale of days to weeks. However, this assembly does require the bis adduct fullerenes instead of the higher adduct fullerenes. Bis fullerene adducts are not water-soluble so assembly with PFT is required to solvate the fullerene, where the high adducts are substituted with n=3-5 adducts on the fullerene ball that allows them to assemble separate from the PFT in solution. To further study this system, the bis adducts were separated into fractions of *trans*-2 and *trans*-3 isomers. This intimate assembly of the bis fullerene facilitates the polaron formation by the *trans*-3 fullerene assembling within the PFT micelle and the *trans*-2 fullerene assembling with the PFT side chains. Upon excitation of the system the electron is quickly transferred (< 1 ps) from PFT to the *trans*-3 isomer and then the electron is shuttled out to the *trans*-2 isomer where it is stabilized by the dielectric of the water. The electron and hole are now out of the recombination range and are stable in their respective environments. Here we have essentially turned off recombination, which is one of the largest hurdles in the OPV community. The next step is to determine how to transfer this polaronic formation into the solid state to create a water-processable device, which requires retention of the self-assembled nature of these organic components.

The content of this thesis elucidates the importance of the nm-scale morphology of OPV devices. The facilitation of these device morphologies can be address in various ways. First, we can study and control the active layer morphology of polymer:fullerene composites through two different device fabrication techniques. Additionally, we can control the active layer morphology by designing organic molecules that self-assemble. This level of control allows us to determine the polymer chain morphology, while also controlling the structure of the overall active layer. And finally by controlling the assembly of the electron-acceptor through self-assembly too, we can create long-lived charge carriers that are stable in solution for days to weeks. These stable charges are unprecedented in polymer:fullerene solutions and if these polarons can be transferred to the solid state it could be a viable pathway towards a water-processable solar device. All of these results point towards how the knowledge of the nanoscale morphology of OPV devices is imperative to designing devices with efficient charge separation and charge transfer.

REFERENCES

(1) Krebs, F. C.; Espinosa, N.; Hösel, M.; Søndergaard, R. R.; Jørgensen, M. 25th Anniversary Article: Rise to Power - OPV-Based Solar Parks. *Adv. Mater.* **2014**, *26*, 29–39.

(2) Scharber, M. C.; Mühlbacher, D.; Koppe, M.; Denk, P.; Waldauf, C.; Heeger, a. J.; Brabec, C. J. Design Rules for Donors in Bulk-Heterojunction Solar Cells—Towards 10 % Energy-Conversion Efficiency. *Adv. Mater.* **2006**, *18*, 789–794.

(3) He, Z.; Zhong, C.; Su, S.; Xu, M.; Wu, H.; Cao, Y. Enhanced Power-Conversion Efficiency in Polymer Solar Cells Using an Inverted Device Structure. *Nat. Photonics* **2012**, *6*, 591–595.

(4) Shaw, P. E.; Ruseckas, A.; Samuel, I. D. W. Exciton Diffusion Measurements in Poly(3-Hexylthiophene). *Adv. Mater.* **2008**, *20*, 3516–3520.

(5) Clark, A. P.; Shi, C.; Ng, B. C.; Wilking, J. N.; Ayzner, A. L.; Stieg, A. Z.; Schwartz, B. J.; Mason, T. G.; Rubin, Y.; Tolbert, S. H.; et al. Self-Assembling Semiconducting Polymers-Rods and Gels from Electronic Materials. *ACS Nano* **2013**, *7*, 962–977.

(6) Deibel, C.; Dyakonov, V. Polymer–Fullerene Bulk Heterojunction Solar Cells. *Rep. Prog. Phys* **2010**, *73*, 096401.

(7) Helgesen, M.; Søndergaard, R.; Krebs, F. C. Advanced Materials and Processes for Polymer Solar Cell Devices. *J. Mater. Chem.* **2010**, *20*, 36.

(8) He, Z.; Zhong, C.; Su, S.; Xu, M.; Wu, H.; Cao, Y. Enhanced Power-Conversion Efficiency in Polymer Solar Cells Using an Inverted Device Structure. *Nat. Photonics* **2012**, *6*, 591–595.

(9) Li, G.; Zhu, R.; Yang, Y. Polymer Solar Cells. *Nat. Photonics* **2012**, *6*, 153–161.

(10) You, J.; Chen, C.-C.; Hong, Z.; Yoshimura, K.; Ohya, K.; Xu, R.; Ye, S.; Gao, J.; Li, G.; Yang, Y. 10.2% Power Conversion Efficiency Polymer Tandem Solar Cells Consisting of Two Identical Sub-Cells. *Adv. Mater.* **2013**, *25*, 3973–3978.

(11) You, J.; Dou, L.; Yoshimura, K.; Kato, T.; Ohya, K.; Moriarty, T.; Emery, K.; Chen, C.-C.; Gao, J.; Li, G.; et al. A Polymer Tandem Solar Cell with 10.6% Power Conversion Efficiency. *Nat. Commun.* **2013**, *4*, 1446.

(12) Yu, G.; Gao, J.; Hummelen, J. C.; Wudl, F.; Heeger, A. J. Polymer Photovoltaic Cells: Enhanced Efficiencies via a Network of Internal Donor-Acceptor Heterojunctions. *Science (80-.).* **1995**, *270*, 1789–1791.

(13) Kim, Y.; Choulis, S. A.; Nelson, J.; Bradley, D. D. C.; Cook, S.; Durrant, J. R. Device Annealing Effect in Organic Solar Cells with Blends of Regioregular poly(3-Hexylthiophene) and Soluble Fullerene. *Appl. Phys. Lett.* **2005**, *86*, 63502.

(14) Ayzner, A. L.; Wanger, D. D.; Tassone, C. J.; Tolbert, S. H.; Schwartz, B. J. Room to Improve Conjugated Polymer-Based Solar Cells: Understanding How Thermal Annealing Affects the Fullerene Component of a Bulk Heterojunction Photovoltaic Device. *J. Phys. Chem. C* **2008**, *112*, 18711–18716.

(15) Collins, B. A.; Gann, E.; Guignard, L.; He, X.; McNeill, C. R.; Ade, H. Molecular Miscibility of Polymer−Fullerene Blends. *J. Phys. Chem. Lett.* **2010**, *1*, 3160–3166.

(16) Chen, D.; Nakahara, A.; Wei, D.; Nordlund, D.; Russell, T. P. P3HT/PCBM Bulk Heterojunction Organic Photovoltaics: Correlating Efficiency and Morphology. *Nano Lett.* **2011**, *11*, 561–567.

(17) Parnell, A. J.; Cadby, A. J.; Mykhaylyk, O. O.; Dunbar, A. D. F.; Hopkinson, P. E.; Donald, A. M.; Jones, R. A. L. Nanoscale Phase Separation of P3HT PCBM Thick Films As Measured by Small-Angle X-Ray Scattering. *Macromolecules* **2011**, *44*, 6503–6508.

(18) Bartelt, J. A.; Beiley, Z. M.; Hoke, E. T.; Mateker, W. R.; Douglas, J. D.; Collins, B. A.; Tumbleston, J. R.; Graham, K. R.; Amassian, A.; Ade, H.; et al. The Importance of Fullerene Percolation in the Mixed Regions of Polymer-Fullerene Bulk Heterojunction Solar Cells. *Adv. Energy Mater.* **2013**, *3*, 364–374.

(19) Shoaee, S.; Subramaniyan, S.; Xin, H.; Keiderling, C.; Tuladhar, P. S.; Jamieson, F.; Jenekhe, S. A.; Durrant, J. R. Charge Photogeneration for a Series of Thiazolo-Thiazole Donor Polymers Blended with the Fullerene Electron Acceptors PCBM and ICBA. *Adv. Funct. Mater.* **2013**, *23*, 3286–3298.

(20) Li, G.; Shrotriya, V.; Huang, J.; Yao, Y.; Moriarty, T.; Emery, K.; Yang, Y. High-Efficiency Solution Processable Polymer Photovoltaic Cells by Self-Organization of Polymer Blends. *Nat. Mater.* **2005**, *4*, 864–868.

(21) Verploegen, E.; Mondal, R.; Bettinger, C. J.; Sok, S.; Toney, M. F.; Bao, Z. Effects of Thermal Annealing Upon the Morphology of Polymer-Fullerene Blends. *Adv. Funct. Mater.* **2010**, *20*, 3519–3529.

(22) Westacott, P.; Tumbleston, J. R.; Shoaee, S.; Fearn, S.; Bannock, J. H.; Gilchrist, J. B.; Heutz, S.; DeMello, J.; Heeney, M.; Ade, H.; et al. On the Role of Intermixed Phases in Organic Photovoltaic Blends. *Energy Environ. Sci.* **2013**, *6*, 2756–2764.

(23) Gomez, E. D.; Barteau, K. P.; Wang, H.; Toney, M. F.; Loo, Y.-L. Correlating the Scattered Intensities of P3HT and PCBM to the Current Densities of Polymer Solar Cells. *Chem. Commun. (Camb).* **2011**, *47*, 436–438.

(24) Guo, J.; Ohkita, H.; Benten, H.; Ito, S. Charge Generation and Recombination Dynamics in Poly (3-Hexylthiophene)/fullerene Blend Films with Different Regioregularities and Morphologies. *J. Am. Chem. Soc.* **2010**, *132*, 6154–6164.

(25) Cates, N. C.; Gysel, R.; Beiley, Z.; Miller, C. E.; Toney, M. F.; Heeney, M.; McCulloch, I.; McGehee, M. D. Tuning the Properties of Polymer Bulk Heterojunction Solar Cells by Adjusting Fullerene Size to Control Intercalation. *Nano Lett.* **2009**, *9*, 4153–4157.

(26) Watts, B.; Belcher, W. J.; Thomsen, L.; Ade, H.; Dastoor, P. C. A Quantitative Study of PCBM Diffusion during Annealing of P3HT:PCBM Blend Films. *Macromolecules* **2009**, *42*, 8392–8397.

(27) Peet, J.; Soci, C.; Coffin, R. C.; Nguyen, T. Q.; Mikhailovsky, A.; Moses, D.; Bazan, G. C. Method for Increasing the Photoconductive Response in Conjugated Polymer/fullerene Composites. *Appl. Phys. Lett.* **2006**, *89*, 252103–252105.

(28) Peet, J.; Kim, J.; Coates, N.; Ma, W. L.; Moses, D.; Heeger, A. J.; Bazan, G. C. Efficiency Enhancement in Low-Bandgap Polymer Solar Cells by Processing with Alkane Dithiols. *Nat. Mater.* **2007**, *6*, 497–500.

(29) Lee, J. K.; Ma, W. L.; Brabec, C. J.; Yuen, J.; Moon, J. S.; Kim, J. Y.; Lee, K.; Bazan, G. C.; Heeger, A. J. Processing Additives for Improved Efficiency from Bulk Heterojunction Solar Cells. *J. Am. Chem. Soc.* **2008**, *130*, 3619–3623.

(30) Chang, L.; Jacobs, I. E.; Augustine, M. P.; Moulé, A. J. Correlating Dilute Solvent Interactions to Morphology and OPV Device Performance. *Org. Electron.* **2013**, *14*, 2431–2443.

(31) Chen, W.; Xu, T.; He, F.; Wang, W.; Wang, C.; Strzalka, J.; Liu, Y.; Wen, J.; Miller, D. J.; Chen, J.; et al. Hierarchical Nanomorphologies Promote Exciton Dissociation in Polymer/fullerene Bulk Heterojunction Solar Cells. *Nano Lett.* **2011**, *11*, 3707–3713.

(32) Ayzner, A. L.; Tassone, C. J.; Tolbert, S. H.; Schwartz, B. J. Reappraising the Need for Bulk Heterojunctions in Polymer− Fullerene Photovoltaics: The Role of Carrier Transport in All-Solution-Processed P3HT/PCBM Bilayer Solar. *J. Phys. Chem. C* **2009**, *113*, 20050–20060.

(33) Chen, D.; Liu, F.; Wang, C.; Nakahara, A.; Russell, T. P. Bulk Heterojunction Photovoltaic Active Layers via Bilayer. *Nano Lett.* **2011**, *11*, 2071–2078.

(34) Gevaerts, V. S.; Koster, L. J. A.; Wienk, M. M.; Janssen, R. A. J. Discriminating between Bilayer and Bulk Heterojunction Polymer:Fullerene Solar Cells Using the External Quantum Efficiency. *ACS Appl. Mater. Interfaces* **2011**, *3*, 3252–3255.

(35) Moon, J. S.; Takacs, C. J.; Sun, Y.; Heeger, A. J. Spontaneous Formation of Bulk Heterojunction Nanostructures: Multiple Routes to Equivalent Morphologies. *Nano Lett.* **2011**, *11*, 1036–1039.

(36) Cho, S.-M.; Bae, J.-H.; Jang, E.; Kim, M.-H.; Lee, C.; Lee, S.-D. Solvent Effect of the Fibrillar Morphology on the Power Conversion Efficiency of a Polymer Photovoltaic Cell in a Diffusive Heterojunction. *Semicond. Sci. Technol.* **2012**, *27*, 125018.

(37) Gadisa, A.; Tumbleston, J. R.; Ko, D.-H.; Aryal, M.; Lopez, R.; Samulski, E. T. The Role of Solvent and Morphology on Miscibility of Methanofullerene and poly(3-Hexylthiophene). *Thin Solid Films* **2012**, *520*, 5466–5471.

(38) Thummalakunta, L. N. S. A.; Yong, C. H.; Ananthanarayanan, K.; Luther, J. P3HT Based Solution-Processed Pseudo Bi-Layer Organic Solar Cell with Enhanced Performance. *Org. Electron.* **2012**, *13*, 2008–2016.

(39) Wong, M. K.; Wong, K. Y. Investigation of the Factors Affecting the Power Conversion Efficiency of All-Solution-Processed "bilayer" P3HT:PCBM Solar Cells. *Synth. Met.* **2013**, *170*, 1–6.

(40) Li, H.; Qi, Z.; Wang, J. Layer-by-Layer Processed Polymer Solar Cells with Self-Assembled Electron Buffer Layer. *Appl. Phys. Lett.* **2013**, *102*, 213901.

(41) Yang, B.; Yuan, Y.; Huang, J. Reduced Bimolecular Charge Recombination Loss in Thermally-Annealed Bilayer Heterojunction Photovoltaic Devices with Large External Quantum Efficiency and Fill Factor. *J. Phys. Chem. C* **2014**, *118*, 5196–5202.

(42) Lin, Y.; Ma, L.; Li, Y.; Liu, Y.; Zhu, D.; Zhan, X. Small-Molecule Solar Cells with Fill Factors up to 0.75 via a Layer-by-Layer Solution Process. *Adv. Energy Mater.* **2014**, *4*, 1300626.

(43) Nardes, A. M.; Ayzner, A. L.; Hammond, S. R.; Ferguson, A. J.; Schwartz, B. J.; Kopidakis, N. Photoinduced Charge Carrier Generation and Decay in Sequentially Deposited Polymer/Fullerene Layers: Bulk Heterojunction vs Planar Interface. *J. Phys. Chem. C* **2012**, *116*, 7293–7305.

(44) Lee, K. H.; Schwenn, P. E.; Smith, A. R. G.; Cavaye, H.; Shaw, P. E.; James, M.; Krueger, K. B.; Gentle, I. R.; Meredith, P.; Burn, P. L. Morphology of All-Solution-Processed "Bilayer" Organic Solar Cells. *Adv. Mater.* **2011**, *23*, 766–770.

(45) Treat, N. D.; Brady, M. a.; Smith, G.; Toney, M. F.; Kramer, E. J.; Hawker, C. J.; Chabinyc, M. L. Interdiffusion of PCBM and P3HT Reveals Miscibility in a Photovoltaically Active Blend. *Adv. Energy Mater.* **2011**, *1*, 82–89.

(46) Lee, K. H.; Zhang, Y.; Burn, P. L.; Gentle, I. R.; James, M.; Nelson, A.; Meredith, P. Correlation of Diffusion and Performance in Sequentially Processed P3HT/PCBM

Heterojunction Films by Time-Resolved Neutron Reflectometry. *J. Mater. Chem. C* **2013**, *1*, 2593.

(47) Hawks, S. A.; Aguirre, J. C.; Schelhas, L. T.; Thompson, R. J.; Huber, R. C.; Ferreira, A. S.; Zhang, G.; Herzing, A. A.; Tolbert, S. H.; Schwartz, B. J. Comparing Matched Polymer:Fullerene Solar Cells Made by Solution-Sequential Processing and Traditional Blend Casting: Nanoscale Structure and Device Performance. *J. Phys. Chem. C* **2014**, DOI:10.1021/jp504560r.

(48) Dang, M.; Hirsch, L.; Wantz, G. P3HT: PCBM, Best Seller in Polymer Photovoltaic Research. *Adv. Mater.* **2011**, *23*, 3597–3602.

(49) Yang, C.; Heeger, A. Morphology of Composites of Semiconducting Polymers Mixed with C 60. *Synth. Met.* **1996**, *83*, 85–88.

(50) Wang, D. H.; Moon, J. S.; Seifter, J.; Jo, J.; Park, J. H.; Park, O. O.; Heeger, A. J. Sequential Processing: Control of Nanomorphology in Bulk Heterojunction Solar Cells. *Nano Lett.* **2011**, *11*, 3163–3168.

(51) Li, H.; Li, Y.; Wang, J. Optimizing Performance of Layer-by-Layer Processed Polymer Solar Cells. *Appl. Phys. Lett.* **2012**, *101*, 033907.

(52) Li, H.; Wang, J. Layer-by-Layer Processed High-Performance Polymer Solar Cells. *Appl. Phys. Lett.* **2012**, *101*, 263901–263905.

(53) Cheng, P.; Hou, J.; Li, Y.; Zhan, X. Layer-by-Layer Solution-Processed Low-Bandgap Polymer-PC 61 BM Solar Cells with High Efficiency. *Adv. Energy Mater.* **2014**, DOI: 10.1002/aenm.201301349.

(54) Loiudice, A.; Rizzo, A.; Latini, G.; Nobile, C.; de Giorgi, M.; Gigli, G. Graded Vertical Phase Separation of Donor/acceptor Species for Polymer Solar Cells. *Sol. Energy Mater. Sol. Cells* **2012**, *100*, 147–152.

(55) Loiudice, A.; Rizzo, A.; Biasiucci, M.; Gigli, G. Bulk Heterojunction versus Diffused Bilayer: The Role of Device Geometry in Solution P-Doped Polymer-Based Solar Cells. *J. Phys. Chem. Lett.* **2012**, *3*, 1908–1915.

(56) Tao, C.; Aljada, M.; Shaw, P. E.; Lee, K. H.; Cavaye, H.; Balfour, M. N.; Borthwick, R. J.; James, M.; Burn, P. L.; Gentle, I. R.; et al. Controlling Hierarchy in Solution-Processed Polymer Solar Cells Based on Crosslinked P3HT. *Adv. Energy Mater.* **2013**, *3*, 105–112.

(57) Yang, H. Y.; Kang, N. S.; Hong, J.-M.; Song, Y.-W.; Kim, T. W.; Lim, J. A. Efficient Bilayer Heterojunction Polymer Solar Cells with Bumpy Donor–acceptor Interface Formed by Facile Polymer Blend. *Org. Electron.* **2012**, *13*, 2688–2695.

(58) Chen, H.; Hu, S.; Zang, H.; Hu, B.; Dadmun, M. Precise Structural Development and Its Correlation to Function in Conjugated Polymer: Fullerene Thin Films by Controlled Solvent Annealing. *Adv. Funct. Mater.* **2013**, *23*, 1701–1710.

(59) Kim, D. H.; Mei, J.; Ayzner, A. L.; Schmidt, K.; Giri, G.; Appleton, A. L.; Toney, M. F.; Bao, Z. Sequentially Solution-Processed, Nanostructured Polymer Photovoltaics Using Selective Solvents. *Energy Environ. Sci.* **2014**, *7*, 1103–1109.

(60) Ayzner, A. L.; Doan, S. C.; de Villers, B.; Schwartz, B. J. Ultrafast Studies of Exciton Migration and Polaron Formation in Sequentially Solution-Processed Conjugated Polymer/Fullerene Quasi-Bilayer Photovoltaics. *J. Phys. Chem. Lett.* **2012**, *3*, 2281–2287.

(61) Rochester, C. W.; Mauger, S. A.; Moule, A. J. Investigating the Morphology of Polymer/Fullerene Layers Coated Using Orthogonal Solvents. *J. Phys. Chem. C* **2012**, *116*, 7287–7292.

(62) Jiang, X.; Osterbacka, R.; Korovyanko, O.; An, C. P.; Horovitz, B.; Janssen, R. A. J.; Vardeny, Z. V. Spectroscopic Studies of Photoexcitations in Regioregular and Regiorandom Polythiophene Films. *Adv. Funct. Mater.* **2002**, *12*, 587–597.

(63) Kim, Y.; Cook, S.; Tuladhar, S. M.; Choulis, S. a.; Nelson, J.; Durrant, J. R.; Bradley, D. D. C.; Giles, M.; McCulloch, I.; Ha, C.-S.; et al. A Strong Regioregularity Effect in Self-Organizing Conjugated Polymer Films and High-Efficiency Polythiophene:fullerene Solar Cells. *Nat. Mater.* **2006**, *5*, 197–203.

(64) Mauer, R.; Kastler, M.; Laquai, F. The Impact of Polymer Regioregularity on Charge Transport and Efficiency of P3HT:PCBM Photovoltaic Devices. *Adv. Funct. Mater.* **2010**, *20*, 2085–2092.

(65) Adachi, T.; Brazard, J.; Ono, R. J.; Hanson, B.; Traub, M. C.; Wu, Z.; Li, Z.; Bolinger, J. C.; Ganesan, V.; Bielawski, C. W.; et al. Regioregularity and Single Polythiophene Chain Conformation. *J. Phys. Chem. Lett.* **2011**, *2*, 1400–1404.

(66) Collins, B. A.; Tumbleston, J. R.; Ade, H. Miscibility, Crystallinity, and Phase Development in P3HT/PCBM Solar Cells: Toward an Enlightened Understanding of Device Morphology and Stability. *J. Phys. Chem. Lett.* **2011**, *2*, 3135–3145.

(67) Brown, P. J.; Thomas, D. S.; Köhler, A.; Wilson, J. S.; Kim, J.-S.; Ramsdale, C. M.; Sirringhaus, H.; Friend, R. H. Effect of Interchain Interactions on the Absorption and Emission of poly(3-Hexylthiophene). *Phys. Rev. B* **2003**, *67*, 064203–064218.

(68) Kohn, P.; Rong, Z.; Scherer, K. H.; Sepe, A.; Sommer, M.; Müller-Buschbaum, P.; Friend, R. H.; Steiner, U.; Hüttner, S. Crystallization-Induced 10-Nm Structure Formation in P3HT/PCBM Blends. *Macromolecules* **2013**, *46*, 4002–4013.

(69) Bronstein, H. A.; Luscombe, C. K. Externally Initiated Regioregular P3HT with Controlled Molecular Weight and Narrow Polydispersity. **2009**, 12894–12895.

(70) Brabec, C. J.; Heeney, M.; McCulloch, I.; Nelson, J. Influence of Blend Microstructure on Bulk Heterojunction Organic Photovoltaic Performance. *Chem. Soc. Rev.* **2011**, *40*, 1185–1199.

(71) Kline, R. J.; McGehee, M. D.; Kadnikova, E. N.; Liu, J.; Fréchet, J. M. J.; Toney, M. F. Dependence of Regioregular Poly (3-Hexylthiophene) Film Morphology and Field-Effect Mobility on Molecular Weight. *Macromolecules* **2005**, *38*, 3312–3319.

(72) Zhang, R.; Li, B.; Iovu, M. C.; Jeffries-el, M.; Cooper, J.; Jia, S.; Tristram-nagle, S.; Smilgies, D. M.; Lambeth, D. N.; Mccullough, R. D.; et al. Nanostructure Dependence of Field-Effect Mobility in Regioregular poly(3-Hexylthiophene) Thin Film Field Effect Transistors. *J. Am. Chem. Soc.* **2006**, *128*, 3480–3481.

(73) Noriega, R.; Rivnay, J.; Vandewal, K.; Koch, F. P. V; Stingelin, N.; Smith, P.; Toney, M. F.; Salleo, A. A General Relationship between Disorder, Aggregation and Charge Transport in Conjugated Polymers. *Nat. Mater.* **2013**, 1–7.

(74) Pingel, P.; Zen, A.; Abellón, R. D.; Grozema, F. C.; Siebbeles, L. D. A.; Neher, D. Temperature-Resolved Local and Macroscopic Charge Carrier Transport in Thin P3HT Layers. *Adv. Funct. Mater.* **2010**, *20*, 2286–2295.

(75) Brinkmann, M.; Rannou, P. Molecular Weight Dependence of Chain Packing and Semicrystalline Structure in Oriented Films of Regioregular Poly(3-Hexylthiophene) Revealed by High-Resolution Transmission Electron Microscopy. *Macromolecules* **2009**, *42*, 1125–1130.

(76) Kline, R. J.; McGehee, M. D.; Kadnikova, E. N.; Liu, J.; Fréchet, J. M. J. Controlling the Field-Effect Mobility of Regioregular Polythiophene by Changing the Molecular Weight. *Adv. Mater.* **2003**, *15*, 1519–1522.

(77) Müller, C.; Ferenczi, T. a. M.; Campoy-Quiles, M.; Frost, J. M.; Bradley, D. D. C.; Smith, P.; Stingelin-Stutzmann, N.; Nelson, J. Binary Organic Photovoltaic Blends: A Simple Rationale for Optimum Compositions. *Adv. Mater.* **2008**, *20*, 3510–3515.

(78) Kirchartz, T.; Deledalle, F.; Tuladhar, P. S.; Durrant, J. R.; Nelson, J. On the Differences between Dark and Light Ideality Factor in Polymer: Fullerene Solar Cells. *J. Phys. Chem. Lett.* **2013**, *4*, 2371–2376.

(79) Street, R. A.; Krakaris, A.; Cowan, S. R. Recombination Through Different Types of Localized States in Organic Solar Cells. *Adv. Funct. Mater.* **2012**, *22*, 4608–4619.

(80) Street, R. A.; Schoendorf, M.; Roy, A.; Lee, J. H. Interface State Recombination in Organic Solar Cells. *Phys. Rev. B* **2010**, *81*, 205307.

(81) Kirchartz, T.; Pieters, B. E.; Kirkpatrick, J.; Rau, U.; Nelson, J. Recombination via Tail States in Polythiophene:fullerene Solar Cells. *Phys. Rev. B* **2011**, *83*, 115209.

(82) Foertig, A.; Rauh, J.; Dyakonov, V.; Deibel, C. Shockley Equation Parameters of P3HT:PCBM Solar Cells Determined by Transient Techniques. *Phys. Rev. B* **2012**, *86*, 115302.

(83) Woo, C. H.; Thompson, B. C.; Kim, B. J.; Toney, M. F.; Fréchet, J. M. J. The Influence of poly(3-Hexylthiophene) Regioregularity on Fullerene-Composite Solar Cell Performance. *J. Am. Chem. Soc.* **2008**, *130*, 16324–16329.

(84) Veldman, D.; Meskers, S. C. J.; Janssen, R. A. J. The Energy of Charge-Transfer States in Electron Donor-Acceptor Blends: Insight into the Energy Losses in Organic Solar Cells. *Adv. Funct. Mater.* **2009**, *19*, 1939–1948.

(85) Tress, W.; Leo, K.; Riede, M. Optimum Mobility, Contact Properties, and Open-Circuit Voltage of Organic Solar Cells: A Drift-Diffusion Simulation Study. *Phys. Rev. B* **2012**, *85*, 155201.

(86) Clark, J.; Silva, C.; Friend, R. H.; Spano, F. C. Role of Intermolecular Coupling in the Photophysics of Disordered Organic Semiconductors: Aggregate Emission in Regioregular Polythiophene. *Phys. Rev. Lett.* **2007**, *98*, 206406.

(87) Spano, F. C. Modeling Disorder in Polymer Aggregates: The Optical Spectroscopy of Regioregular poly(3-Hexylthiophene) Thin Films. *J. Chem. Phys.* **2005**, *122*, 234701.

(88) Gierschner, J.; Mack, H.-G.; Lüer, L.; Oelkrug, D. Fluorescence and Absorption Spectra of Oligophenylenevinylenes: Vibronic Coupling, Band Shapes, and Solvatochromism. *J. Chem. Phys.* **2002**, *116*, 8596.

(89) Niles, E. T.; Roehling, J. D.; Yamagata, H.; Wise, A. J.; Spano, F. C.; Moule, A. J.; Grey, J. K. J-Aggregate Behavior in Poly-3-Hexylthiophene Nanofibers. *J. Phys. Chem. Lett.* **2012**, *3*, 259–263.

(90) Gao, Y.; Grey, J. K. Resonance Chemical Imaging of Polythiophene/fullerene Photovoltaic Thin Films: Mapping Morphology-Dependent Aggregated and Unaggregated C=C Species. *J. Am. Chem. Soc.* **2009**, *131*, 9654–9662.

(91) O'Connor, B. T.; Reid, O. G.; Zhang, X.; Kline, R. J.; Richter, L. J.; Gundlach, D. J.; DeLongchamp, D. M.; Toney, M. F.; Kopidakis, N.; Rumbles, G. Morphological Origin of Charge Transport Anisotropy in Aligned Polythiophene Thin Films. *Adv. Funct. Mater.* **2014**, DOI: 10.1002/adfm.201303351.

(92) Reid, O.; Pensack, R.; Song, Y. Charge Photogeneration in Neat Conjugated Polymers. *Chem. Mater.* **2013**, DOI: 10.1021/cm4027144.

(93) Lee, K. H.; Schwenn, P. E.; Smith, A. R. G.; Cavaye, H.; Shaw, P. E.; James, M.; Krueger, K. B.; Gentle, I. R.; Meredith, P.; Burn, P. L. Morphology of All-Solution-Processed “Bilayer” Organic Solar Cells. *Adv. Mater.* **2011**, *23*, 766–770.

(94) Abbas, M.; Tekin, N. Balanced Charge Carrier Mobilities in Bulk Heterojunction Organic Solar Cells. *Appl. Phys. Lett.* **2012**, *101*, 073302.

(95) Kumar, A.; Liao, H.-H.; Yang, Y. Hole Mobility in Optimized Organic Photovoltaic Blend Films Obtained Using Extraction Current Transients. *Org. Electron.* **2009**, *10*, 1615–1620.

(96) Yin, W.; Dadmun, M. A New Model for the Morphology of P3HT/PCBM Organic Photovoltaics from Small-Angle Neutron Scattering: Rivers and Streams. *Nano Lett.* **2011**, *5*, 4756–4768.

(97) Chen, H.; Hegde, R.; Browning, J.; Dadmun, M. D. The Miscibility and Depth Profile of PCBM in P3HT: Thermodynamic Information to Improve Organic Photovoltaics. *Phys. Chem. Chem. Phys.* **2012**, *14*, 5635–5641.

(98) Kozub, D. R.; Vakhshouri, K.; Orme, L. M.; Wang, C.; Hexemer, A.; Gomez, E. D. Polymer Crystallization of Partially Miscible Polythiophene/Fullerene Mixtures Controls Morphology. *Macromolecules* **2011**, *44*, 5722–5726.

(99) Chen, W.; Nikiforov, M. P.; Darling, S. B. Morphology Characterization in Organic and Hybrid Solar Cells. *Energy Environ. Sci.* **2012**, *5*, 8045–8074.

(100) Gu, S.; Neugebauer, H.; Sariciftci, N. S. Conjugated Polymer-Based Organic Solar Cells. *Chem. Rev.* **2007**, *107*, 1324–1338.

(101) Cheng, Y.-J.; Yang, S.-H.; Hsu, C.-S. Synthesis of Conjugated Polymers for Organic Solar Cell Applications. *Chem. Rev.* **2009**, *109*, 5868–5923.

(102) Günes, S.; Neugebauer, H.; Sariciftci, N. Conjugated Polymer-Based Organic Solar Cells. *Chem. Rev.* **2007**, *45*, 723–733.

(103) Guo, X.; Zhou, N.; Lou, S. J.; Smith, J.; Tice, D. B.; Hennek, J. W.; Ortiz, R. P.; Navarrete, J. T. L.; Li, S.; Strzalka, J.; et al. Polymer Solar Cells with Enhanced Fill Factors. *Nat. Photonics* **2013**, *7*, 825–833.

(104) Small, C. E.; Chen, S.; Subbiah, J.; Amb, C. M.; Tsang, S.-W.; Lai, T.-H.; Reynolds, J. R.; So, F. High-Efficiency Inverted Dithienogermole–thienopyrrolodione-Based Polymer Solar Cells. *Nat. Photonics* **2011**, *6*, 115–120.

(105) Earmme, T.; Hwang, Y.; Murari, N. M.; Subramaniyan, S.; Jenekhe, S. A. All-Polymer Solar Cells with 3.3% E Ffi Ciency Based on Naphthalene Diimide-Selenophene Copolymer Acceptor. *J. Am. Chem. Soc.* **2013**, *135*, 14960–14963.

(106) Cheng, P.; Ye, L.; Zhao, X.; Hou, J.; Li, Y.; Zhan, X. Binary Additives Synergistically Boost the Efficiency of All-Polymer Solar Cells up to 3.45%. *Energy Environ. Sci.* **2014**, *7*, 1351.

(107) Zhou, E.; Cong, J.; Hashimoto, K.; Tajima, K. Control of Miscibility and Aggregation via the Material Design and Coating Process for High-Performance Polymer Blend Solar Cells. *Adv. Mater.* **2013**, *25*, 6991–6996.

(108) Kietzke, T.; Hörhold, H.; Neher, D. Efficient Polymer Solar Cells Based on M3EH-PPV. *Chem. Mater.* **2005**, 6532–6537.

(109) Friedel, B.; McNeill, C. R.; Greenham, N. C. Influence of Alkyl Side-Chain Length on the Performance of Poly(3-alkylthiophene)/Polyfluorene All-Polymer Solar Cells. *Chem. Mater.* **2010**, *22*, 3389–3398.

(110) Holcombe, T. W.; Woo, C. H.; Kavulak, D. F. J.; Thompson, B. C.; Fre, J. M. J. All-Polymer Photovoltaic Devices of Poly (3-(4-N-Octyl)-Phenylthiophene) from Grignard Metathesis (GRIM) Polymerization. *J. Am. Chem. Soc. Commun.* **2009**, *131*, 14160–14161.

(111) Hwang, Y.-J.; Ren, G.; Murari, N. M.; Jenekhe, S. a. N-Type Naphthalene Diimide–Biselenophene Copolymer for All-Polymer Bulk Heterojunction Solar Cells. *Macromolecules* **2012**, *45*, 9056–9062.

(112) Yao, K.; Intemann, J. J.; Yip, H.-L.; Liang, P.-W.; Chang, C.-Y.; Zang, Y.; Li, Z.; Chen, Y.; Jen, A. K.-Y. Efficient All Polymer Solar Cells from Layer-Evolved Processing of a Bilayer Inverted Structure. *J. Mater. Chem. C* **2014**, *2*, 416.

(113) Zhan, X.; Tan, Z.; Domercq, B.; An, Z. A High-Mobility Electron-Transport Polymer with Broad Absorption and Its Use in Field-Effect Transistors and All-Polymer Solar Cells. *J. ...* **2007**, *129*, 7246–7247.

(114) Zhou, Y.; Kurosawa, T.; Ma, W.; Guo, Y.; Fang, L.; Vandewal, K.; Diao, Y.; Wang, C.; Yan, Q.; Reinspach, J.; et al. High Performance All-Polymer Solar Cell via Polymer Side-Chain Engineering. *Adv. Mater.* **2014**, *26*, 3767–3772.

(115) Hwang, Y.-J.; Earmme, T.; Subramaniyan, S.; Jenekhe, S. a. Side Chain Engineering of N-Type Conjugated Polymer Enhances Photocurrent and Efficiency of All-Polymer Solar Cells. *Chem. Commun. (Camb).* **2014**, *50*, 10801–10804.

(116) Earmme, T.; Hwang, Y.-J.; Subramaniyan, S.; Jenekhe, S. a. All-Polymer Bulk Heterojuction Solar Cells with 4.8% Efficiency Achieved by Solution Processing from a Co-Solvent. *Adv. Mater.* **2014**, *26*, 6080–6085.

(117) Di Nuzzo, D.; Wetzelaer, G.-J. a. H.; Bouwer, R. K. M.; Gevaerts, V. S.; Meskers, S. C. J.; Hummelen, J. C.; Blom, P. W. M.; Janssen, R. a. J. Simultaneous Open-Circuit Voltage

Enhancement and Short-Circuit Current Loss in Polymer: Fullerene Solar Cells Correlated by Reduced Quantum Efficiency for Photoinduced Electron Transfer. *Adv. Energy Mater.* **2013**, *3*, 85–94.

(118) Clarke, T. M.; Durrant, J. R. Charge Photogeneration in Organic Solar Cells. *Chem. Rev.* **2010**, *110*, 6736–6767.

(119) Ren, G.; Schlenker, C. W.; Ahmed, E.; Subramaniyan, S.; Olthof, S.; Kahn, A.; Ginger, D. S.; Jenekhe, S. a. Photoinduced Hole Transfer Becomes Suppressed with Diminished Driving Force in Polymer-Fullerene Solar Cells While Electron Transfer Remains Active. *Adv. Funct. Mater.* **2013**, *23*, 1238–1249.

(120) Alam, M.; Jenekhe, S. Efficient Solar Cells from Layered Nanostructures of Donor and Acceptor Conjugated Polymers. *Chem. Mater.* **2004**, *16*, 4647–4656.

(121) Halls, J. J. M.; Walsh, C. A.; Greenham, N.; Marseglia, E. A.; Friend, R.; Moratti, S. C.; Holmes, A. Efficient Photodiodes from Interpenetrating Polymer Networks. *Nature* **1995**, *376*, 498–500.

(122) Mori, D.; Benten, H.; Kosaka, J.; Ohkita, H.; Ito, S.; Miyake, K. Polymer/polymer Blend Solar Cells with 2.0% Efficiency Developed by Thermal Purification of Nanoscale-Phase-Separated Morphology. *ACS Appl. Mater. Interfaces* **2011**, *3*, 2924–2927.

(123) He, X.; Gao, F.; Tu, G.; Hasko, D.; Hüttner, S.; Steiner, U.; Greenham, N. C.; Friend, R. H.; Huck, W. T. S. Formation of Nanopatterned Polymer Blends in Photovoltaic Devices. *Nano Lett.* **2010**, *10*, 1302–1307.

(124) Li, H.; Kim, F. S.; Ren, G.; Hollenbeck, E. C.; Subramaniyan, S.; Jenekhe, S. a. Tetraazabenzodifluoranthene Diimides: Building Blocks for Solution-Processable N-Type Organic Semiconductors. *Angew. Chem. Int. Ed. Engl.* **2013**, *52*, 5513–5517.

(125) Li, H.; Kim, F. S.; Ren, G.; Jenekhe, S. A. High-Mobility N - Type Conjugated Polymers Based on Electron- De Fi Cient Tetraazabenzodi Fl Uoranthene Diimide for Organic Electronics. *J. Am. Chem. Soc.* **2013**, *135*, 14920–14923.

(126) Xin, H.; Subramaniyan, S.; Kwon, T. Enhanced Open Circuit Voltage and Efficiency of Donor − Acceptor Copolymer Solar Cells by Using Indene-C60 Bisadduct. *Chem. Mater.* **2012**, *24*, 1995–2001.

(127) Hollinger, J.; Jahnke, A. A.; Coombs, N.; Seferos, D. S. Controlling Phase Separation and Optical Properties in Conjugated Polymers through Selenophene - Thiophene Copolymerization. *J. Am. Chem. Soc.* **2010**, *132*, 8546–8547.

(128) Chen, H.; Peet, J.; Hu, S.; Azoulay, J.; Bazan, G.; Dadmun, M. The Role of Fullerene Mixing Behavior in the Performance of Organic Photovoltaics: PCBM in Low-Bandgap Polymers. *Adv. Funct. Mater.* **2014**, *24*, 140–150.

(129) Chen, D.; Nakahara, A.; Wei, D.; Nordlund, D.; Russell, T. P. P3HT/PCBM Bulk Heterojunction Organic Photovoltaics: Correlating Efficiency and Morphology. *Nano Lett.* **2011**, *11*, 561–567.

(130) Tang, Y.; McNeill, C. R. All-Polymer Solar Cells Utilizing Low Band Gap Polymers as Donor and Acceptor. *J. Polym. Sci. Part B Polym. Phys.* **2013**, *51*, 403–409.

(131) Han, H.; Lee, H.; Nam, S.; Jeong, J.; Lee, I. Poly (3-Hexylthiophene-Co-benzothiadiazole)(THBT) as an Electron-Accepting Polymer for Normal and Inverted Type All-Polymer Solar Cells. *Polym. Chem.* **2013**, *4*, 2053–2061.

(132) Bakulin, A. a; Rao, A.; Pavelyev, V. G.; van Loosdrecht, P. H. M.; Pshenichnikov, M. S.; Niedzialek, D.; Cornil, J.; Beljonne, D.; Friend, R. H. The Role of Driving Energy and Delocalized States for Charge Separation in Organic Semiconductors. *Science* **2012**, *335*, 1340–1344.

(133) Li, K.; Khlyabich, P.; Li, L. Influence of Exciton Diffusion and Charge-Transfer State Dissociation Efficiency on the Short-Circuit Current Densities in Semi-Random Donor/Acceptor Polymer:Fullerene Solar Cells. *J. Phys. Chem. C* **2013**, *117*, 6940–6948.

(134) Keivanidis, P. E.; Clarke, T. M.; Lilliu, S.; Agostinelli, T.; Macdonald, J. E.; Durrant, J. R.; Bradley, D. D. C.; Nelson, J. Dependence of Charge Separation Efficiency on Film Microstructure in Poly(3-Hexylthiophene-2,5-diyl):[6,6]-Phenyl-C 61 Butyric Acid Methyl Ester Blend Films. *J. Phys. Chem. Lett.* **2010**, *1*, 734–738.

(135) Tremolet de Villers, B.; Tassone, C. J.; Tolbert, S. H.; Schwartz, B. J. Improving the Reproducibility of P3HT:PCBM Solar Cells by Controlling the PCBM/Cathode Interface. *J. Phys. Chem. C* **2009**, *113*, 18978–18982.

(136) Kotlarski, J. D.; Moet, D. J. D.; Blom, P. W. M. Role of Balanced Charge Carrier Transport in Low Band Gap polymer:Fullerene Bulk Heterojunction Solar Cells. *J. Polym. Sci. Part B Polym. Phys.* **2011**, *49*, 708–711.

(137) Forrest, S. The Limits to Organic Photovoltaic Cell Efficiency. *MRS Bull.* **2005**, *30*, 28–32.

(138) Rance, W. L.; Ferguson, A. J.; Mccarthy-ward, T.; Heeney, M.; Ginley, D. S.; Olson, D. C.; Rumbles, G.; Kopidakis, N.; Al, R. E. T. Photoinduced Carrier Generation and Decay Dynamics in Intercalated and Non-Intercalated Polymer : Fullerene Bulk Heterojunctions. *ACS Nano* **2011**, *5*, 5635–5646.

(139) Yan, H.; Collins, B. A.; Gann, E.; Wang, C.; Ade, H.; Mcneill, C. R. Correlating the Efficiency and Nano-Morphology of Polymer Blend Solar Cells Utilizing Resonant Soft X-Ray Scattering. *ACS Nano6* **2012**, *6*, 677–688.

(140) Hoppe, H.; Sariciftci, N. S. Morphology of Polymer/fullerene Bulk Heterojunction Solar Cells. *J. Mater. Chem.* **2006**, *16*, 45.

(141) Bruner, C.; Miller, N. C.; McGehee, M. D.; Dauskardt, R. H. Molecular Intercalation and Cohesion of Organic Bulk Heterojunction Photovoltaic Devices. *Adv. Funct. Mater.* **2013**, *23*, 2863–2871.

(142) Etzold, F.; Howard, I. a; Mauer, R.; Meister, M.; Kim, T.-D.; Lee, K.-S.; Baek, N. S.; Laquai, F. Ultrafast Exciton Dissociation Followed by Nongeminate Charge Recombination in PCDTBT:PCBM Photovoltaic Blends. *J. Am. Chem. Soc.* **2011**, *133*, 9469–9479.

(143) Jeong, S.; Kwon, Y.; Choi, B.-D.; Ade, H.; Han, Y. S. Improved Efficiency of Bulk Heterojunction poly(3-hexylthiophene):[6,6]-Phenyl-C[sub 61]-Butyric Acid Methyl Ester Photovoltaic Devices Using Discotic Liquid Crystal Additives. *Appl. Phys. Lett.* **2010**, *96*, 183305.

(144) Troshin, P. a.; Hoppe, H.; Renz, J.; Egginger, M.; Mayorova, J. Y.; Goryachev, A. E.; Peregudov, A. S.; Lyubovskaya, R. N.; Gobsch, G.; Sariciftci, N. S.; et al. Material Solubility-Photovoltaic Performance Relationship in the Design of Novel Fullerene Derivatives for Bulk Heterojunction Solar Cells. *Adv. Funct. Mater.* **2009**, *19*, 779–788.

(145) Liang, Y.; Yu, L. A New Class of Semiconducting Polymers for Bulk Heterojunction Solar Cells with High Performance. *Acc. Chem. Res.* **2010**, *43*, 1227–1236.

(146) Ma, W.; Yang, C.; Gong, X.; Lee, K.; Heeger, A. â??J. Thermally Stable, Efficient Polymer Solar Cells with Nanoscale Control of the Interpenetrating Network Morphology. *Adv. Funct. Mater.* **2005**, *15*, 1617–1622.

(147) Kim, K.; Liu, J.; Namboothiry, M. A. G.; Carroll, D. L. Roles of Donor and Acceptor Nanodomains in 6% Efficient Thermally Annealed Polymer Photovoltaics. *Appl. Phys. Lett.* **2007**, *90*, 163511.

(148) Ayzner, A.; Tassone, C.; Tolbert, S.; Schwartz, B. Reappraising the Need for Bulk Heterojunctions in Polymer− Fullerene Photovoltaics: The Role of Carrier Transport in All-Solution-Processed P3HT/PCBM Bilayer Solar. *J. Phys. Chem. C* **2009**, *113*, 20050–20060.

(149) Wang, D. H.; Moon, J. S.; Seifter, J.; Jo, J.; Park, J. H.; Park, O. O.; Heeger, a J. Sequential Processing: Control of Nanomorphology in Bulk Heterojunction Solar Cells. *Nano Lett* **2011**, *11*, 3163–3168.

(150) Kennedy, R. D.; Ayzner, A. L.; Wanger, D. D.; Day, C. T.; Halim, M.; Khan, S. I.; Tolbert, S. H.; Schwartz, B. J.; Rubin, Y. Self-Assembling Fullerenes for Improved Bulk-Heterojunction Photovoltaic Devices. *J. Am. Chem. Soc.* **2008**, *130*, 17290–17292.

(151) Tassone, C. J.; Ayzner, A. L.; Kennedy, R. D.; Halim, M.; So, M.; Rubin, Y.; Tolbert, S. H.; Schwartz, B. J. Using Pentaarylfullerenes to Understand Network Formation in Conjugated Polymer-Based Bulk-Heterojunction Solar Cells. *J. Phys. Chem. C* **2011**, *115*, 22563–22571.

(152) Kennedy, R. D.; Halim, M.; Khan, S. I.; Schwartz, B. J.; Tolbert, S. H.; Rubin, Y. Crystal-Packing Trends for a Series of 6,9,12,15,18-Pentaaryl-1-hydro[60]fullerenes. *Chem. Eur. J.* **2012**, *18*, 7418–7433.

(153) Sawamura, M.; Kawai, K.; Matsuo, Y.; Kanie, K. Stacking of Conical Molecules with a Fullerene Apex into Polar Columns in Crystals and Liquid Crystals. *Nature* **2002**, *419*, 702–705.

(154) Huebener, K.; Scheloske, M.; Hauschild, J.; Harneit, W.; Zehl, G.; Fiechter, S. AFM Investigation of the Formation of One-Dimensional Structures of C60 Shuttlecocks on HOPG. *Phys. Status Solidi* **2006**, *243*, 2990–2994.

(155) Kirkpatrick, J. An Approximate Method for Calculating Transfer Integrals Based on the ZINDO Hamiltonian. *Int. J. Quantum Chem.* **2008**, *108*, 51–56.

(156) Marcus, R. A.; Amos, A. Electron Transfers in Chemistry and Biology. *Biochim. Biohysica Acta* **1985**, *811*, 265–322.

(157) Stein, T.; Kronik, L.; Baer, R. Reliable Prediction of Charge Transfer Excitations in Molecular Complexes Using Time-Dependent Density Functional Theory. *J. Am. Chem. Soc.* **2009**, *131*, 2818–2820.

(158) Wu, Q.; Van Voorhis, T. Extracting Electron Transfer Coupling Elements from Constrained Density Functional Theory. *J. Chem. Phys.* **2006**, *125*, 164105.

(159) Lemaur, V. Charge Transport Properties in Discotic Liquid Crystals: A Quantum-Chemical Insight into Structure-Property Relationships. *J. Am. Chem. Soc.* **2004**, *126*, 3271–3279.

(160) Bredas, J.-L.; Beljonne, D.; Coropceanu, V.; Cornil, J. Charge-Transfer and Energy-Transfer Processes in Π -Conjugated Oligomers and Polymers : A Molecular Picture. *Chem. Rev.* **2004**, *104*, 4971–5003.

(161) Raja, M.; Lloyd, G. C. R.; Sedghi, N.; Eccleston, W.; Di Lucrezia, R.; Higgins, S. J. Conduction Processes in Conjugated, Highly Regio-Regular, High Molecular Mass, poly(3-Hexylthiophene) Thin-Film Transistors. *J. Appl. Phys.* **2002**, *92*, 1441.

(162) Geens, W.; Martens, T.; Poortmans, J.; Aernouts, T.; Manca, J.; Lutsen, L.; Heremans, P.; Borghs, S.; Mertens, R.; Vanderzande, D. Modelling the Short-Circuit Current of Polymer Bulk Heterojunction Solar Cells. *Thin Solid Films* **2004**, *451-452*, 498–502.

(163) Shuttle, C. G.; Hamilton, R.; Nelson, J.; O'Regan, B. C.; Durrant, J. R. Measurement of Charge-Density Dependence of Carrier Mobility in an Organic Semiconductor Blend. *Adv. Funct. Mater.* **2010**, *20*, 698–702.

(164) Mozer, a. J.; Sariciftci, N. S.; Lutsen, L.; Vanderzande, D.; Österbacka, R.; Westerling, M.; Juška, G. Charge Transport and Recombination in Bulk Heterojunction Solar Cells Studied by the Photoinduced Charge Extraction in Linearly Increasing Voltage Technique. *Appl. Phys. Lett.* **2005**, *86*, 112104.

(165) Choulis, S. a.; Nelson, J.; Kim, Y.; Poplavskyy, D.; Kreouzis, T.; Durrant, J. R.; Bradley, D. D. C. Investigation of Transport Properties in Polymer/fullerene Blends Using Time-of-Flight Photocurrent Measurements. *Appl. Phys. Lett.* **2003**, *83*, 3812.

(166) Juska, G.; Arlauskas, K.; Viliunas, M. Extraction Current Transients: New Method of Study of Charge Transport in Microcrystalline Silicon. *Phys. Rev. Lett.* **2000**, *84*, 4946–4949.

(167) Dicker, G.; de Haas, M. P.; Warman, J. M.; de Leeuw, D. M.; Siebbeles, L. D. a. The Disperse Charge-Carrier Kinetics in Regioregular Poly(3-Hexylthiophene). *J. Phys. Chem. B* **2004**, *108*, 17818–17824.

(168) Ferguson, A. J.; Blackburn, J. L.; Holt, J. M.; Kopidakis, N.; Tenent, R. C.; Barnes, T. M.; Heben, M. J.; Rumbles, G. Photoinduced Energy and Charge Transfer in P3HT:SWNT Composites. *J. Phys. Chem. Lett.* **2010**, *1*, 2406–2411.

(169) Ferguson, A. J.; Kopidakis, N.; Shaheen, S. E.; Rumbles, G. Dark Carriers, Trapping, and Activation Control of Carrier Recombination in Neat P3HT and P3HT:PCBM Blends. *J. Phys. Chem. C* **2011**, *115*, 23134–23148.

(170) Mihailetchi, B. V. D.; Duren, J. K. J. Van; Blom, P. W. M.; Hummelen, J. C.; Janssen, R. A. J.; Kroon, J. M.; Rispens, M. T.; Verhees, W. J. H.; Wienk, M. M. Electron Transport in a Methanofullerene. *Adv. Funct. Mater.* **2003**, *13*, 43–46.

(171) He, Y.; Chen, H.; Hou, J.; Li, Y. Indene - C 60 Bisadduct : A New Acceptor for High-Performance Polymer Solar Cells. *J. Am. Chem. Soc.* **2010**, 1377–1382.

(172) Chi, C.; Mikhailovsky, A.; Bazan, G. C. Design of Cationic Conjugated Polyelectrolytes for DNA Concentration Determination. *J. Am. Chem. Soc.* **2007**, *129*, 11134–11145.

(173) Jiang, H.; Zhao, X.; Schanze, K. S. Effects of Polymer Aggregation and Quencher Size on Amplified Fluorescence Quenching of Conjugated Polyelectrolytes. *Langmuir* **2007**, *23*, 9481–9486.

(174) Jiang, H.; Taranekar, P.; Reynolds, J. R.; Schanze, K. S. Conjugated Polyelectrolytes: Synthesis, Photophysics, and Applications. *Angew. Chem. Int. Ed. Engl.* **2009**, *48*, 4300–4316.

(175) Thomas, A.; Houston, J. E.; Van den Brande, N.; De Winter, J.; Chevrier, M.; Heenan, R. K.; Terry, A. E.; Richeter, S.; Mehdi, A.; Van Mele, B.; et al. All-Conjugated Cationic Copolythiophene “rod–rod” Block Copolyelectrolytes: Synthesis, Optical Properties and Solvent-Dependent Assembly. *Polym. Chem.* **2014**, *5*, 3352.

(176) Wu, C.; Bull, B.; Szymanski, C.; Christensen, K.; McNeill, J. Multicolor Conjugated Polymer Dots for Biological Fluorescence Imaging. *ACS Nano* **2008**, *2*, 2415–2423.

(177) Tuncel, D.; Demir, H. V. Conjugated Polymer Nanoparticles. *Nanoscale* **2010**, *2*, 484–494.

(178) Stevens, A. L.; Kaeser, A.; Schenning, A. P. H. J.; Herz, L. M. Morphology-Dependent Energy Transfer Dynamics in Fluorene-Based Amphiphile Nanoparticles. *ACS Nano* **2012**, *6*, 4777–4787.

(179) Clark, A. P.-Z.; Shi, C.; Ng, B. C.; Wilking, J. N.; Ayzner, A. L.; Stieg, A. Z.; Schwartz, B. J.; Mason, T. G.; Rubin, Y.; Tolbert, S. H. Self-Assembling Semiconducting Polymers-Rods and Gels from Electronic Materials. *ACS Nano* **2013**, *7*, 962–977.

(180) Zaroslov, Y. D.; Gordeliy, V. I.; Kuklin, a. I.; Islamov, a. H.; Philippova, O. E.; Khokhlov, a. R.; Wegner, G. Self-Assembly of Polyelectrolyte Rods in Polymer Gel and in Solution: Small-Angle Neutron Scattering Study. *Macromolecules* **2002**, *35*, 4466–4471.

(181) Nguyen, T.; Martini, I.; Schwartz, B. Controlling Interchain Interactions in Conjugated Polymers: The Effects of Chain Morphology on Exciton-Exciton Annihilation and Aggregation in MEH-PPV Films. *J. Phys. Chem. B* **2000**, *104*, 237–255.

(182) Martini, I. B.; Smith, A. D.; Schwartz, B. J. Exciton-Exciton Annihilation and the Production of Interchain Species in Conjugated Polymer Films : Comparing the Ultrafast Stimulated Emission and Photoluminescence Dynamics of MEH-PPV. *Phys. Rev. B* **2004**, *69*, 1–12.

(183) Seo, J.; Gutacker, A.; Sun, Y. Improved High-Efficiency Organic Solar Cells via Incorporation of a Conjugated Polyelectrolyte Interlayer. *J. …* **2011**, *133*, 8416–8419.

(184) Costa, T.; Marques, A. T.; Se, J.; Melo, S. De; Thomas, A. W.; Garner, L. E.; Scherf, U.; Bazan, G. C.; Burrows, H. D. Self-Assembly of Poly{1,4-Phenylene-[9,9-bis(4-Phenoxy-Butylsulfonate)]fluorene-2,7-Diyl} with Oppositely Charged Phenylenevinylene Oligoelectrolytes. *J. Phys. Chem. B* **2014**, 613–623.

(185) Lutkenhaus, J. L.; Hammond, P. T. Electrochemically Enabled Polyelectrolyte Multilayer Devices: From Fuel Cells to Sensors. *Soft Matter* **2007**, *3*, 804.

(186) Wang, D.; Gong, X.; Heeger, P. S.; Rininsland, F.; Bazan, G. C.; Heeger, A. J. Biosensors from Conjugated Polyelectrolyte Complexes. *Proc. Natl. Acad. Sci. U. S. A.* **2002**, *99*, 49–53.

(187) Shu, S.; Zhang, X.; Wu, Z.; Wang, Z.; Li, C. Gradient Cross-Linked Biodegradable Polyelectrolyte Nanocapsules for Intracellular Protein Drug Delivery. *Biomaterials* **2010**, *31*, 6039–6049.

(188) O'Connell, M. J.; Chan, C. K.; Li, W.; Hicks, R. K.; Doorn, S. K.; Wang, H.-L. Polyelectrolyte Platform for Sensitive Detection of Biological Analytes via Reversible Fluorescence Quenching. *Polymer (Guildf).* **2007**, *48*, 7582–7589.

(189) Tai, B. C. U.; Wan, A. C. a; Ying, J. Y. Modified Polyelectrolyte Complex Fibrous Scaffold as a Matrix for 3D Cell Culture. *Biomaterials* **2010**, *31*, 5927–5935.

(190) Chakraborty, T.; Ghosh, S.; Moulik, S. P. Micellization and Related Behavior of Binary and Ternary Surfactant Mixtures in Aqueous Medium: Cetyl Pyridinium Chloride (CPC), Cetyl Trimethyl Ammonium Bromide (CTAB), and Polyoxyethylene (10) Cetyl Ether (Brij-56) Derived System. *J. Phys. Chem. B* **2005**, *109*, 14813–14823.

(191) Hennink, W. E.; van Nostrum, C. F. Novel Crosslinking Methods to Design Hydrogels. *Adv. Drug Deliv. Rev.* **2002**, *54*, 13–36.

(192) Luo, Y.; Kirker, K. R.; Prestwich, G. D. Cross-Linked Hyaluronic Acid Hydrogel Films: New Biomaterials for Drug Delivery. *J. Control. Release* **2000**, *69*, 169–184.

(193) Peppas, N. a.; Hilt, J. Z.; Khademhosseini, a.; Langer, R. Hydrogels in Biology and Medicine: From Molecular Principles to Bionanotechnology. *Adv. Mater.* **2006**, *18*, 1345–1360.

(194) Campoccia, D.; Doherty, P.; Radice, M.; Brun, P.; Abatangelo, G.; Williams, D. F. Semisynthetic Resorbable Materials from Hyaluronan Esterification. *Biomaterials* **1998**, *19*, 2101–2127.

(195) Prestwich, G. D.; Marecak, D. M.; Marecek, J. F.; Vercruysse, K. P.; Ziebell, M. R. Controlled Chemical Modification of Hyaluronic Acid: Synthesis, Applications, and Biodegradation of Hydrazide Derivatives. *J. Control. Release* **1998**, *53*, 93–103.

(196) Kroeze, J. E.; Savenije, T. J.; Vermeulen, M. J. W.; Warman, J. M. Contactless Determination of the Photoconductivity Action Spectrum, Exciton Diffusion Length, and Charge Separation Efficiency in Polythiophene-Sensitized TiO 2 Bilayers. **2003**, 7696–7705.

(197) Dicker, G.; de Haas, M. P.; Siebbeles, L. D. A.; Warman, J. M. Electrodeless Time-Resolved Microwave Conductivity Study of Charge-Carrier Photogeneration in Regioregular poly(3-Hexylthiophene) Thin Films. *Phys. Rev. B* **2004**, *70*, 45203.

(198) Piris, J.; Kopidakis, N.; Olson, D. C.; Shaheen, S. E.; Ginley, D. S.; Rumbles, G. The Locus of Free Charge-Carrier Generation in Solution-Cast Zn1−xMgxO/Poly(3-Hexylthiophene) Bilayers for Photovoltaic Applications. *Adv. Funct. Mater.* **2007**, *17*, 3849–3857.

(199) Ferguson, A. J.; Kopidakis, N.; Shaheen, S. E.; Rumbles, G. Quenching of Excitons by Holes in Poly(3-Hexylthiophene) Films. *J. Phys. Chem. C* **2008**, *112*, 9865–9871.

(200) Israelachvili, J. N.; Mitchell, D. J.; Ninham, B. W. *Theory of Self-Assembly of Hydrocarbon Amphiphiles into Micelles and Bilayers*; 1975; pp. 1525–1568.

(201) Beaucage, G. Small-Angle Scattering from Polymeric Mass Fractals of Arbitrary Mass-Fractal Dimension. *J. Appl. Crystallogr.* **1996**, *29*, 134–146.

(202) Svergun, D. I.; Koch, M. H. J. Small-Angle Scattering Studies of Biological Macromolecules in Solution. *Reports Prog. Phys.* **2003**, *66*, 1735–1782.

(203) Choudhary, S.; Bhatia, S. R. Rheology and Nanostructure of Hydrophobically Modified Alginate (HMA) Gels and Solutions. *Carbohydr. Polym.* **2012**, *87*, 524–530.

(204) Svergun, D. I. Restoring Low Resolution Structure of Biological Macromolecules from Solution Scattering Using Simulated Annealing. *Biophys. J.* **1999**, *76*, 2879–2886.

(205) Fairclough, J. P. A.; Norman, A. I. Structure and Rheology of Aqueous Gels. In *Annual Reports Section "C" (Physical Chemistry)*; 2003; Vol. 99, pp. 243–276.

(206) Shaw, M. T. *Introduction to Polymer Rheology*; 2012.

(207) Shah, J. V.; Janmey, P. a. Strain Hardening of Fibrin Gels and Plasma Clots. *Rheol. Acta* **1997**, *36*, 262–268.

(208) Hyun, K.; Wilhelm, M.; Klein, C. O.; Cho, K. S.; Nam, J. G.; Ahn, K. H.; Lee, S. J.; Ewoldt, R. H.; McKinley, G. H. A Review of Nonlinear Oscillatory Shear Tests: Analysis and Application of Large Amplitude Oscillatory Shear (LAOS). *Prog. Polym. Sci.* **2011**, *36*, 1697–1753.

(209) Tirtaatmadja, V.; Tam, K. C.; Jenkins, R. D. Superposition of Oscillations on Steady Shear Flow as a Technique for Investigating the Structure of Associative Polymers. *Macromolecules* **1997**, *30*, 1426–1433.

(210) Hyun, K.; Kim, S. H.; Ahn, K. H.; Lee, S. J. Large Amplitude Oscillatory Shear as a Way to Classify the Complex Fluids. *J. Nonnewton. Fluid Mech.* **2002**, *107*, 51–65.

(211) Evans, R. C. Harnessing Self-Assembly Strategies for the Rational Design of Conjugated Polymer Based Materials. *J. Mater. Chem. C* **2013**, *1*, 4190.

(212) Aguirre, J. C.; Arntsen, C.; Hernandez, S.; Huber, R.; Nardes, A. M.; Halim, M.; Kilbride, D.; Rubin, Y.; Tolbert, S. H.; Kopidakis, N.; et al. Understanding Local and Macroscopic Electron Mobilities in the Fullerene Network of Conjugated Polymer-Based Solar Cells: Time-Resolved Microwave Conductivity and Theory. *Adv. Funct. Mater.* **2014**, *24*, 784–792.

(213) Liang, Z.; Reese, M. O.; Gregg, B. A. Chemically Treating poly(3-Hexylthiophene) Defects to Improve Bulk Heterojunction Photovoltaics. *ACS Appl. Mater. Interfaces* **2011**, *3*, 2042–2050.

(214) Gregg, B. A. Transport in Charged Defect-Rich Π -Conjugated Polymers. *J. Phys. Chem. C* **2009**, *113*, 5899–5901.

(215) Rutherford, A. W. Photosystem II, the Water-Splitting Enzyme. *Trends Biochem. Sci.* **1989**, *14*, 227–232.

(216) Piris, J.; Dykstra, T. E.; Bakulin, A. A.; Loosdrecht, P. H. M. Van; Knulst, W.; Trinh, M. T.; Schins, J. M.; Siebbeles, L. D. A. Photogeneration and Ultrafast Dynamics of Excitons and Charges in P3HT/PCBM Blends. *J. Phys. Chem. C* **2009**, *113*, 14500–14506.

(217) Gélinas, S.; Paré-Labrosse, O.; Brosseau, C.-N.; Albert-Seifried, S.; McNeill, C. R.; Kirov, K. R.; Howard, I. A.; Leonelli, R.; Friend, R. H.; Silva, C. The Binding Energy of Charge-Transfer Excitons Localized at Polymeric Semiconductor Heterojunctions. *J. Phys. Chem. C* **2011**, 7114–7119.

(218) Lungenschmied, C.; Dennler, G.; Neugebauer, H.; Sariciftci, S. N.; Glatthaar, M.; Meyer, T.; Meyer, A. Flexible, Long-Lived, Large-Area, Organic Solar Cells. *Sol. Energy Mater. Sol. Cells* **2007**, *91*, 379–384.

(219) Yasuda, T.; Shinohara, Y.; Ishi-i, T.; Han, L. Use of Benzothiadiazole–triphenylamine Amorphous Polymer for Reproducible Performance of Polymer–fullerene Bulk-Heterojunction Solar Cells. *Org. Electron.* **2012**, *13*, 1802–1808.

(220) Cassell, A.; Asplund, C.; Tour, J. Self-Assembling Supramolecular Nanostructures from a C60 Derivative: Nanorods and Vesicles. *Angew. Chemie Int. Ed.* **1999**, *38*, 2403–2405.

(221) Li, Y.-C.; Chen, K.-B.; Chen, H.-L.; Hsu, C.-S.; Tsao, C.-S.; Chen, J.-H.; Chen, S.-A. Fractal Aggregates of Conjugated Polymer in Solution State. *Langmuir* **2006**, *22*, 11009–11015.

(222) Jeng, U.; Lin, T.-L.; Hu, Y.; Lin, J.-M.; Huang, Y.-S.; Liang, K. S.; Fan, L.; Thiyagarajan, P. Complex Structure of Fullerene Star Ionomers and Sodium Dodecyl Sulfate Resolved by Contrast Variation with SANS and SAXS. *Nucl. Instruments Methods Phys. Res. Sect. A Accel. Spectrometers, Detect. Assoc. Equip.* **2009**, *600*, 294–296.

(223) Park, Y.; Park, Y.; Gao, J.; Grey, J.; Wang, C. PPV and C 60 Nanocomposite with Enhanced Miscibility and Enhanced Photo-Induced Charge Transfer through Ground State Electrostatic Interactions. *Polymer (Guildf).* **2014**, *55*, 855–859.

(224) Österbacka, R.; An, C. P.; Jiang, X. M.; Vardeny, Z. V. Two-Dimensional Electronic Excitations in Self-Assembled Conjugated Polymer Nanocrystals. *Science (80-.).* **2000**, *287*, 839–842.

(225) Paquin, F.; Latini, G.; Sakowicz, M.; Karsenti, P.-L.; Wang, L.; Beljonne, D.; Stingelin, N.; Silva, C. Charge Separation in Semicrystalline Polymeric Semiconductors by Photoexcitation: Is the Mechanism Intrinsic or Extrinsic? *Phys. Rev. Lett.* **2011**, *106*, 197401.

(226) Chiang, C.; Fincher, C.; Park, Y.; Heeger, a.; Shirakawa, H.; Louis, E.; Gau, S.; MacDiarmid, A. Electrical Conductivity in Doped Polyacetylene. *Phys. Rev. Lett.* **1977**, *39*, 1098–1101.

(227) Kato, T.; Kodama, T.; Oyama, M.; Okazaki, S.; Shida, T. ESR and Optical Studies of the Radical Anion of C60. *Chem. Phys. Lett.* **1991**, *186*, 35–39.

(228) Guldi, D. M.; Prato, M. Excited-State Properties of C(60) Fullerene Derivatives. *Acc. Chem. Res.* **2000**, *33*, 695–703.

(229) Krinichnyi, V. I. Dynamics of Charge Carriers Photoinduced in poly(3-Dodecylthiophene)/fullerene Bulk Heterojunction. *Sol. Energy Mater. Sol. Cells* **2008**, *92*, 942–948.

(230) Savenije, T. J.; Sperlich, A.; Kraus, H.; Poluektov, O.; Heeney, M.; Dyakonov, V. Observation of Bi-Polarons in Blends of Conjugated Copolymers and Fullerene Derivatives. *Phys. Chem. Chem. Phys.* **2011**, *13*, 16579–16584.

(231) Ceuster, J.; Goovaerts, E.; Bouwen, a.; Hummelen, J.; Dyakonov, V. High-Frequency (95 GHz) Electron Paramagnetic Resonance Study of the Photoinduced Charge Transfer in Conjugated Polymer-Fullerene Composites. *Phys. Rev. B* **2001**, *64*, 195206.

(232) Kelley, E.; Smart, T.; Jackson, A. Structural Changes in Block Copolymer Micelles Induced by Cosolvent Mixtures. *Soft Matter* **2011**, *7*, 7094–7102.

(233) Maggini, M.; Scorrano, G.; Prato, M. Addition of Azomethine Ylides to C60: Synthesis, Characterization, and Functionalization of Fullerene Pyrrolidines. *J. Am. Chem. Soc.* **1993**, *115*, 9798–9799.

(234) Lu, Q.; Schuster, D. I.; Wilson, S. R. Preparation and Characterization of Six Bis(N-methylpyrrolidine)−C60 Isomers: Magnetic Deshielding in Isomeric Bisadducts of C60. *J. Org. Chem.* **1996**, *61*, 4764–4768.